Space Weather Propagation in the Inner Heliosphere

by

Alicia K. Petersen

A dissertation submitted in partial fulfillment
of the requirements for the degree of
Doctor of Philosophy
(Climate and Space Sciences and Engineering and Scientific Computing)
in The University of Michigan
2020

Doctoral Committee:

Professor Susan T. Lepri, Co-Chair
Professor Michael W. Liemohn, Co-Chair
Dr. Stephen W. Kahler, Air Force Research Laboratory
Associate Professor Justin C. Kasper
Associate Dean Timothy A. McKay
Assistant Professor Daniel T. Welling

"Creating a new theory is not like destroying an old barn and erecting a skyscraper in its place. It is rather like climbing a mountain, gaining new and wider views, discovering unexpected connections between our starting point and its rich environment. But the point from which we started out still exists and can be seen, although it appears smaller and forms a tiny part of our broad view gained by the mastery of the obstacles on our adventurous way up."

— Albert Einstein (*Einstein and Infeld*, 1961)

Alicia K. Petersen

aliciaks@umich.edu

ORCID iD: 0000-0003-3163-7832

For my little Leo. For my husband. For my family.

The light you bring into my life is as bright as the Sun.

ACKNOWLEDGEMENTS

Thank you to my sister, my parents, and my grandparents whose curiosity and support have both inspired me and grounded me my whole life, guiding me to where and who I am today.

Thank you to my amazing husband, Chris Petersen, whose enduring love, patience and faith in me has inspired me to persevere again and again. Forever and always, thank you.

Special thanks to Abby Azari without whose friendship, advice and camaraderie I would never have made it this far.

Thank you to my advisors, Mike Liemohn and Sue Lepri for all your incredible guidance, patience and mentorship.

Thank you to Stephen Kahler who has guided me with his vast knowledge and inspired me with his incredible insight into the state of the field.

Thank you to those in the Magnetosphere, Ionosphere, Thermosphere Research and Simulation group for your friendship, guidance and support. Special thanks to Dan Welling, Meghan Burleigh, Agnit Mukhopadhyay, Lois Keller-Smith, Alex Shane, and Brian Swiger.

Thank you to those in the Solar Heliospheric Research Group who have given me so much support and guidance through these years, especially Thomas Zurbuchen, Justin Kasper, Jim Raines, and Jason Gilbert.

Thank you to so many fellow students in the Climate and Space Sciences department for supporting me, encouraging me, and commiserating with me throughout

this crazy PhD process. Special shout-outs to Kali Roeten, Sam Basile, Jamie Ward, Sarah Spitzer, Ben Alterman, Camilla Harris, Ryan Dewey, and Doga Can Su Ozturk.

Thank you everyone at the Air Force Research Laboratory who have shared their expertise and friendship: Carl Henney, Stephen White, Rachel Hock-Mysliwiec, Nick Arge, Sam Schoenfeld, Sam Wallace, Michelle Simon, Sean Phillips and Scott Erwin.

Thank you Hazel Bain and Doug Biesecker at the Space Weather Prediction Center for your mentorship and for sharing your expertise in space weather forecasting.

Thank you to Laura Hopkins, Elaine Meinzer and Sandra Pytlinski for answering so many questions and smoothing out tricky situations.

Additional thanks to David MacKenzie of AFRL Space Vehicles and Shaela Jones-Mecholsky of NASA GSFC for their assistance with ADAPT-WSA. Special thanks to Ruth Skoug and John Steinberg of Los Alamos National Laboratory for their early assistance with interpreting ACE/SWEPAM data.

TABLE OF CONTENTS

LIST OF FIGURES

Figure

LIST OF TABLES

Table

LIST OF ABBREVIATIONS

AU Astronomical Unit

FIP first ionization potential

SEP solar energetic particle

CME coronal mass ejection

ICME interplanetary coronal mass ejection

NASA National Aeronautics and Space Administration

PSP Parker Solar Probe

LASCO Large Angle and Spectrometric Coronagraph

SOHO Solar and Heliospheric Observatory

EUV extreme ultraviolet light

SDO Solar Dynamics Observatory

ACE Advanced Composition Explorer

ESA European Space Agency

ADAPT-WSA Air Force Data Assimilative Photospheric flux Transport - Wang-Sheeley-Arge

ADAPT Air Force Data Assimilative Photospheric flux Transport

WSA Wang-Sheeley-Arge

IMF interplanetary magnetic field

HMF heliospheric magnetic field

CIR corotating interaction region

SIR stream interaction region

PAD pitch angle distribution

SE suprathermal electron

CSE counterstreaming suprathermal electron

SSE strahl suprathermal electron

NOAA National Oceanic and Atmospheric Administration

SWPC Space Weather Prediction Center

GONG Global Oscillation Network Group

EIT Extreme Ultraviolet Imaging Telescope

MAS MHD-on-A-Sphere

AIA Atmospheric Imaging Assembly

FIP first ionization potential

SWMF Space Weather Modeling Framework

ABSTRACT

The inner region of our solar system is vast, spanning hundreds of millions of kilometers and is driven by dynamics ranging in time scales from less than seconds to more than centuries. Space weather originating at the Sun and impacting life at Earth propagates through this complicated region, known as the inner heliosphere, whose dynamics is driven by the Sun's dynamic magnetic field. When space weather such as interplanetary coronal mass ejections (ICMEs) impact Earth, they can induce geomagnetic storms which cause the aurorae, cause damage to satellites, cause radio and GPS interference, and induce ground currents which can damage power grid infrastructure.

In order to accurately forecast space weather, we need to improve our ability to forecast space weather propagation through the inner heliosphere. To do so we need the ability to answer these two questions: "When observing space weather as far from the Sun as the Earth, how do we differentiate those features that are due to conditions near their origins at the Sun from those due to propagation effects as they traverse the inner heliosphere?" and "How do we then characterize those propagation effects to improve space weather predictions?"

To address these questions this dissertation investigates three aspects of space weather propagation through the inner heliosphere: **1) How well do heavy ion charge distributions now-cast ICMEs at 1 AU?** Relative abundances of heavy ion charge states remain constant as ions propagate out from the Sun. Thus, observations of these charge states enable the identification of ICME plasma by a feature

which is intrinsic to the conditions at the Sun near the time of their eruption and are unaffected by interplanetary propagation. In a multi-year survey of observations we find the heavy ion charge state ratios of $Fe^{16+\,to\,24+}/Fe_{tot}$, and O^{7+}/O^{6+} are most characteristic to ICME plasma and therefore the most effective at identifying ICMEs in situ. **2) How do arrival time, velocity and intensity of solar energetic electrons compare to modeled magnetic connectivity using ADAPT-WSA vs the Parker spiral?** Near-relativistic electron solar energetic particle (SEP) events propagate through the inner heliosphere along heliospheric magnetic field lines. Previous studies have estimated the field line connections of the propagation paths of these events using the Parker spiral approximation. In a study of six near-relativistic electron events we find that modeling the field line connections between the observing spacecraft and the event's solar origins using ADAPT-WSA improves onset time and intensity profile analysis for spike and pulse type events. **3) How often are counterstreaming (CSEs) and strahl suprathermal electrons (SSEs) observed during in situ observations of ICMEs and what are their characteristics when compared to suprathermal electrons in the solar wind?** Analyzing the occurrence rates and quantitative features of CSEs and SSEs inside of ICMEs compared to those observed in the solar wind outside of ICMEs offers a method of characterizing ICME magnetic topologies. Conducting a fourteen-year survey of in situ observations, we present CSE and SSE occurrence rates using a quantitative classification scheme across a range of widths during ICMEs and during non-ICME solar wind observations. Notably, narrow CSEs with beam widths less than 18° are found to occur nearly exclusively within ICMEs.

In this thesis we analyze in situ observations of space weather to characterize features and quantify correlations which are due to interplanetary propagation effects versus those which are tied to properties near the Sun. We present this analysis and interpret the results in the context of space weather propagation to achieve significant

progress in our understanding of the connection between the Sun and the near-Earth interplanetary environment. This will enable further study that can differentiate propagation effects from those of energization, acceleration and plasma conditions at the solar origins of these space weather events. Ultimately, this research will enhance our ability to forecast space weather propagation through the inner heliosphere.

CHAPTER I

Introduction

1.1 Space Weather Propagation

1.1.1 What is Space Weather?

Exactly as it sounds, space weather is weather in space. In addition to visible and ultraviolet light, the Sun is also continually emitting particles such as electrons and protons (solar energetic particles), x-rays (flares), steady solar wind composed of ionized gas (plasma), and explosive bundles of magnetically bound ionized gas and energy (coronal mass ejections). The collective effects of solar energetic particles (SEPs), coronal mass ejections (CMEs) and solar flares as they reach the near-Earth space environment are known as space weather. The effects of space weather are not limited to space, rather space weather can have damaging impacts on life and weather on Earth.

Space weather is considered geo-effective when the near-Earth space environment, geospace, is noticeably disrupted by these solar influences. This disruption can detrimentally affect both space- and ground-based systems on Earth. There are many ways to define "geospace activity," such as severe distortions of the near-Earth magnetic field, enhancement of space currents and hot particle populations, acceleration of electrons to relativistic speeds to become part of the Van Allen radiation belts, the

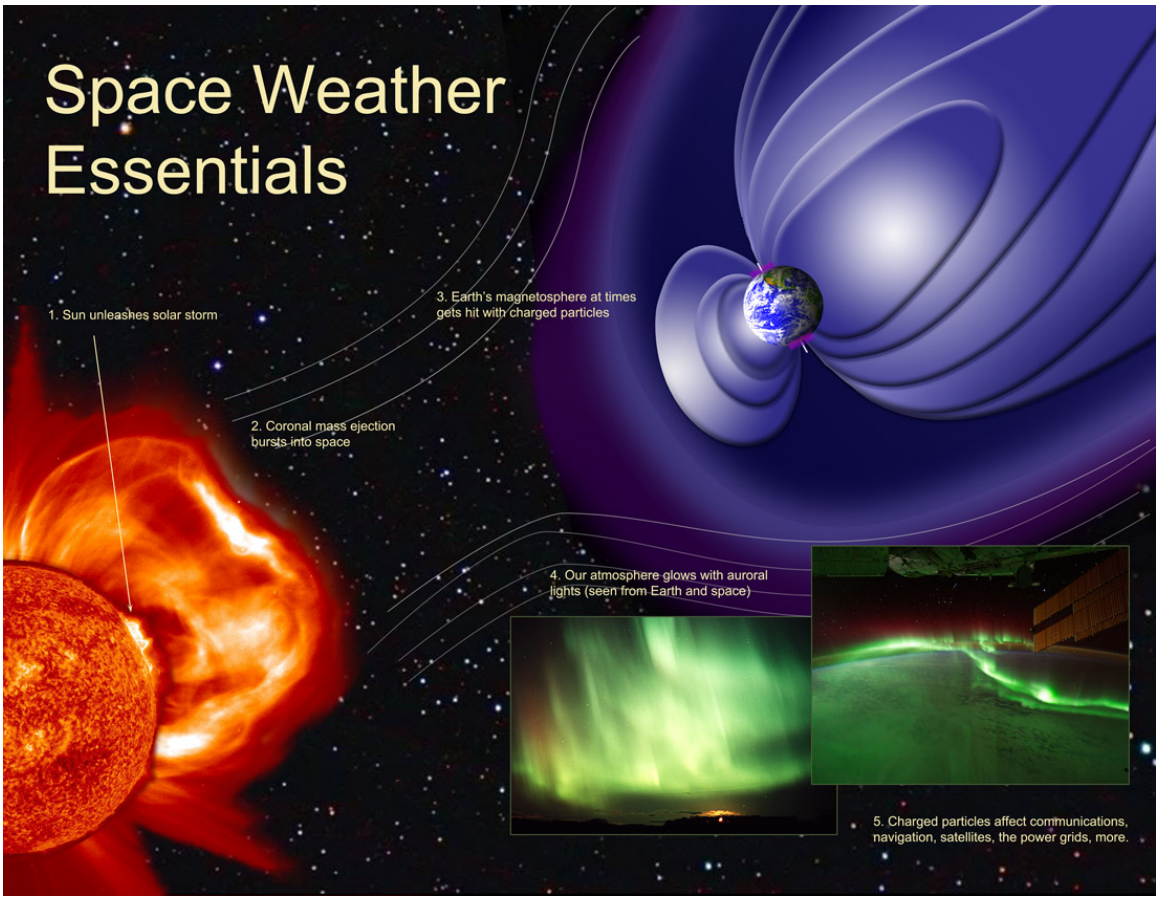

Figure 1.1: Diagram of the path of geo-effective space weather. 1) A solar storm originates at the Sun. 2) A coronal mass ejection (CME) erupts out into the solar system. 3) The CME impacts Earth's protective magnetic shield, the magnetosphere. 4) Charged particles shower down as Aurora in Earth's atmosphere. 5) Charged particles affect satellites and signals for communication and navigation, while radiation harms astronauts and polar flight passengers, while the geomagnetic storm damages the power grid and electrical infrastructure. Image courtesy of NASA.

formation of beautiful auroral displays, and changes to the chemistry and dynamics of the Earth's upper atmosphere. Each of these space weather conditions has an associated solar phenomena that instigate these effects.

When SEPs and solar flares arrive at Earth their energetic particles can cause severe damage to solar panels and electronics onboard spacecraft, and they can dose astronauts and polar flights with harmful radiation. CMEs contain enhanced magnetic fields, and contain billions of tons of hot plasma traveling hundreds of kilometers per second. When CMEs impact Earth's magnetic field, the clash induces geomagnetic storms, which cause the Aurora Borealis and Aurora Australis, damage satellites, cause radio and GPS interference, and induce ground currents which can damage power grid infrastructure. A significant driver guiding much of space weather research is the desire to improve forecasts of space weather events and their effects on Earth.

1.1.2 Likening CMEs to Storms

If you were asked, are you standing in a storm right now? You'd probably be quick to give me an answer, and feel certain you were correct. Information you might use to come to a conclusion might be whether raindrops are falling around you, whether you see storm clouds, and whether you hear thunder or see lightning.

You might become less confident in your answer if you were asked, "Is it a rainstorm or a thunderstorm?" Perhaps you'd think to yourself, "Wait, what is the difference?" or "I don't currently hear thunder so does that make it a rainstorm?" What if the storm clouds remain but it's stopped raining; at what point are you no longer in the storm? What if there is thunder and lightning nearby but no rain? What if it is still raining across the street but not directly above your head? These questions make it quickly apparent how important your definition of a storm is in order to answer the question, "Are you standing in a storm?"

So, now you need to determine what your definition actually is. Perhaps you research what those experts before you have defined. Perhaps, you return to why you need to know whether you're in a storm to decide. Or maybe you choose to focus on what observations you have available to you to decide. Current physical understanding, the particular application, and available observational data, likewise, determine what definition for space weather events is used.

If you are trying to decide whether to cancel an upcoming sailing trip or a sports event, you might not cancel for a rainstorm, but you would be concerned about lightning, so you might cancel for a forecasted thunder storm. Likewise, when forecasting space weather, the important features of the forecast might depend greatly on the application. A satellite operator who is concerned about whether they need to send their spacecraft into a safe-mode to wait out an incoming geomagnetic storm caused by a CME, might have very different concerns than someone working for the National Aeronautics and Space Administration (NASA) wondering if they need to send astronauts on the International Space Station into a radiation shelter.

1.1.3 Making Sense of In Situ Observations

Returning to the comparison of a space weather event with that of a storm on Earth, consider how limited your understanding of a particular storm might be if you only had two points of observation. Say you have one radar measurement that can see an approaching storm at the horizon, and you have one instrument on your roof measuring precipitation, pressure and wind velocity. Imagine your radar measures a huge storm where one region appears to have more heavy rainfall than the rest. Later you compare the radar data you gathered as the storm approaches with the instrument observations on your roof once the storm hit. You notice that the precipitation levels are lower than the heaviest region of the storm. What you cannot determine is whether the precipitation is lower because that region of the storm did not pass over

your roof or whether the storm became less intense by the time it reached you. Research in space weather is likewise made difficult by observations at limited locations. The heliophysics community makes use of both in situ and remote observations of the Sun to study space weather.

Remote observations of the Sun such as those seen by Solar and Heliospheric Observatory (SOHO) and Solar Dynamics Observatory (SDO) make observations of the sun in visible, radio, ultraviolet and extreme ultraviolet light (EUV). A remote CME observation made on December 2nd 2003 is shown in Figure 1.2. The image is a composite of a SOHO white light coronagraph observation of a CME launching into space with an 304 Å extreme ultraviolet image of the Sun. Spacecraft such as SDO and STEREO are equipped with magnetometers which are able to make remote observations of the magnetic field at the surface of the Sun.

In situ observations of the Sun have primarily been dominated by observations about 152 million km from the Sun, or 1 Astronomical Unit (AU), the distance of the Earth from the Sun. STEREO A and STEREO B are spacecraft which travel along an orbit around the Sun similar to Earth's own orbit, traveling in opposite directions ahead and behind Earth. Spacecraft such as the Advanced Composition Explorer (ACE) and WIND have been taking in situ observations at the L1 Lagrange point between the Sun and the Earth, about one hour of solar wind time ahead of Earth. In situ observations are taken using particle, plasma and magnetic field instruments which measure the properties of the solar wind and space weather which directly pass over the spacecraft. Parker Solar Probe (PSP), launched in 2018, and Solar Orbiter, launched in 2020, are new missions which are taking in situ measurements much nearer the Sun. PSP will make it as near as 6.1 million km from the Sun's surface, while Solar Orbiter will get as close as 42 million km to the Sun.

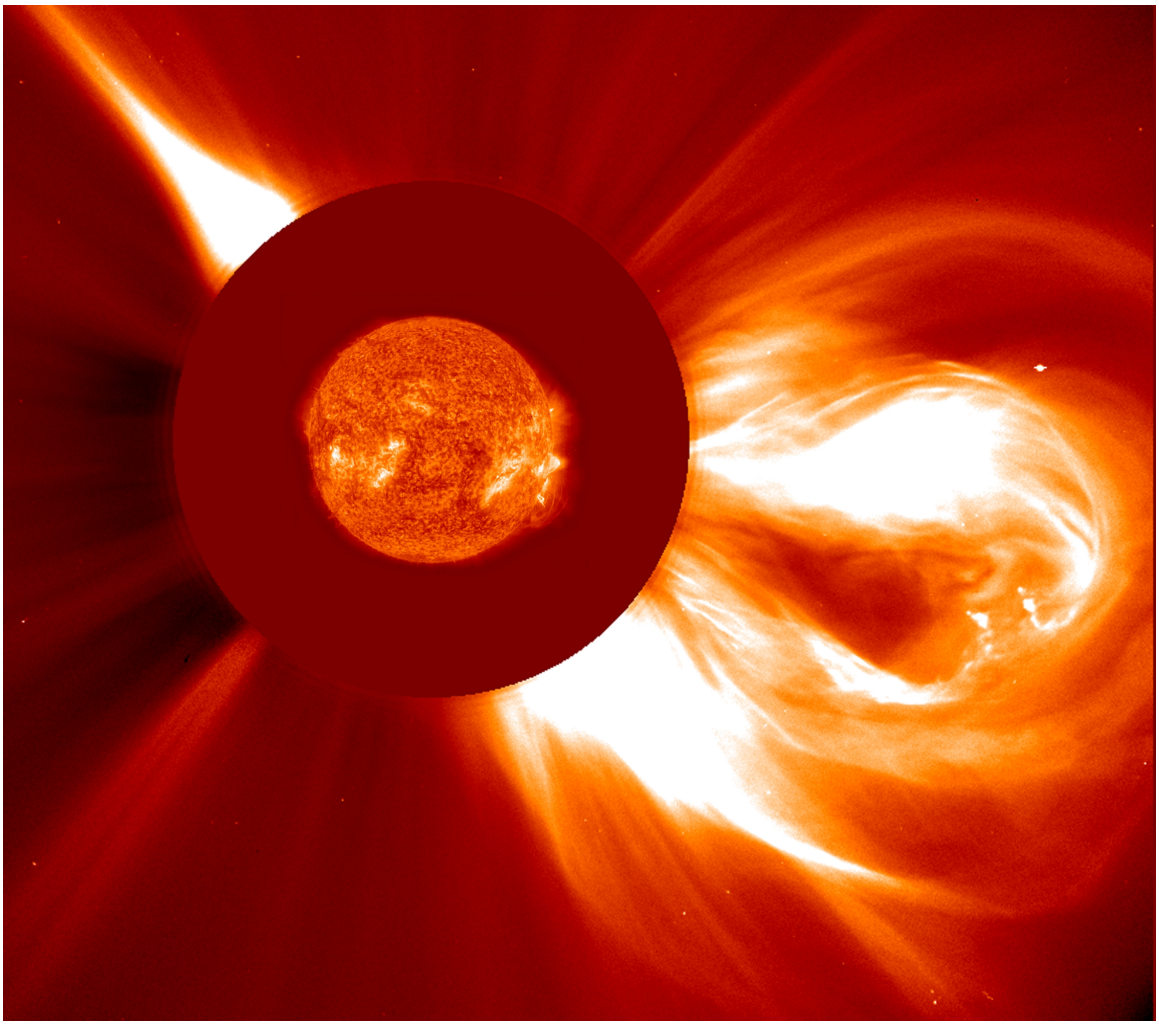

Figure 1.2: Coronal Mass Ejection (CME) observation on December 2nd 2003. This image is a composite of two observations. The outermost image is of a CME launching into interplanetary space observed in white light by the C2 coronagraph of the LASCO instrument on the SOHO. The inner image is a 304 Å observation of the Sun taken by the EIT on SOHO.

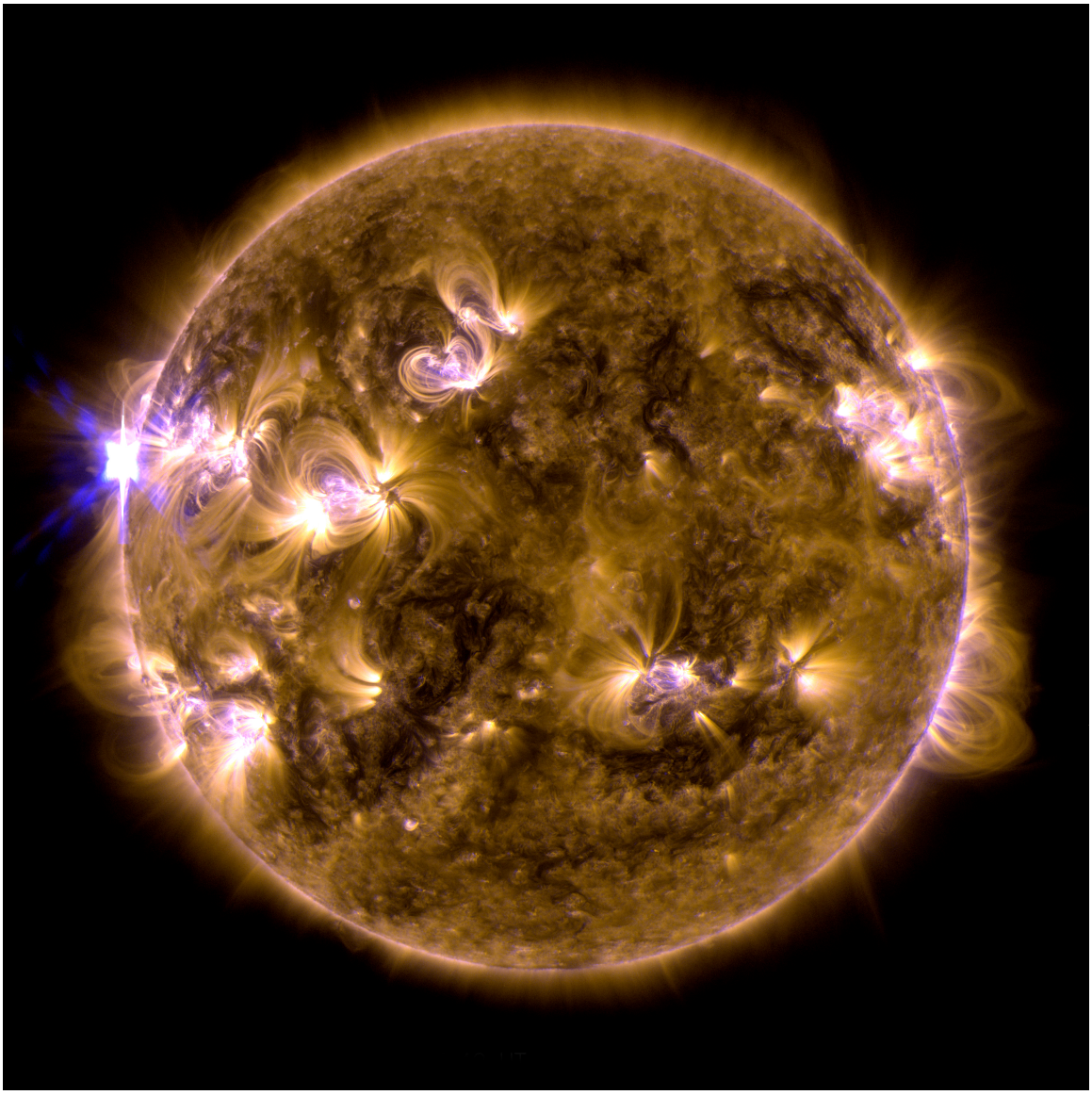

Figure 1.3: X-class solar flare observation on May 13th 2013 taken by NASA's SDO. This is a composite image of the Sun observed in 131 Å and 171 Å EUV light. On the left edge of the Sun an x-class solar flare can be seen. Throughout the image glowing arcades are visible, which are coronal magnetic loops that extend from the Sun's chromosphere up into the low corona.

1.1.4 The Big Challenge

Connecting remote observations at or near the Sun with in situ measurements near the Earth and expanding from the single point in situ spacecraft measurements to understand these spatially vast space weather events remain a big challenge in studying space weather. Without direct measurements how do we study the propagation of space weather events such as SEPs and CMEs after they've left the Sun before they reach our spacecraft near Earth? With only measurements of one path through an event, how do we know how large the event is or how uniform these observed properties are throughout?

The title of this dissertation refers to studying the propagation of space weather in the inner heliosphere. The inner heliosphere, here refers to the inner region of the solar system which contains the Sun, Mercury, Venus and Earth.

Previous space missions, such as Helios 1 (1974-1982), Helios 2 (1976-1981) and Messenger (2004-2015), probed the inner heliosphere. BepiColombo was launched in October 2018 as a joint European Space Agency (ESA) and the Japan Aerospace Exploration Agency mission to Mercury. Two current missions are traveling even closer to the Sun. The NASA launched PSP in August 2018 which aims get as close as 9 solar radii to the Sun. While ESA's Solar Orbiter mission, which launched in February 2020, is set to travel to 60 solar radii from the Sun. The exciting new frontier of in situ observations these missions are offering is unprecedented and already is confirming theories and opening up new questions (*Case et al.*, 2020; *Halekas et al.*, 2020).

Another approach to studying the inner heliosphere is to model the region. This is being done using space weather models such as the Air Force Data Assimilative Photospheric flux Transport - Wang-Sheeley-Arge (ADAPT-WSA) solar wind model, which is discussed further in Section 1.2.3.1, (*Arge and Pizzo*, 2000; *Arge et al.*, 2010), or the Michigan Geospace Model, which is a real-time operational version of

the Space Weather Modeling Framework (SWMF) that was developed at the University of Michigan (*Cash et al.*, 2017). The Michigan Geospace Model is currently being used to forecast space weather at the Space Weather Prediction Center (SWPC) of the National Oceanic and Atmospheric Administration (NOAA). Many additional models for studying space weather, the inner heliosphere and the near-Earth space environment are available for public use at NASA's Community Coordinated Modeling Center (CCMC) at https://ccmc.gsfc.nasa.gov/.

This dissertation uses both in situ observations and modeling to help connect remote and in situ observations while considering the effects of propagation through the inner heliosphere on those observations. As with understanding a storm on Earth, drawing the connections between multiple measurements across time and space are necessary to create a solid framework for understanding the full scale, dynamics and propagation of space weather in the inner heliosphere.

1.1.5 The Sun's Magnetic Field

The Sun's magnetic field extends out throughout the rest of the solar system, to the edge of the heliosphere, its structure determines the propagation of charged particles and plasma as they travel outward from the Sun. This extended magnetic field is known as the heliospheric magnetic field (HMF) or the interplanetary magnetic field (IMF). Here we will treat these two terms interchangeably.

The shape and dynamics of the HMF determine the path of charged particles such as electrons and protons. When discussing the shape of the HMF, the topology of the magnetic field lines is often discussed. Magnetic field lines which are open, trace out from the Sun's surface all the way out to the edge of the heliosphere where they connect with magnetic field lines coming from outside our solar system in interstellar space. Magnetic field lines which are closed loop back towards the Sun and connect back to the surface of the Sun.

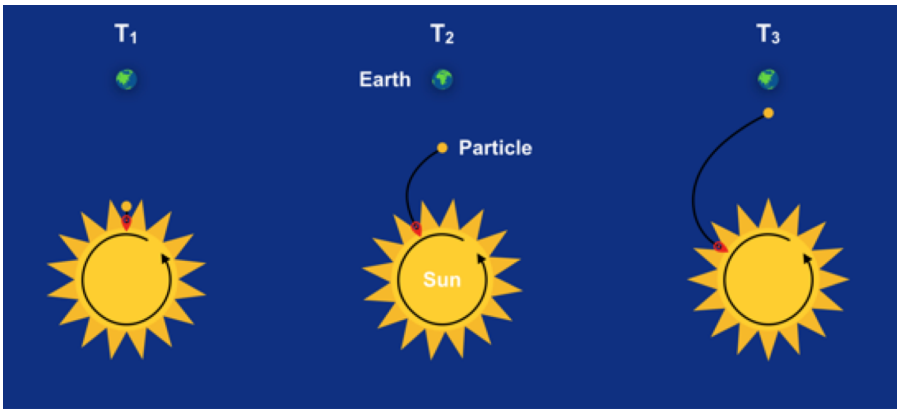

Figure 1.4: Diagram of solar wind particle propagation leading to the formation of the Parker spiral. This diagram represents the path of a particle of solar wind as it leaves the Sun in three subsequent snapshots in time labeled T_1, T_2 and T_3. The solar wind particle is represented by a yellow dot, while its relative path in the Sun's reference frame is traced by a black curve. Though the particle propagates from the Sun radially outward, the Sun rotates out from under it as it travels the great distance to the Earth. By the time the solar wind has reached the Earth, the traced path of its trajectory is a curved spiral. The shape of this spiral path depends on the velocity of the solar wind and the rotation rate of the Sun. The heliospheric magnetic field lines are traced out by the solar wind into this spiral shape. The averaged approximation of the magnetic field lines, which are dragged out by the solar wind along these spiral paths, is approximated by the Parker spiral.

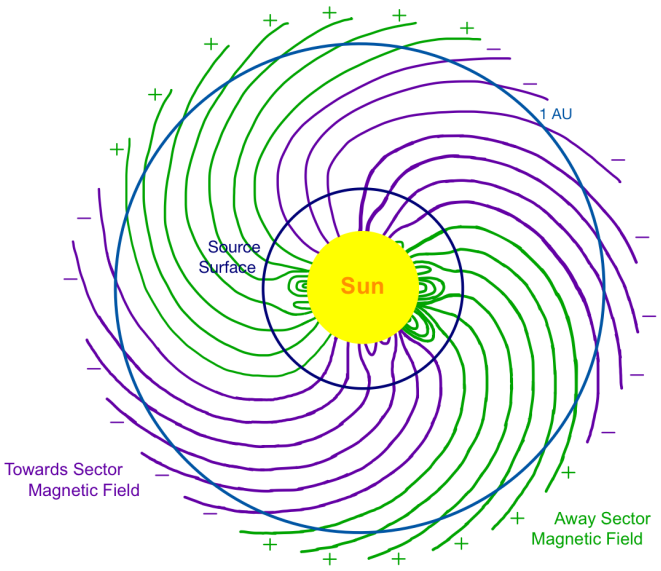

Figure 1.5: Diagram of a simplified Parker spiral HMF in the equatorial plane. Green lines indicate away sector magnetic field lines, while purple lines indicate towards sector magnetic field lines. A navy inner circle represents a potential field source surface, beyond which field lines are assumed to be open and following a Parker spiral. A blue outer circle marks 1 AU from the Sun's center. This diagram is not to scale, nor is it complete, rather it is a simplified sketch to give a rough idea of a four sector Parker spiral HMF with a potential field source surface.

Sunlight travels at the speed of light, 300,000 km/s, radially outward from the Sun, reaching Earth after about 8.3 minutes. Solar wind however, travels more slowly, hundreds of km per second. Though individual solar wind particles travel radially outward from the Sun, in the Sun's reference frame the overall flow of solar wind is curved in an Archimedian spiral (*Parker*, 1959), as depicted in Figures 1.4 and 1.5. The degree of the curvature depends on the solar wind speed relative to the Sun's rotation. For example, at 1 AU, the average solar wind speed is about 400 km/s, as such the degree of curvature in the Parker spiral is typically 45° inclination from the radial. As it flows out from the rotating Sun, the solar wind plasma, or ionized gas, drags out the open HMF lines into this spiral pattern. This overall HMF spiral is known as the Parker Spiral. Some limitations of the Parker Spiral approximation are investigated in Chapter III. Charged particles such as the suprathermal electrons (discussed in Section 1.2.5) and the high energy electrons and protons in SEPs (discussed in Section 1.2.3) are bound to these field lines, and propagate outward in this approximate spiral. While the lower energy solar wind flows radially outward, dragging the magnetic field along.

Understanding how the global picture of the shape and dynamics of the HMF can be tied directly to in situ measurements is a primary goal of this dissertation research. As will be outlined in the next two sections, better characterization of CME plasma which directly ties these events to their solar origins, improved tracing of SEP events to their solar source regions and quantitative analysis of in situ observations of suprathermal electrons which are tied to magnetic field topology are all undertaken in Chapters II, III and IV, respectively, to improve that global picture of the HMF in the inner heliosphere and its connections to space weather propagation.

1.2 Connecting In Situ Observations to their Solar Origins

1.2.1 Solar Wind

The solar wind is the continuous flow of solar plasma out into the heliosphere. The solar wind is the medium through which space weather propagates through the heliosphere. The solar wind is a highly dynamic, magnetized, low density plasma, which is comprised of H^+ (95-98%), He^{2+} (2-5%) and other heavy ions (1%) (*Hundhausen et al.*, 1968). The bulk solar wind is therefore characterized by the density and velocity of its protons. The charge of the electrons and ions in the solar wind is approximately balanced, thus it is considered quasi-neutral. The Sun's HMF is coupled to the Parker spiral path of the solar wind, as the solar wind is frozen-in to the magnetic field (*Alfvén*, 1950), shaping the field as it flows.

Studies investigating the variable magnetic field, plasma heating, particle acceleration, turbulence and wave dynamics in the solar wind are at the cutting edge of plasma physics theory and research. A fundamental question related to the solar wind which remains unanswered to this day is: "How is the solar wind heated and accelerated?" This complicated and dynamic solar wind is the background through which space weather travels in the heliosphere and is the environment within which the research of this dissertation resides.

1.2.2 Interplanetary Coronal Mass Ejections (ICMEs)

CMEs contain enhanced magnetic fields, and contain billions of tons of hot plasma traveling hundreds of kilometers per second. Determining the structure of CMEs when observed in interplanetary space is challenging given the nature of in situ observational data. To differentiate the nature of these observations, we refer to CMEs that are observed in situ in interplanetary space as interplanetary coronal mass ejections (ICMEs). ICMEs fill a large angular extent of the heliosphere as they propagate,

see Figures 1.2 and 1.6, and in situ data come from singular spacecraft providing a 1D observational cut through their 3D structure. Given their extent and the non-uniform spatial variability of their substructure, extrapolating from individual in situ observations to ICME global structure requires indirect information. As will be discussed in Section 1.2.4, ion charge states and plasma properties yield information about the conditions at its solar origins. However, to understand the ICME structure and how it evolves as it propagates through the inner heliosphere, its magnetic field topology must be understood.

While the magnetic field lines of the quiescent solar wind are predominantly open, coronal mass ejections form in closed field regions in the corona. Due to the nature of the 3-dimensional magnetic reconnection that causes the eruption of CMEs from the corona, CMEs contain closed helical loops called magnetic flux ropes (*Gosling*, 2014).

When observing CMEs in coronagraph images such as those in Figures 1.2 and 1.6, one can frequently observe a light-bulb-like structure. This structure typically contains three significant parts, the leading edge with a shock, a cavity where the plasma density is decreased and a denser plasma core. One can see this structure in both Figures 1.2 and 1.6, where the leading shock edge are marked by the bright outermost loop. The bright swath inside the bulb is the plasma core, and the empty section within the bulb is the cavity. This three-part structure is identified in nearly 70% of CMEs observed in coronagraphs (e.g., *Munro et al.*, 1979; *Webb and Hundhausen*, 1987; *Gopalswamy et al.*, 2003). As the CME expands outward through interplanetary space this structure expands. Figure 1.7 is a diagram theorizing how this CME structure is shaped in interplanetary space once it is an ICME, with the leading edge shock shown in blue. The core has expanded behind it. Highlighted in yellow is a coherent magnetic flux rope filling in behind the shock front. Once observed at 1 AU, only 1/3 - 1/2 of ICMEs contain observable flux rope signatures (*Gosling*, 1990).

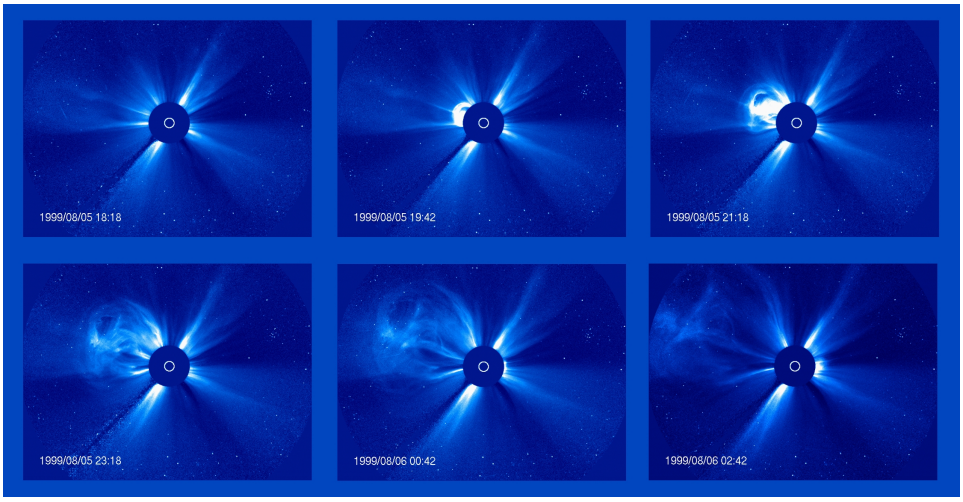

Figure 1.6: Observed coronagraphs from August 1999 of a coronal mass ejection by the LASCO instrument onboard the SOHO. These images were taken using the C3 coronagraph, which observes from 3 to 32 solar radii outward from the Sun. The inner white circles mark the solar surface at 1 solar radius.

1.2.3 Solar Energetic Particles (SEPs)

A major limitation in forecasting geo-effective SEP events is the difficulty modeling propagation through interplanetary space and producing accurate predictions for time of arrival. Whether an event will be geo-effective is highly dependent upon time of arrival. If timing is off a geo-effective event may be incorrectly forecasted to miss Earth entirely or an event may arrive hours ahead of predictions. Improved understanding of how SEP events are affected by intervening magnetic structures and transient events in interplanetary space, and improved understanding of SEP propagation through interplanetary space, could inform forecasting models to improve SEP time of arrival predictions.

SEPs are classified into two primary types based on which physical mechanisms are responsible for their acceleration (*Reames*, 2013). There are impulsive SEPs which are accelerated by impulsive flares or jets, and there are gradual SEPs which are accelerated in shock waves driven out from the Sun by CMEs (e.g., *Lin*, 1970; *Reames*, 2013; *Desai and Giacalone*, 2016). These SEPs can also be differentiated

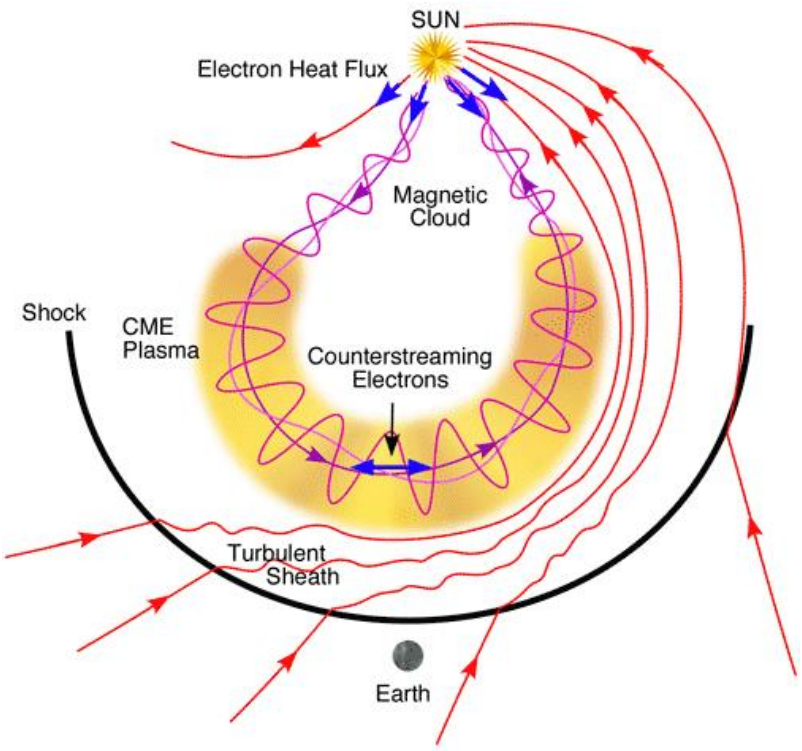

Figure 1.7: A diagram of a "typical" ICME. The yellow region indicates a magnetic flux rope containing closed purple field lines with CSEs. The red lines represent open magnetic field lines with red arrows marking the magnetic field direction. The purple magnetic field lines are closed magnetic field loops which comprise a magnetic flux rope and contain counterstreaming suprathermal electrons. The blue arrows represent sources of suprathermal electrons. The black curve indicates the leading shock front of the ICME. Figure from Zurbuchen and Richardson 2006.

by some associated observations. For instance, impulsive SEPs are associated with enhanced ^{3}He/^{4}He ratios and with Type III radio bursts, which are radio signals that erupt at the Sun. Gradual SEPs are associated with CMEs and with Type II radio bursts (*Reames*, 2013).

Haggerty and Roelof (2009) classified near-relativistic electron (from 10 keV to 100 keV) SEP events into three types: spike, pulse and ramp events. Many have investigated the properties of the more impulsive and short-duration near-relativistic electron SEPs, the electron spike events, (e.g., *Kahler*, 2007; *Kahler et al.*, 2007; *Wiedenbeck et al.*, 2015; *Klassen et al.*, 2012). The SEPT instrument on the STEREO spacecraft measures these near-relativistic electrons from 30 keV to 300 keV (*Müller-Mellin et al.*, 2008).

Electron spike events are spatially correlated with Type III bursts and narrow EUV jets (*Klassen et al.*, 2011, 2012) even while they are not always temporally associated with these eruptions (*Kahler et al.*, 2007), suggesting each are accelerated in the same source regions from the same magnetic reconnection regions but not necessarily the same eruptions (*Klassen et al.*, 2011, and references therein).

Interplanetary propagation effects on spike events are reduced compared to the more gradual ramp events, in fact many spike and pulse events are scatter-free and appear not to experience interplanetary acceleration (*Haggerty and Roelof*, 2009; *Wiedenbeck et al.*, 2015). Near-relativistic electron SEP events can be incredibly valuable for estimating HMF connectivity. When the source location, eruption timing and onset timing are known, one can use impulsive electron spike SEP events to calculate the length of the HMF field lines through which the SEPs propagated (*Kahler et al.*, 2011).

Wang et al. also considered near-relativistic spike and pulse events and evaluated the time delays between the low-energy and near-relativistic electron injections and suggested that the low-energy injections may provide the seed population for the

subsequent near-relativistic electron injection events (2016).

Many current studies investigate the spatial extent and shape of SEP events, considering both how expansive and isotropic they spread from their near-Sun origins (e.g., *Klassen et al.*, 2016, 2018) and how much longitudinal spreading occurs during interplanetary propagation (e.g., *Wiedenbeck et al.*, 2015; *Cohen et al.*, 2017).

Corotating interaction regions (CIRs) and stream interaction regions (SIRs) affect SEP propagation *Richardson* (2004). As shown in Figure 1.8, CIRs contain both rarefaction and compression regions where the shape of HMF open field lines are impacted by the interface of fast and slow solar wind streams. The CIR depicted in Figure 1.8 represents the interaction of two stream interaction regions which form when fast solar wind streams up behind a slow solar wind stream creating a compression interface region between them. When two SIRs interact in this way, they create a rarefaction region between them where magnetic density is decreased. The impact on the shape of the HMF field lines and particle acceleration which can occur in the shocked regions of SIRs plays a role in impacting the interplanetary propagation, scatter and acceleration of SEPs.

1.2.3.1 ADAPT-WSA Modeling

ADAPT-WSA is a coupled model which feeds Global Oscillation Network Group (GONG) magnetograms, which are maps of Earth-based magnetic observations of the magnetic field of the solar photosphere (the Sun's surface,) into the Air Force Data Assimilative Photospheric flux Transport (ADAPT) model whose ensemble of results is fed into the Wang-Sheeley-Arge (WSA) solar wind model to produce an ensemble of solar wind forecasts.

The ADAPT model creates an ensemble of photospheric forecast magnetogram maps based on an assimilation of recent GONG observed magnetograms with older observations that have been modeled forward in time using magnetic flux transport

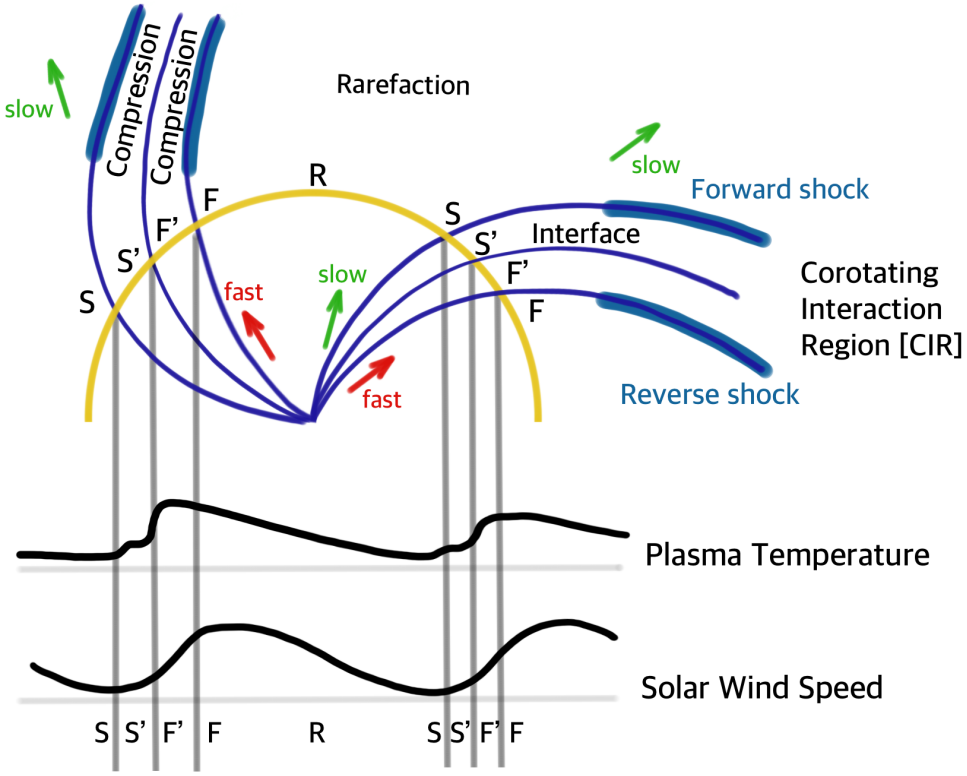

Figure 1.8: Diagram of a CIR in the solar wind. Green and red arrows indicate which regions are driven by slow and fast solar wind, respectively, these solar wind speeds are also marked with S for slow and F for fast. Blue magnetic field lines show the compression regions of bunched magnetic field lines and the rarefaction region between them where the density of magnetic field lines is lower. The golden arc represents the path of a spacecraft which observes the plasma temperature and solar wind speed depicted in black in the lower portion of the diagram. Based on a diagram of a CIR from *Richardson* (2004).

modeling, thus creating a complete photospheric synchronic magnetic forecast map (*Arge and Pizzo*, 2000). ADAPT creates an ensemble of such photospheric forecast maps which differ by random walk variation in the photospheric flux transport modeling. This ensemble of maps is then fed as input into the WSA model (*Arge et al.*, 2010). The WSA model is an empirical solar wind and HMF model, which uses magnetic expansion factor to model from synoptic maps of the magnetic field at the solar photosphere (the Sun's surface) to a 2.5 R_S (solar radii) Schatten current sheet through which all field lines must be open. The WSA model then models field lines out to a potential field source surface at 5 R_S from which all field lines expand outward radially with mapped solar wind velocities and magnetic expansion factor. The WSA model then propagates the solar wind out in an equatorial plane incorporating stream interaction regions and sometimes transient events such as CMEs (*Arge and Pizzo*, 2000). When coupled with ADAPT, the WSA model uses each ADAPT forecasted synoptic magnetic map to create the Schatten current sheet and potential field source surfaces, modeling forward the solar wind out throughout the heliosphere along the equatorial plane, resulting in an ensemble of solar wind and HMF forecasts in the equatorial plane (*Arge et al.*, 2010; *Arge et al.*, 2011).

As discussed in Section 1.1.5 heliospheric magnetic field lines are shaped into a spiral pattern known as the Parker spiral. The curvature of those field lines is dependent on the velocity of the solar wind that shaped them. Faster solar wind forms a more stretched out spiral path, whereas slower solar wind forms a tighter spiral. When streams of faster solar wind come up behind streams of slower solar wind, the interaction forms a region of enhanced pressure, this is known as a stream interaction region or a CIR. Figure 1.8 diagrams the compression and rarefaction regions of a CIR. The diagram also marks the interface boundary between the S' (formerly slow) and F' (formerly fast) compressed solar wind of the interaction region. The plasma density spikes in the S' regions of the CIR, while the magnetic field intensity

is increased in both the S' and F' streams.

The WSA model portion of ADAPT-WSA incorporates the changes in solar wind velocity, magnetic field intensity and plasma density due to CIRs and models the HMF accordingly, therefore allowing for the WSA modeled global HMF to differ from a general Parker spiral. This important feature of ADAPT-WSA will become relevant in Chapter III.

1.2.4 Heavy Ion Charge States in the Solar Wind

Atoms of elements such as helium, oxygen, carbon, and iron rise out of the Sun's interior convective zone and are ionized in the Sun's atmosphere, i.e. the chromosphere and lower corona of the Sun, before they propagate through the heliosphere (*Gosling*, 2014). Collisional ionization, when electrons collide with ions in the plasma, occurs in the low corona, including along coronal magnetic loops, such as those which can be seen in the observations of Figures 1.3 and 1.9 (*Gruesbeck et al.*, 2011, and references therein). The charge state of an ion is simply the difference between the number of protons and the number of electrons. The high temperature of the plasma in the corona ($\sim 10^6$ K), where these loops reside, heats and strips atoms of their electrons, ionizing them into higher charge states of ions (*Ko et al.*, 1997; *Landi et al.*, 2012).

The energies required for ionization differ for each element. The first ionization potential (FIP) value of an element is the lowest energy required to strip it of one electron and ionize it to its 1+ charge state. Some elements are known as low-FIP ions, such as Mg, Si and Fe. Low-FIP elements require energies < 10 eV to ionize to their lowest states and are thus able to ionize easily in the low solar chromosphere. Low-FIP ions are then quickly convected up into the low corona by resonating Alfvén waves, where they are further ionized into higher states by the higher coronal temperatures at higher altitudes. High-FIP elements, however, such as He, C, O, and Ne, require

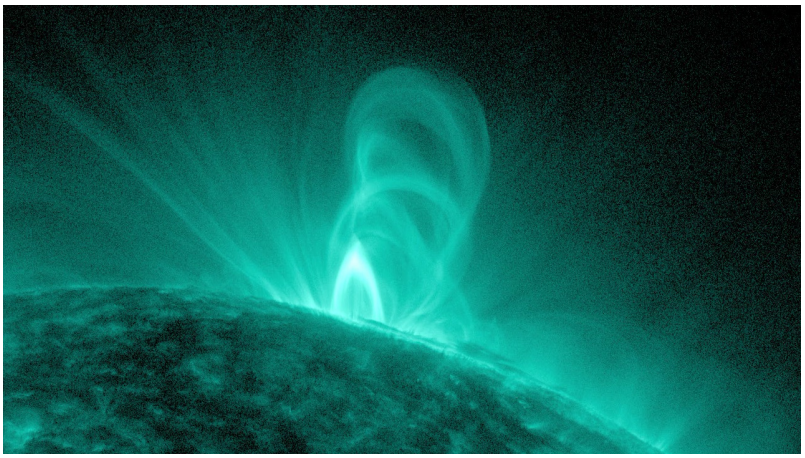

Figure 1.9: SDO AIA observations of coronal loops in 131 Å EUV on July 18th 2012.

energies > 10 eV to ionize and take longer to be swept up into the corona to be ionized, resulting in lower abundances of ions of these elements (*Reames*, 2018). The fractionation this has on the relative abundances of these elements is known as the FIP effect.

As ions are heated in the solar corona, the abundances of higher charge states increases. The highest charge state an element can reach in the solar corona is dependent on the electron temperature and electron temperature in the surrounding environment (*Ko et al.*, 1997; *Landi et al.*, 2012). At any given coronal temperature, the highest available charge states vary for different elements. For example, the temperature required to ionize oxygen to its 8+ charge state is around $\sim$2.5 x 10^6 K (*Rakowski et al.*, 2007).

As solar magnetic field lines expand out into the heliosphere as the HMF or as part of the magnetic flux rope of an ICME, the density drops to the point where further ionization and recombination can no longer take place (*Landi et al.*, 2012). Thus the ratios of high charge states to low charge states for any given ion remains fixed as it propagates throughout the heliosphere. The point at which solar wind expansion causes the electron density in the solar wind to drop so that ionization ceases and the ratios of charge states no longer changes as it propagates through the heliosphere is

known as the freeze-in point (*Hundhausen et al.*, 1968; *Ko et al.*, 1997). The distance at which this occurs does differ for different elements and plasma conditions, but has effectively ceased for solar wind elements by 4 R_S (*Rakowski et al.*, 2007).

Plasma accelerated along open magnetic field lines that quickly flows through the low corona out as solar wind, does not always have enough time to reach a state of ionization equilibrium, and the relative levels of high charge states for given elements might be lower than the coronal temperatures through which they crossed would otherwise have indicated (*Stakhiv*, 2016; *Reames*, 2018). Thus, the resulting charge state ratios associated with SEP events in combination with analysis of the FIP fractionation, (an increase in the relative abundance of low-FIP elements,) can give an indication of the conditions through which their seed populations were accelerated (*Reames*, 2018).

For example, as will be discussed further in Chapter II, ratios of O^{7+} compared to O^{6+}, C^{6+} compared to C^{5+} and Fe ions 16+ and greater compared to the average Fe charge state, are each enhanced in plasma observed during ICMEs (*Lepri et al.*, 2001; *Lepri and Zurbuchen*, 2004; *Gilbert et al.*, 2012, and references therein). The temperatures and plasma conditions as CMEs form in the low corona are such that these particular charge states are enhanced. This will be discussed in Section 1.3 and will be analyzed in Chapter II.

As can be seen in Figure 1.10, modeling of CMEs using the MHD-on-A-Sphere (MAS) model has produced predictions as to the distribution of heavy ions throughout a CME (*Lynch et al.*, 2011). The subplots a - d of Figure 1.10 show the modeled distribution maps within a CME erupting to the right for ions with charge state ratios of C^{6+}/C^{5+}, O^{7+}/O^{6+}, Si^{12+}/Si^{11+}, and $Fe^{\geq 16+}/Fe_{\text{total}}$ respectively. Knowing which portions of an ICME that one is observing when studying in situ observations can offer great insights into how an ICME evolves as it propagates through the inner heliosphere. With insight from such modeling predictions, heavy ion charge state

observations can be used to probe the properties of the plasma within ICMEs and gain insights into the solar conditions and solar source regions of the plasma swept up into that portion of the ICME. This analysis of ICME substructure using heavy ion ratios, can then be reinforced with modeling predictions using ionization rate calculations, such as those discussed by *Rivera et al.* (2018). This will be further discussed in Chapter II.

Analyzing the elemental abundances, charge state ratios and FIP fractionation of in situ plasma observations offers a method to probe the coronal temperatures, acceleration and unique plasma conditions in the low corona at the solar origins of the plasma, independent of its propagation through the heliosphere.

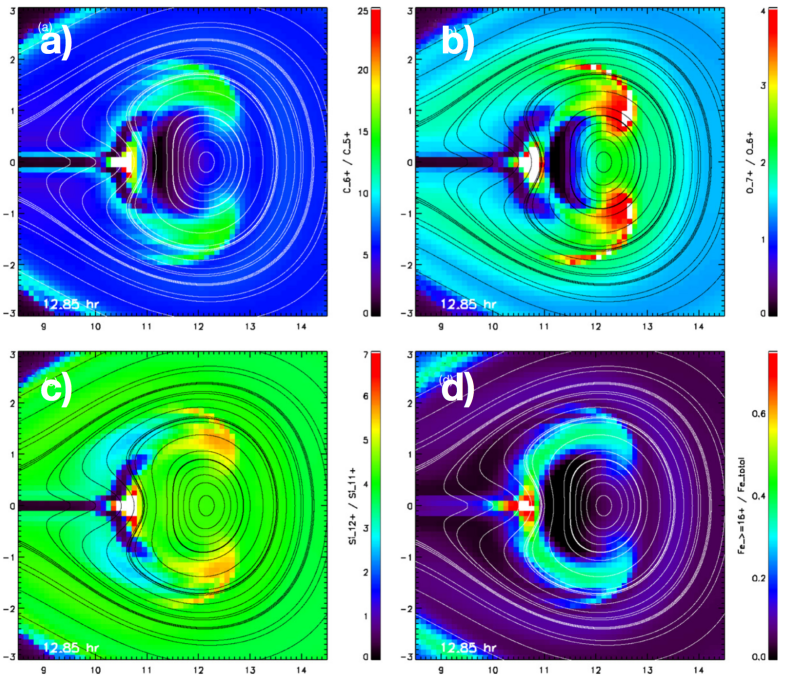

Figure 1.10: Simulated spatial distribution map of heavy ion charge state parameters during an MAS simulation of a CME. These modeled results represent an axisymmetric cone-shaped CME erupting to the right 12.85 hours into the simulation time. Higher charge state ratios are red while lower charge state ratios are blue. Each subplot maps a different charge state ratio: a) C^{6+}/C^{5+}, b) O^{7+}/O^{6+}, c) Si^{12+}/Si^{11+}, d) $Fe^{\geq 16+}/Fe_{total}$. Figure adapted from *Lynch et al.* (2011).

1.2.5 Suprathermal Electrons

Solar wind suprathermal electrons (E > 70 eV) observed in situ at 1 AU flow in field-aligned beams through the heliosphere. These electrons are fast, with speeds at least 10 times greater than the normal solar wind flow. For this reason they are optimal tracers of magnetic field topology in the inner heliosphere. Due to adiabatic expansion the distribution of pitch angles of suprathermal electrons (SEs) narrow towards 0° when parallel to the magnetic field or 180° when anti-parallel. Without scattering processes, by 1 AU the width of the pitch angle distribution (PAD) would be <1°. Different scattering processes, such as shocks, wave interactions, and irregularities in the heliospheric magnetic field scatter or reflect the electrons, causing the PAD to widen or narrow, or causing drop outs around 90° pitch angles. We refer to SE PADs with narrow, unidirectional beams about 0° or 180° as strahl suprathermal electrons (SSEs). Whereas SEs which travel both parallel and anti-parallel to the magnetic field with narrow PADs about both 0° and 180° are CSEs. CSEs indicate closed field lines with SE sources at both magnetic footpoints at the Sun, which are correlated with ICME observations.

When one measures the energy distribution function of observed solar wind electrons, there are three portions of the distribution. There are the thermal population of electrons, which are the bulk flow of electrons, but there are also two populations of electrons that extend beyond this thermal population, which are therefore suprathermal (*Crooker et al.*, 2002; *Vocks et al.*, 2005, 2016, and references therein). The beam population of suprathermal electrons form a bump on the higher energy side of the electron velocity distribution function, as shown in Figure 1.11. This population of suprathermal electrons form the suprathermal electron strahl. Additional suprathermal electrons form the diffuse halo, a population of scattered suprathermal electrons which are isotropically distributed in pitch angles and form a high energy tail to the distribution of solar wind electrons.

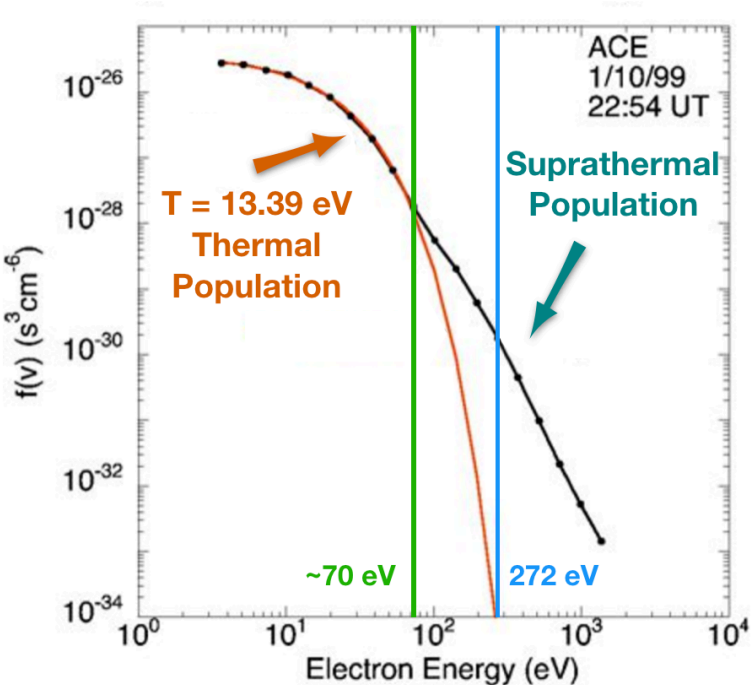

Figure 1.11: This figure depicts the velocity distribution function of the thermal core population of electrons compared to the suprathermal tail population of electrons as observed by the ACE spacecraft at L1 on 1 October 1999 at 22:54 UT. The orange line shows the Maxwellian fit for a core thermal population at T = 13.39 eV. Around 70 eV the observed distribution of electrons, represented in black, diverges from the thermal Maxwellian fit in orange. These additional electrons at these energies just above thermal core electrons form the suprathermal tail. At L1 the suprathermal tail begins with electron energies around 70 eV and at $\geq$272 eV the observed electron population is almost exclusively suprathermal. Figure adapted from *Gosling* (2014).

The highly idealized case for how to interpret SE PADs is shown in Figure 1.12. This picture compares an idealized PAD plot of pitch angle versus time with suprathermal electron flux represented with a rainbow color bar. These idealized PADs map to particular magnetic field topologies, A, B, C or D. Ideally unidirectional beams of SEs are strahl and are either anti-aligned as with case A, or aligned as with case C with their magnetic field lines. A disconnected field line which has no source of SEs from the Sun would have no SE signature as seen with case D. Case B shows the CSE case when a closed magnetic field loop has solar sources of SEs along both magnetic footpoints and therefore has a very clear counterstreaming signature of two beams with electron flux along both 0° and 180°. Thus, suprathermal electron PADs can be used to probe the magnetic topology of the inner heliosphere.

While Figure 1.12 demonstrates the connection between SE PAD observations and corresponding magnetic field topology, it leaves off the more complicated cases. This standard set of cases does not address how to handle observations of isotropic fully-scattered PADs, how to interpret asymmetric counterstreaming or how to identify broadened CSEs from 90° PAD depletions (*Gosling and Skoug*, 2002). As will be discussed in Section 1.3 and presented in Chapter IV, this dissertation seeks to provide a system of more complex SE PAD characterization which enables improved analysis of SE observations and modeling of magnetic topology.

The magnetic mirror force in conjunction with the adiabatic expansion of the heliospheric magnetic fields as they expand out into the heliosphere result in adiabatic focusing of suprathermal electron populations (*Rosenbauer et al.*, 1977). Scattering processes counteract this focusing and broaden PADs. Such processes include Whistler mode wave-particle interactions (*Gary and Li*, 2000) and Coulomb collisions (*Pagel et al.*, 2007). Thus, suprathermal electron PADs retain information about the interplanetary conditions through which they have propagated. Studies have been undertaken to investigate the impacts of SIRs (e.g., *Steinberg et al.*, 2005), whistler

waves (e.g., *Gary and Li*, 2000), and coulomb collisions (e.g., *Ogilvie et al.*, 2000; *Pagel et al.*, 2007) on suprathermal electrons in the solar wind.

1.3 Relevant Open Questions in Heliophysics

1.3.1 ICME Forecasting

How well do heavy ion charge distributions now-cast ICMEs at 1 AU?

Observations of certain charge state parameters in solar wind plasma can be tied to plasma conditions at the solar origins of the solar wind, as described in Section 1.2.4. Such plasma conditions which enhance ionization of certain ion charge states relative to others are known to correlate with ICME observations (e.g., *Lepri et al.*, 2001; *Lepri and Zurbuchen*, 2004; *Gilbert et al.*, 2012). What remains open for investigation is the effectiveness of now-casting ICMEs using heavy ion charge states alone. We selected six charge state parameters to test: the average Fe charge state ($< Q_{Fe} >$), $Fe^{16+\,to\,24+}/Fe_{tot}$, O^{8+}/O^{6+}, O^{7+}/O^{6+}, C^{6+}/C^{5+}, and C^{6+}/C^{4+}.

We aim to now-cast ICMEs using heavy ion charge states which could be used to identify in situ ICMEs in real-time, if observations were included in real-time space weather monitoring observations. This would be beneficial for forecasting ICMEs at Earth, given that L1 is approximately an hour upstream of Earth, now-casting at L1 could give an hour's lead time for ICME forecasting at Earth. Now-casting is helpful for understanding the current local environmental conditions and the risks that disturbances pose to humans, space- and ground-based technologies, and infrastructure operating under the influence of the changing space environment. For example, the distribution of mass within an ICME, and thus its mass-loading on a system, can be underestimated if only the proton parameters are considered (*Kozyra et al.*, 2013, e.g.).

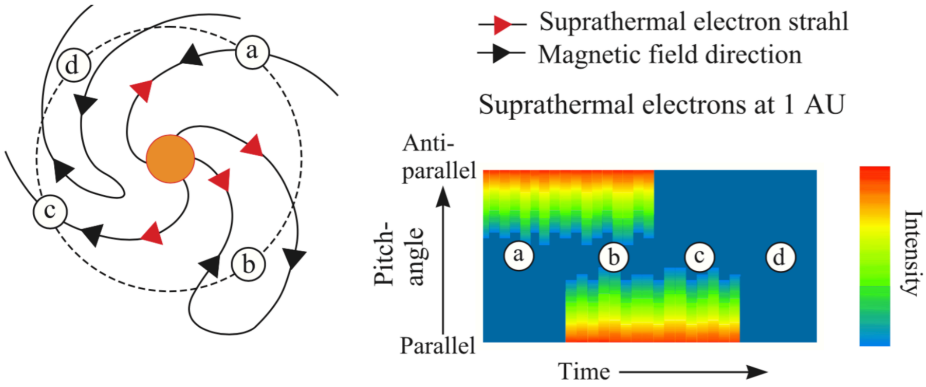

Figure 1.12: Diagram of heliospheric magnetic field lines and the corresponding idealized observations of suprathermal electron PADs. Region A & C: Open field lines with SSEs. Region B: Closed field lines with CSEs. Region D: Disconnected field lines with no suprathermal electron source. Figure from *Owens and Forsyth* (2013).

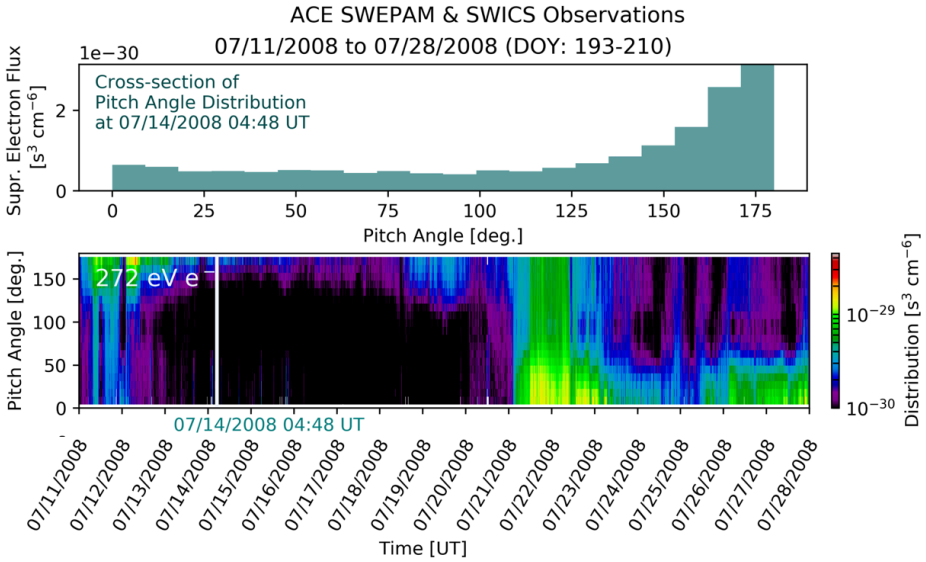

Figure 1.13: ACE SWEPAM observations of 272 eV SEs spanning 11 July 2008 to 28 July 2008. This period of solar wind observations does not contain an ICME. The lower panel plot shows the observed SE pitch angles versus time with the rainbow color bar representing the SE flux for each pitch angle bin. The vertical white line in the lower panel marks the location of the PAD cross-section shown in the panel above. This top panel presents the SE flux for 0° to 180° of observed SE pitch angles on 14 July 2008 at 04:48 UT. Given the singular unidirectional beam of field-anti-aligned SEs, this cross-section is an observation of SSEs.

1.3.2 Propagation of SEPs

How do arrival time, velocity and intensity of SEP electrons compare to modeled magnetic connectivity using ADAPT-WSA vs Parker Spiral?

Features of SEPs which are still open topics of investigation are tracing the HMF and their propagation paths through interplanetary space, the full shape and spatial extent of SEP events, and the impact of the heliospheric current sheet (HCS) on their intensity profiles.

As discussed earlier in Section 1.2.3, SEPs can be classified into two primary types: impulsive and gradual. The seed populations, plasma conditions at their origins, and probable acceleration mechanisms have been investigated (*Cohen*, 2016; *Reames*, 2018, and references therein). Recent studies often seek to factor in propagation effects and investigate how to validate assumptions about magnetic connectivity and solar origins (*Klassen et al.*, 2016; *Wiedenbeck et al.*, 2015, e.g.).

Distinguishing between features of in situ observations due to acceleration mechanisms, seed populations and propagation effects is a complex problem to address. For instance, electron spike events are frequently observed with impulsive SEP events, yet an investigation by Kahler et al. 2007, found the electron spike and pulse events are unlikely to be further accelerated during propagation through the inner heliosphere.

From early research through current research today, authors investigating SEPs often rely on the Parker spiral approximation when considering the magnetic connectivity of magnetic field lines from observation to solar source region (*Lin*, 1985; *Cohen et al.*, 2017; *Klassen et al.*, 2015, 2016, 2018, e.g.). ADAPT-WSA modeling in contrast includes SIRs to consider variation of the HMF. The investigation presented in Chapter III seeks to address the open question regarding the accuracy of the Parker spiral approximation when determining SEP magnetic connectivity. To that aim, additional more specific questions are addressed, including the following:

- How greatly does the inclusion of HMF variation due to CIRs impact calcu-

lations of HMF footpoints at the Sun? How does this impact our picture of interplanetary SEP propagation?

- Is the impact greater for electron spike events which show evidence of interplanetary particle acceleration versus gradual events which are CME shock-accelerated?

- How close to the associated flare are the modeled origins for impulsive events?

1.3.3 Magnetic Connectivity and Substructure of ICMEs

How often are CSEs and strahl observed during in situ observations of ICMEs and what are their characteristics when compared to suprathermal electrons in the solar wind?

CSEs have long been shown to be associated with interplanetary coronal mass ejections (ICMEs) (*Gosling*, 1990), while unidirectional SSEs have long been known to be associated with open magnetic field solar wind. Streaming of both aligned and anti-aligned suprathermal electrons is theorized to occur along closed magnetic fields which maintain footpoint connections at the Sun on both ends, which act as sources for the streaming SEs (*Gosling et al.*, 1987).

To better characterize SE PAD width observations and enable better characterization for comparison to other observational studies, this study seeks to quantitatively define not only a range of widths which could be defined as strahl, but to quantify the actual individual occurrence rates of various beam widths for both SSEs and CSEs during ICMEs and during non-ICME times.

Characterizing the expected PAD signatures on closed field magnetic structures, and distinguishing which features are unique to closed fields specifically gives a foundational basis to distinguish between each of these structures and will lead to the ability to more conclusively identify magnetic topology. The analysis in this study

seeks to offer that quantitative definition to build upon with subsequent research.

This study seeks to quantitatively characterize the PADs of observed suprathermal electrons in the solar wind compared to those observed during ICMEs. This preliminary study uses suprathermal electron pitch angle observations by the ACE Solar Wind Electron, Proton, and Alpha Monitor (SWEPAM), which will be described in Section 4.4.1. The overall survey results are presented in Section 4.5. This observational survey gives an indication of the range of the widths of observed SSEs and CSEs and how those widths vary from observations during ICMEs compared to observations outside of ICMEs using two published ICME databases, which will be described in Section 4.4.1. The occurrence rates presented in Table 4.1 vary depending on what quantitative parameters for counterstreaming are used. This investigation produces cross-sections of the PADs so that quantitative thresholds such as those used for Table 4.1 or by *Anderson et al.* (2012) can be defined by quantitative features which can be compared across solar wind conditions, ICME substructure, and magnetic topologies.

1.4 Dissertation Outline

Chapter I contains the introduction for this dissertation. This introduction includes background information on space weather, in situ observations in the inner heliosphere and current relevant open questions in heliophysics.

Chapter II contains a journal article titled "Now-Casting Interplanetary Coronal Mass Ejections Using Heavy Ion Charge Distributions," which was submitted to American Geophysical Union's peer-reviewed Space Weather.This chapter presents a study which evaluates quantitatively the effectiveness of six heavy ion charge state parameters at now-casting interplanetary coronal mass ejections at L1. By using statistical metrics to evaluate across a range of possible thresholds for each parameter, the study identifies how effective each parameter could be, and which thresholds are the optimal choices for ICME now-casting depending on user needs. This study is the

first of its kind to evaluate the effectiveness of identifying ICMEs solely using charge states across such an extended multi-year survey which spans a complete solar cycle. Chapter II answers the following science question established in Section 1.3.1: **How well do heavy ion charge distributions now-cast ICMEs at 1 AU?**

Chapter III is titled "Characterizing Magnetic Connectivity of Solar Flare Electron Sources to STEREO Spacecraft Using ADAPT-WSA Modeling," which is based on a research paper submitted under the same title to be published in the American Geophysical Union's Journal of Geophysical Research: Space Physics. This study uses a combination of in situ observations of six SEP events which were observed by two or more satellites and solar wind modeling, to trace from 1 AU observations back to the solar origins of the SEP events and compare those origins to the Parker Spiral predicted magnetic connectivity. This study seeks to evaluate how well the Parker Spiral approximates the magnetic connectivity compared to ADAPT-WSA modeling using in situ observations at multiple spatially separated observation points 1 AU from the Sun. Chapter III answers the following science question established in Section 1.3.2: **How do arrival time, velocity and intensity of SEP electrons compare to modeled magnetic connectivity using ADAPT-WSA vs Parker Spiral?**

Chapter IV presents a study titled "A Characterization of Counterstreaming Suprathermal Electrons and Their Correlation with Interplanetary Coronal Mass Ejections 1998 - 2011," which was submitted to be published in the American Geophysical Union's Journal of Geophysical Research: Space Physics. This chapter quantitatively characterizes the occurrence of counterstreaming suprathermal electrons over a complete solar cycle using in situ observations from NASA's Advanced Composition Explorer satellite from 1998 - 2011. While counterstreaming suprathermal electrons are known to occur during ICMEs and are expected to indicate closed magnetic field connections, this is the first study to actually quantitatively characterize

the occurrence rate of counterstreaming and strahl of differing widths for both ICME and solar wind observations over a fourteen-year study that spans a complete solar cycle. Chapter IV answers the following science question established in Section 1.3.3: **How often are CSEs and strahl observed during in situ observations of ICMEs and what are their characteristics when compared to suprathermal electrons in the solar wind?**

CHAPTER II

Now-Casting Interplanetary Coronal Mass Ejections Using Heavy Ion Charge Distributions

2.1 Preface

This chapter presents a study which evaluates quantitatively the effectiveness of six heavy ion charge state parameters at now-casting ICMEs at L1. By using statistical metrics to evaluate across a range of possible thresholds for each parameter, the study identifies how effective each parameter could be, and which thresholds are the optimal choices for ICME now-casting depending on user needs. This study is the first of its kind to evaluate the effectiveness of identifying ICMEs solely using charge states across such an extended multi-year survey which spans a complete solar cycle.

2.2 Abstract

Enhancements in high charge states of heavy ions, as identified by increases in the ratios of ions such as $Fe^{\geq 16+}/Fe_{tot}$, O^{8+}/O^{6+}, O^{7+}/O^{6+}, and C^{6+}/C^{5+}, have been shown to consistently occur during Interplanetary Coronal Mass Ejection (ICME) space weather events. The presence of these ions is due to increased ionization attributed to enhanced heating and enhanced densities associated with erupting struc-

tures at the Sun during the initiation and release of ICMEs. We present a retrospective study using in situ data at L1 from the Solar Wind Ion Composition Spectrometer (SWICS) on the Advanced Composition Explorer (ACE) spacecraft. We analyze rates of event identification based on heavy ion charge distributions compared with published ICME databases using the Heidke skill score and additional metrics using Receiver Operating Characteristic (ROC) curves. Identifying events spanning 1998-2011, we evaluate a spread of thresholds to assess the feasibility of using solar wind heavy ion charge distributions of iron, carbon and oxygen to now-cast the arrival of ICME space weather events at Earth. We find that the best ICME identifiers were $Fe^{16+\,\mathrm{to}\,24+}/Fe_{\mathrm{tot}}$ and O^{7+}/O^{6+}. Three optimal threshold choices were found for each parameter, with the optimal choice varying based on user need.

2.3 Introduction

Coronal mass ejections are powerful eruptions that are generated by the catastrophic release of stored magnetic energy and massive amounts of plasma from the solar corona. While the exact details of the mechanisms of their release still remain an ongoing key research area in solar physics, the gravity of their impact on the space environment, particularly the near-Earth space environment, is well appreciated. Energetic particles and radiation accelerated during coronal mass ejections and solar flares can be vital in forecasting whether a coronal mass ejection propagating through interplanetary space, i.e. an interplanetary coronal mass ejection (ICME), is earthward bound, and can give advanced warning of as little as 20 minutes for the most energetic radiation to as much as several days warning of the impending ICME arrival at Earth (e.g., *Webb et al.*, 2000; *Zhang et al.*, 2007). In situ identification of ICMEs, i.e. attempting to understand if a given spacecraft or solar system body is immersed inside an ICME using in situ observations can also aid in confirming and constraining forecasts and provide another way of determining if a space weather

disturbance is propagating along a given path.

Now-casting is when one uses forecasting methods to create a prediction for the current time. For this study, we aim to now-cast ICMEs using heavy ion charge states which could be used to identify in situ ICMEs in real-time, if observations were included in real-time space weather monitoring operations. This would be beneficial for forecasting ICMEs, given that L1 is approximately an hour upstream of Earth, now-casting at L1 could give an hour's lead time for ICME forecasting at Earth. Now-casting is helpful for understanding the current local environmental conditions and the risks that disturbances pose to humans, space- and ground-based technologies, and infrastructure operating under the influence of the changing space environment. For example, the distribution of mass within an ICME, and thus its mass-loading on a system, can be underestimated if only the proton parameters are considered (*Kozyra et al.*, 2013, e.g.).

Solar wind composition has shown itself to be a reliable tracer of different solar wind structures and solar source regions, and reveals important insights about processes in the corona. Unusually high charge state ion composition signatures in the solar wind can be reliably traced to material associated with ICMEs. For instance unusually highly ionized atoms of Fe or other heavy elements almost always only appear inside ICMEs (e.g. *Gruesbeck et al.*, 2011, 2012; *Lepri et al.*, 2001; *Lepri and Zurbuchen*, 2004, 2010; *Zurbuchen and Richardson*, 2006, and references therein), and unusually low charge state ions of solar origin are almost always related to cold, dense structures associated with a select set of prominence-related ICMES (*Lepri and Zurbuchen*, 2010; *Gilbert et al.*, 2012, and references therein). The unique ability to use solar wind charge state information to identify ICMEs, based on the finding that 95% of ICMES exhibit unusually elevated Fe charge states (*Gruesbeck et al.*, 2011), make solar wind composition a prime candidate for ICME now-casting. For example, ACE observations of enhanced heavy ion charge distributions in panels G through K

can be identified in Figure 2.1 at the onset of an ICME, marked with a red vertical line, on 19 February 2003.

To date, there has not been a systematic study of charge state composition over a full solar cycle of observations. This work presented below conducts such a study. The hypothesis that we are testing is this: can we identify ICMEs strictly using heavy ion charge state analysis? If so, then this opens a new method of now-casting ICMEs as they are observed in situ between the Sun and the Earth. The study presented below uses parameters from ions of three elements, specifically iron, carbon, and oxygen, for which abundant and reliable in situ charge state data are available.

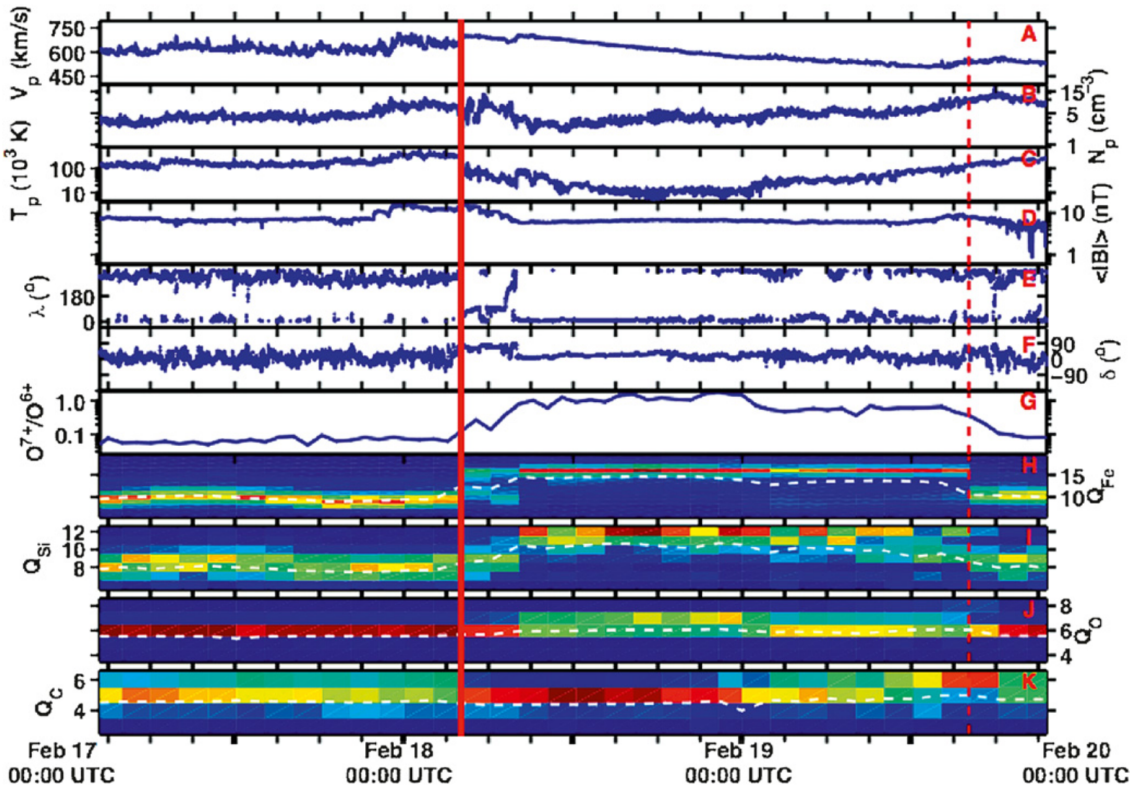

Figure 2.1: ACE in situ observations of plasma properties at the onset of an ICME on 19 February 2003. Adapted from *Gruesbeck et al.* (2011).

2.4 Data and Event Analysis

As discussed in the Introduction, Section 2.3, observations of certain charge state parameters in solar wind plasma can be tied to plasma conditions at the solar origins of the solar wind. Such plasma conditions which enhance ionization of certain ion charge states relative to others are known to correlate with ICME observations. For the purposes of this study, we seek to test the effectiveness of now-casting ICMEs using heavy ion charge states alone. We selected six charge state parameters for this analysis, each of which have been previously shown to correlate with ICME observations (e.g. *Gruesbeck et al.*, 2011, 2012; *Lepri et al.*, 2001; *Lepri and Zurbuchen*, 2004, 2010; *Zurbuchen and Richardson*, 2006, and references therein). These charge state parameters are the average Fe charge state ($< Q_{\mathrm{Fe}} >$), $\mathrm{Fe}^{16+\,\mathrm{to}\,24+}/\mathrm{Fe}_{\mathrm{tot}}$, $\mathrm{O}^{8+}/\mathrm{O}^{6+}$, $\mathrm{O}^{7+}/\mathrm{O}^{6+}$, $\mathrm{C}^{6+}/\mathrm{C}^{5+}$, and $\mathrm{C}^{6+}/\mathrm{C}^{4+}$.

The data for this study were observed by the Advanced Composition Explorer (ACE) Solar Wind Ion Composition Spectrometer (SWICS) (*Gloeckler et al.*, 1998). ACE was launched in 1997 and has since been taking continuous data in orbit around the L1 point. SWICS measures 77 ion velocity distribution functions, producing density, temperature and thermal velocities for each ion on time resolutions ranging from its native 12 minute scan for more abundant heavy ions (He, C, O), up to 2 hours for less abundant ions (including Si, Mg, Fe). These data sets can be found at the ACE Science Center (http://www.srl.caltech.edu/ACE/ASC/level2/index.html). The densities of individual ions of a given element can be combined to produce charge state distributions, average charge state values, and select ion charge state ratios for selected time resolutions. Additionally, elemental abundance ratios can be produced by summing over ions of a given element.

To explore the utility of solar wind charge state measurements for space weather forecasting, we begin by exploring the observations of heavy element charge states of Fe, O, and C using SWICS two-hour time resolutions. The time period covered in this

study lasts from shortly after science operations began, day 35 of 1998, through day 233 of 2011, after which SWICS mode of operation changed due to a radiation-induced hardware degradation. These dates align with the time span of the Cane and Richardson ICME list (*Cane and Richardson*, 2003; *Richardson and Cane*, 2010), which is available online at http://www.srl.caltech.edu/ACE/ASC/DATA/level3/icmetable2.html.

To now-cast whether a given set of in situ observations at ACE was observing plasma during an ICME, we use a forecast method that tests a range of thresholds for each of the six charge state parameters. Our forecast method utilizes a classification algorithm which scans through every two hour interval of the SWICS charge state data set, from day 35 of 1998 through day 233 of 2011, and classified every charge state parameter observation per time step either as class A, above the charge state parameter threshold, or as class B, below the charge state parameter threshold. This algorithm was applied repeatedly for each parameter stepping through separate threshold values with discrete steps.

The series of discrete threshold values that we test range from $Fe^{16+\,to\,24+}/Fe_{tot} = 0$ to 0.725 with discrete steps of 0.005, $< Q_{Fe} > = 6.5$ to 19.5 with steps of 0.1, $O^{8+}/O^{6+} = 0$ to 0.675 with steps of 0.001, $O^{7+}/O^{6+} = 0$ to 3.4 with steps of 0.01, $C^{6+}/C^{5+} = 0$ to 5.75 with steps of 0.05, and $C^{6+}/C^{4+} = 0$ to 22.5 with steps of 0.25.

For each charge state parameter threshold, a set of forecasting metrics are calculated to evaluate the now-cast accuracy, this is discussed further in Section 2.5. To evaluate the forecast utility of using these charge state parameters to now-cast ICMEs, we measure the accuracy of our now-casts against two published reference ICME lists. The first is created by Cane and Richardson, hereafter referred to as the C&R ICME list (*Cane and Richardson*, 2003; *Richardson and Cane*, 2010). The second is from L. Jian et al., hereafter referred to as the LJ et al. ICME list, (*Jian et al.*, 2011).

We then broke each of the ICME reference lists down into a set of the same two-hour time bins used by our now-cast classification algorithm. Each two hour time bin which contained the listed start time of an ICME or fell between the start and end times of an ICME according to the ICME reference list was labeled as being an ICME time. Each two hour time bin which contained the listed end time of an ICME according to the ICME reference list was labeled as a non-ICME time.

The LJ et al. ICME list spans 1995 - 2009 (*Jian et al.*, 2011), while the version of the C&R ICME list we use for this study spans 1996 - 2011 (*Richardson and Cane*, 2010). It is important to note that the LJ et al. ICME list and the C&R ICME list use different criteria to identify ICMEs in situ. For example, the LJ et al. ICME list was created only using bulk plasma properties and magnetic field signatures to identify the ICME intervals and did not use heavy ion charge state information to create the ICME event list (*Jian et al.*, 2006). The C&R ICME list, however, uses an expanded data set to identify ICMEs, including qualitative assessment of suprathermal electron strahl features and enhancements in heavy ion charge states (*Richardson*, 2004).

Figure 2.2 displays panels of SWICS observations of each of the charge state parameters, $Fe^{16+\,\mathrm{to}\,24+}/Fe_{\mathrm{tot}}$, $< Q_{\mathrm{Fe}} >$, O^{8+}/O^{6+}, O^{7+}/O^{6+}, C^{6+}/C^{5+}, and C^{6+}/C^{4+}. Blue shading marks the ICME times from the C&R ICME reference list, while green shading marks the ICME times from the LJ et al. ICME reference list. These sample plots span across three ICMEs, (though each list only identified two of them,) in one Carrington Rotation from 11/14/2006 to 12/12/2006.

2.5 Comparison of Classification Metrics

Forecast skill scores give a scale for relative accuracy of a set of forecasts with respect to a reference list of observations. Skill scores have long been used in both the weather and space weather forecasting communities. Contingency tables such as Table 2.5, show the relationship between the reference observation list and the

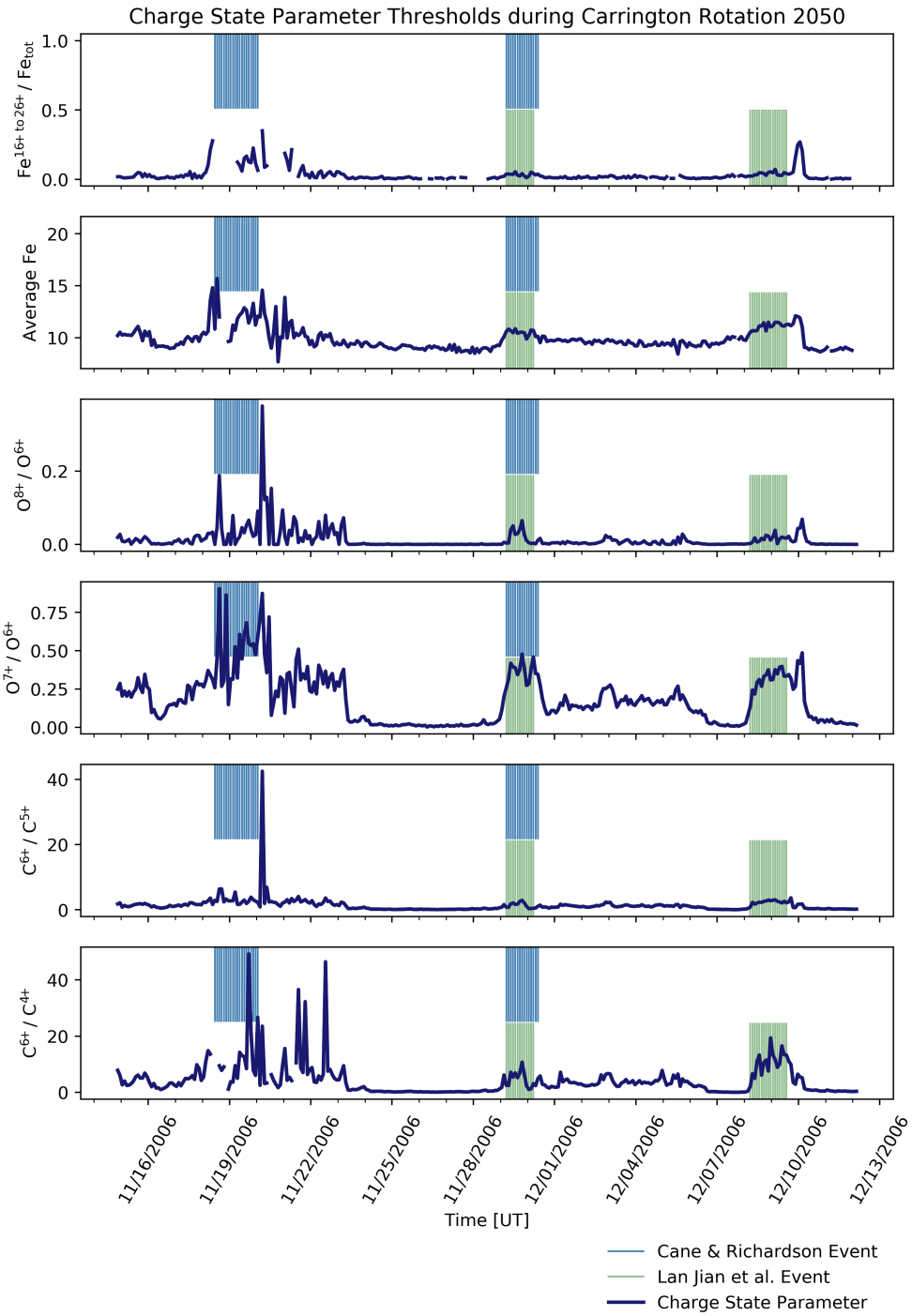

Figure 2.2: Charge state parameter observations spanning Carrington Rotation 2050 from 11/14/2006 to 12/12/2006 as observed by ACE/SWICS. Blue shaded regions correspond to ICME events according to the C&R ICME list (*Richardson and Cane*, 2010). Green shaded regions correspond to ICME events according to the LJ et al. ICME list (2011). This sample of events act as an example of the variability of concurrent charge state parameter observations during ICME observations.

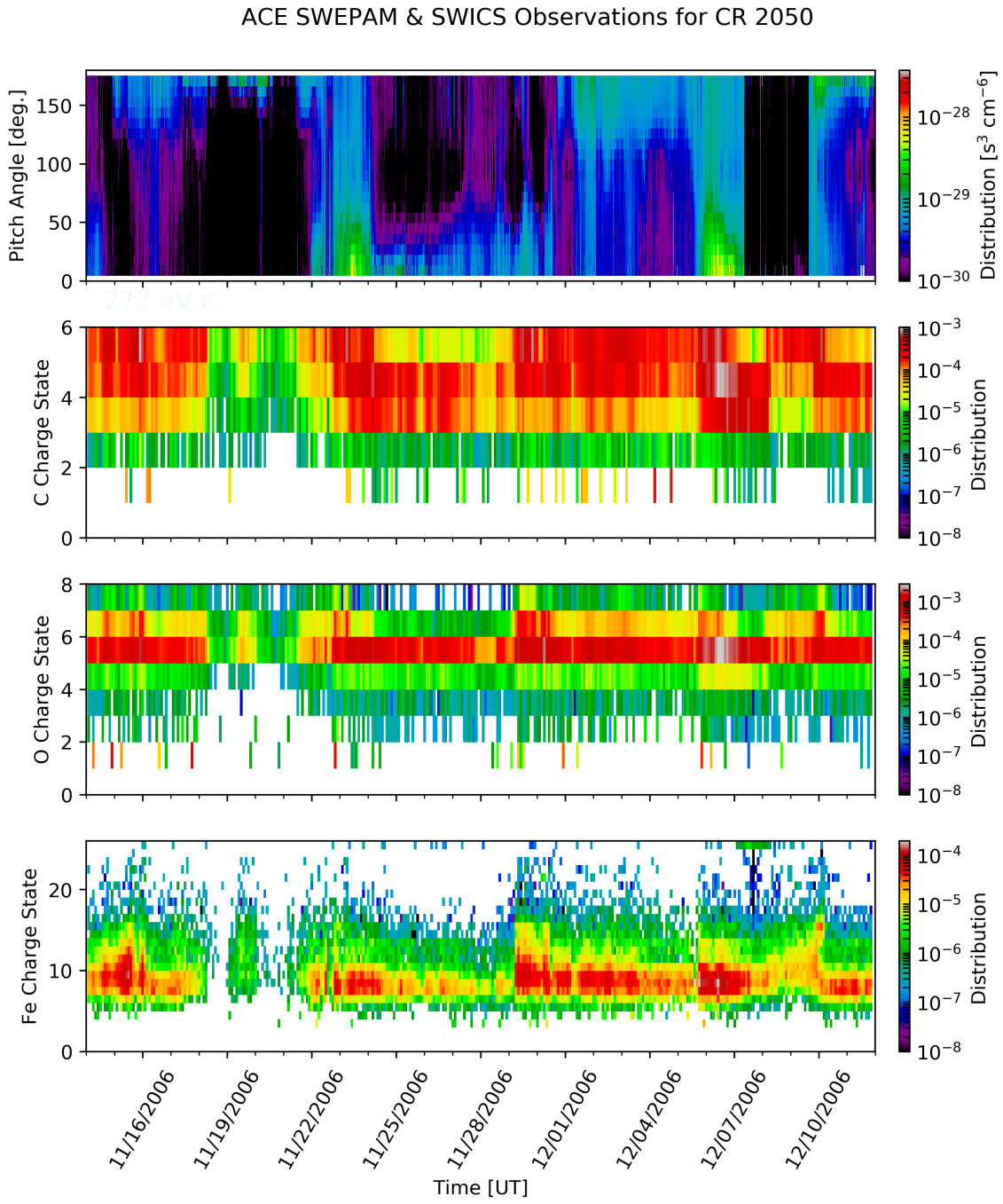

Figure 2.3: Solar wind observations by ACE/SWEPAM and ACE/SWICS spanning Carrington Rotation 2050 from 11/14/2006 to 12/12/2006. The top panel shows the SWEPAM suprathermal electron pitch angle distribution for 272 eV. The 2nd panel presents the SWICS charge state distribution of carbon observations. The third panel has the SWICS charge state distribution of oxygen observations. The fourth panel displays the SWICS distribution of iron observations.

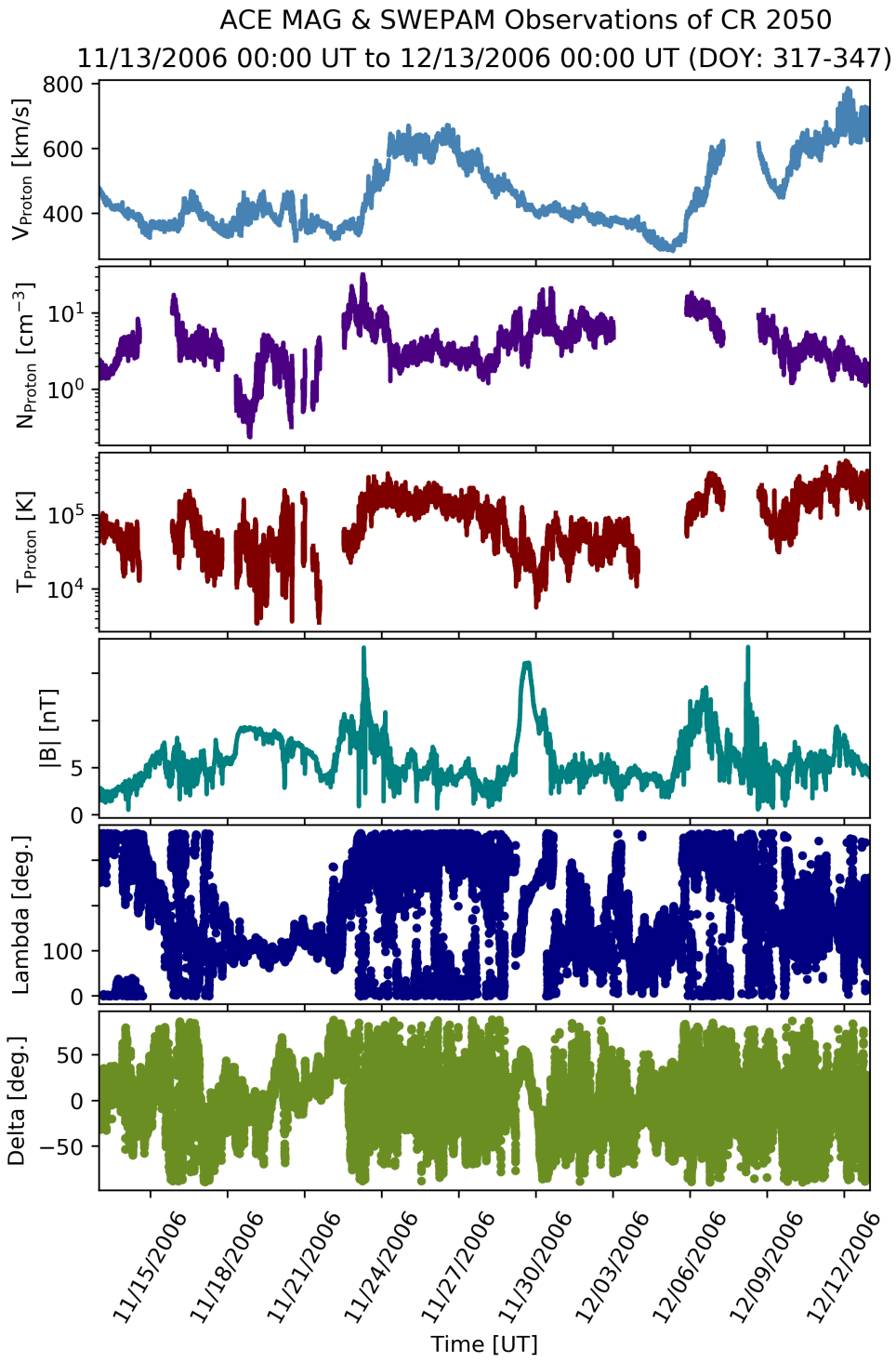

Figure 2.4: Solar wind observations by ACE/MAG and ACE/SWEPAM spanning Carrington Rotation 2050 from 11/14/2006 to 12/12/2006. The upper three panels present proton observations from SWEPAM indicating the bulk solar wind velocity, density and temperature. The lower three panels show magnetic field observations from MAG of the magnetic field magnitude and the lambda and delta magnetic field components.

forecasting method. When the forecasting method correctly classifies an event which was on the reference observation list, then that is a true positive (TP). When the forecasting method classifies something as an event, which was not on the reference list, then that is a false positive (FP). When the forecast method identifies something as not an event and it was not an event according the reference list, then that is a true negative (TN). When the forecasting method classifies something as a non-event, but the reference list includes it as an observed event, then it is a false negative (FN). In the case of this study, a time bin is classified by our forecast method as either part of an ICME or during a non-ICME time. Thus time bins which are part of an ICME are positive events. Our forecast method classifies an observation time bin of SWICS observations of charge state parameters as above or below a threshold value, as discussed in Section 2.4. Our observation reference lists are the C&R ICME list (*Richardson and Cane*, 2010) and the LJ et al. ICME list (*Jian et al.*, 2011), as described in Section 2.4.

	ICME Time According to Reference ICME List	**Non-ICME Time According to Reference ICME List**
Above the Charge State Parameter Threshold	True Positive	False Positive
Below the Charge State Parameter Threshold	False Negative	True Negative

Figure 2.5: Contingency table for charge state parameter threshold now-casting. This table displays the relationship between now-casting using charge state parameter thresholds and observational reference ICME lists. Times which are above the threshold and listed as an ICME time, are identified as true positives (TP). Those times which are above the threshold, but were non-ICME times on the reference list, are classified as false positives (FP). Times which were below the threshold and non-ICME times on the reference list, are classified as true negatives (TN). Times which were below the threshold, but were ICME times according to the reference list, were classified as false negatives (FN).

Table 2.1 defines TP, TN, FP, and FN as described above, as well as several

statistical terms that are referenced throughout this paper. One such term defined in this table, which we will return to later is the true positive rate (TPR), also known as the sensitivity or the probability of detection, which is the percent of TP identifications out of all events as classified by the forecast method, which is the probability of a forecasted event classification to be correct. Likewise, the FP rate (FPR) is the rate of FP identifications out of all non-event times according to the reference list, the TN rate (TNR) is the rate of TN identifications out of all reference list non-events, and the FN rate (FNR) is the rate of FN identifications out of all reference list events. The positive predictive value (PPV), and the false detection rate (FDR) are also defined in Table 2.1. The PPV, which is also known as precision, is the probability that something identified as an event by the forecast method is actually an event on the reference list. The FDR, which is also 1 - PPV, is the probability that something identified as a non-event by the forecast method is actually a non-event according to the reference list.

The Heidke Skill Score (HSS) evaluates the improvement of a forecast as compared to a forecast based on random chance. HSS is a forecast skill score often used in space weather forecasting. The equation we use for HSS in this study is given in Equation 2.1 and defined in Table 2.1.

$$\mathrm{HSS} = \frac{2 \cdot [(\mathrm{TP} \cdot \mathrm{TN}) - (\mathrm{FP} \cdot \mathrm{FN})]}{[(\mathrm{TP} + \mathrm{FP}) \cdot (\mathrm{FP} + \mathrm{FN})] + [(\mathrm{TP} + \mathrm{TN}) \cdot (\mathrm{TN} + \mathrm{FN})]} \tag{2.1}$$

Our forecast method in this study, as described in Section 2.4, tests thresholds for six charge state parameters: $\mathrm{Fe}^{16+\,\mathrm{to}\,24+}/\mathrm{Fe}_{\mathrm{tot}}$, $\mathrm{O}^{8+}/\mathrm{O}^{6+}$, $\mathrm{O}^{7+}/\mathrm{O}^{6+}$, $\mathrm{C}^{6+}/\mathrm{C}^{5+}$, and $\mathrm{C}^{6+}/\mathrm{C}^{4+}$, as well as the average Fe charge state ($< Q_{\mathrm{Fe}} >$). The plot of HSS versus charge state parameter threshold choice across the range our algorithm tested for each of the charge state parameters is given in Figure 2.6. The blue curves give the HSS values when referencing the C&R ICME list, and the green curves mark the HSS values when referencing the LJ et al. ICME list. The maximum HSS is marked with

a gold point. These gold HSS maxima correspond to the HSS optimized threshold values which we subsequently evaluate and discuss in Section 2.6.

The forecast method we use in this study is a classification method. We now-cast an observation as being in either class A, above the threshold (during an ICME), or in class B, below the threshold (during a non-ICME time). When the number of observations within class A is about equivalent to the number of observations within class B, then the class proportions π_A and π_B are each about 1/2 and the data set is class balanced (*Ferri et al.*, 2011). If however, the number of observations in each class is vastly different and $\pi_A \gg \pi_B$ or $\pi_A \gg \pi_B$, then the data set is highly class imbalanced. In this case, the class proportion of the ICME class (class A) using the C&R list is $\pi_A = 0.078$ and when using the LJ et al. list $\pi_A = 0.067$. For a two class forecast method, the sum of the two class proportions is 1. The class which is much greater in size, is defined as the major class, which in this case is the class of non-ICME solar wind observations (class B) for both reference lists. Thus, it becomes quite clear that when classifying space weather events such as ICMEs in the solar wind, the classes are highly imbalanced.

The HSS, defined in Equation 2.1 and in Table 2.1, assumes the cost of falsely identifying an event as a non-event is equivalent to the cost of falsely identifying a non-event as an event (*Provost and Fawcett*, 2001). When the classes are balanced and when you value true positives and true negatives equivalently for your forecasting purposes, the costs might be equal. For the data sets considered in this study, however, and for many other data sets in the space weather community when solar wind observations comprise the non-event class, the classes are so extremely imbalanced one cannot assume the cost functions of each class are equivalent.

Because HSS assumes equal cost functions, when using a data set that is highly class imbalanced, the threshold choice that is optimized for the highest HSS ends up heavily weighting the major class over the minor (*Haixiang et al.*, 2017). In this case,

this means HSS will value FPs and FNs equally, however, since the percentage of the data set which are non-events is so high, then HSS will optimize for reducing error in the major class, or in this case, reducing the FPR, at the expense of missing actual ICME events, resulting in a low TPR.

Hence, though skill scores such as HSS are commonly used for evaluating forecasting models in space weather, as adapted from the weather forecasting community, depending on one's specific forecasting needs and the class balance of the data set, HSS is likely not the best metric to use. Therefore, for space weather forecasting using highly class imbalanced data, one should turn to a classification metric which is less skewed by extreme class proportions. Classification metrics based in receiver operating characteristic (ROC) space are metrics which are not automatically skewed by extreme class imbalance and allow one to consider the costs of misidentifying events (*Ferri et al.*, 2011).

Receiver operating characteristic (ROC) curves plot TPR versus FPR, where every point along the curve gives the TPR and FPR of a different threshold choice. Following the curve, the highest threshold choices fall where TPR and FPR are close to zero, or the lower-left corner, and the lowest threshold choices are where TPR and FPR are near one, or the upper-right corner in ROC space. The stronger the predictive strength of the selected charge state parameter, the closer the curve will bend towards the upper-left corner in ROC space, where TPR = 1 and FPR = 0. Therefore, it is promising that the ROC curves of these charge state parameters, $Fe^{16+\,\mathrm{to}\,24+}/Fe_{tot}$ and O^{7+}/O^{6+}, do clearly bend towards that upper-left corner, as seen in Figures 2.7 and 2.8, respectively. The ROC curves for these charge state parameters are clearly stronger than either a straight unity line, (where TPR = FPR,) which would indicate no clear threshold choice, or a curve that bends to the lower-right corner, (where TPR = 0 and FPR = 1,) which would indicate that the parameter was anti-correlated with ICME events.

For each of the charge state parameters of this study, the ROC curves show such a clean curve that bends towards the upper-left corner. Additional ROC curves for the other four charge state parameters can be found as Supplemental Figures. These ROC curves indicate that these parameters do have predictive value and an optimal threshold choice can be found that maximizes for positive likelihood ratio (PLR). The PLR is the ratio between TPR and FPR, in particular the PLR is $\frac{\text{TPR}}{\text{FPR}}$. The Youden's J statistic is a statistic that is a maximum in the upper-left corner of ROC space, when PLR is a maximum. The definition of the J statistic is given in Table 2.1. The purple points in the ROC curves in Figures 2.7 and 2.8 mark the J statistic maxima where PLR is maximized. The threshold values for each of the charge state parameters which optimize for these J statistic maxima are the thresholds which we subsequently evaluate and discuss in Section 2.6 as the ROC optimized charge state parameter thresholds.

The thresholds in ROC space that correspond to the J statistic maxima, optimize for maximum TPR and maximum TNR equally. The benefit of ROC space is that one can see the trade-off benefits between TPR and FPR and consider other costs. Perhaps one wishes to minimize the FPR at the cost of having a lower TPR, because the cost of misidentifying a non-ICME time as an ICME is considered greater than the cost of missing ICME times because the threshold is low, then one might choose a point along the curve left of the J statistic maximum. For example, to minimize FPR, if one slides left along the curve towards lower FPR values, one could choose a threshold that corresponds to maximum PPV which optimizes for TPR with respect to FPR while ignoring the TNR and FNR. The blue and grey points in the $Fe^{16+\,\text{to}\,24+}/Fe_{\text{tot}}$ and O^{7+}/O^{6+} ROC curves in Figures 2.7 and 2.8, mark the threshold choices which maximize for PPV with respect to the C&R ICME list and the LJ et al. ICME list, respectively. These thresholds corresponding to maximum PPV values are evaluated and discussed in Section 2.6 as the PPV optimized charge state

parameter thresholds.

Figure 2.9 displays the values for each of the six charge state parameters examined in this study over the course of Carrington Rotation 2050, from 11/14/2006 to 12/12/2006. The ACE/SWICS observed charge state data is plotted over the shaded regions that were identified as ICME events by the C&R ICME reference list (light blue) and by the LJ et al. ICME list (green). The optimal threshold levels found by the Heidke Skill Score method shown in Section 5.2.2.3 are shown with horizontal yellow lines. Similarly, the optimal threshold levels found by optimizing for Youden's J statistic in ROC space, as defined in Table 2.1 and explained in Section 2.4, are marked with horizontal purple lines. Carrington Rotation 2050 is a sample time period with three identified ICME events that were observed by ACE. The first and second of which were classified as ICMEs by the C&R ICME database, whereas the second and third events were classified as ICMEs by the LJ et al. ICME list.

One can note in Figure 2.9 that for each of the six charge state parameters, the observed values exceed the ROC threshold for all three of the events, whereas the HSS threshold only caught the first event for all parameters. These sample events demonstrate some of the complexity involved in using a single threshold to identify ICME events. Take note of the O^{7+}/O^{6+} subplot. The HSS threshold value for this parameter selects boundaries for the first event that effectively match the C&R ICME list, whereas the ROC boundaries select the trailing section of elevated charge states that were not chosen to be part of the C&R ICME list. In contrast, the boundaries of the second event were identified well using the O^{7+}/O^{6+} ROC threshold, and effectively match both reference lists, whereas the O^{7+}/O^{6+} HSS threshold misses the event entirely. The top panel also demonstrates what obscures some of the results. Some of the $Fe^{16+\,\mathrm{to}\,24+}/Fe_{\mathrm{tot}}$ data was missing during the first event and as such, some of the event time periods had to be rejected, this is discussed further in Section 2.6.

Term	Abbrev.	Equation	Statistical Definition	Study Definition
True Positives	TP	Sum of all true positive time bins.	Time bins that the forecast method correctly identifies as occurring during event times.	Charge state parameter values at or above the threshold during an ICME time according to the ICME reference list.
True Negatives	TN	Sum of all true negative time bins.	Time bins that the forecast method correctly identifies as occurring non-event times.	Charge state parameter values below the threshold during a non-ICME time according to the ICME reference list.
False Positives	FP	Sum of all false positive time bins.	Time bins that the forecast method incorrectly identifies as occurring event times.	Charge state parameter values at or above the threshold during a non-ICME time according to the ICME reference list.
False Negatives	FN	Sum of all false negative time bins.	Time bins that the forecast method incorrectly identifies as occurring during non-event times.	Charge state parameter values below the threshold during an ICME time according to the ICME reference list.
Heidke Skill Score	HSS	$\frac{2\,[(TP \cdot TN) - (FP \cdot FN)]}{(TP+FP)\cdot(FP+FN) + (TP+TN)\cdot(TN+FN)}$	Forecast skill score that gives the relative accuracy of a forecast method with respect to a reference list of observations relative to random chance.	A forecast skill score that quantifies the accuracy of classifying ICME or non-ICME event observations using a charge state parameter threshold as opposed to random chance with respect to a reference list of ICMEs.
Class Proportion	π_A or π_B	$\pi_A = n_A / n$ or $\pi_B = n_B / n$	Number of time bins in a class (n_B or n_A) out of the total number of time bins (n).	The class proportion for the class of ICMEs (π_A) is the number of ICME times (n_A) out of the total number of time bins (n).
True Positive Rate or Sensitivity or Probability of Detection	TPR	TP / (TP + FN) ·100	The probability that an event is correctly identified as an event.	Percent of the reference list ICME times at or above the threshold.
True Negative Rate or Specificity	TNR	TN / (TN + FP) ·100	The probability that a non-event is correctly identified as a non-event.	Percent of the reference list non-ICME times below the threshold.
False Positive Rate	FPR	FP / (FP + TN) ·100	The probability that a non-event is incorrectly identified as an event.	Percent of the reference list non-ICME times at or above the threshold.
Positive Predictive Value or Precision	PPV	TP / (TP + FP) ·100 or TPR / (TPR+FPR) ·100	The probability that times identified as events by the test are actually event times.	Percent of the charge state parameter values at or above the threshold identified by both charge state parameter threshold and ICME reference list.
False Discovery Rate	FDR	FP / (FP + TP) ·100 or 1 - PPV	The probability that times identified as events by the test are actually non-events.	Percent of the charge state parameter values at or above the threshold that are non-ICME times according to the ICME reference list.
Receiver Operating Characteristic Space	ROC space	TPR vs FPR space	Graphically represents the relationship between TPR and FPR.	Graphically demonstrates the trade-off between the probability of correctly identifying ICME times and the probability of falsely identifying solar wind as an ICME time.
Youden's J Statistic	J	TPR + TNR - 1 or sensitivity + specificity - 1	J is a maximum at the TPR = 1 & FPR = 0 corner of ROC space.	The metric used to identify how well a threshold maximizes the probability of correct identification of both ICME times and solar wind times.

Table 2.1: Definitions of statistical terms used throughout this study. Col. 1: Unabbreviated terms. Col. 2: Abbreviations. Col. 3: Statistical equations. Col. 4: General statistical definitions. Col. 5: Definitions as they pertain to this study.

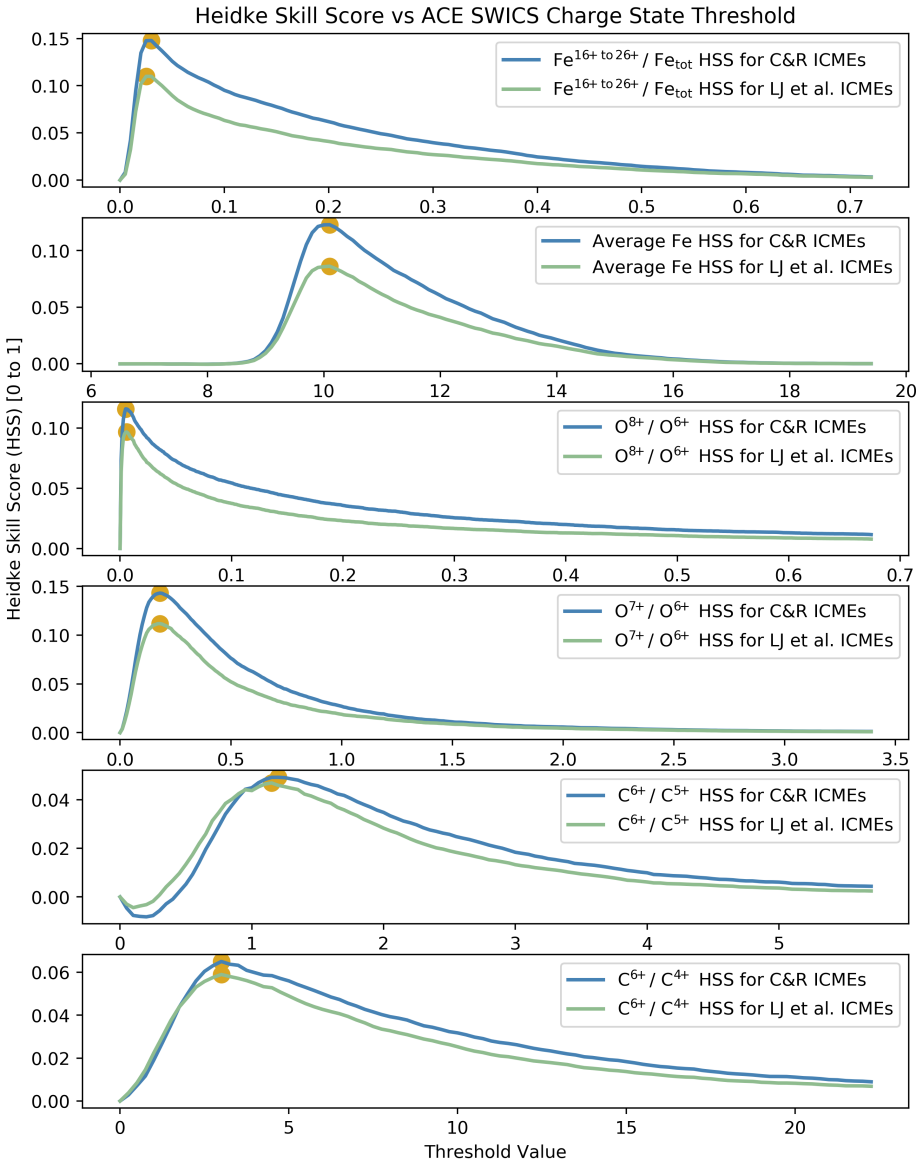

Figure 2.6: Plots give the Heidke skill score (HSS) as a function of threshold value. Each panel shows the results for each charge state parameter. In order from top to bottom: $Fe^{16+\,to\,24+}/Fe_{tot}$, the average Fe charge state $< Q_{Fe} >$, O^{8+}/O^{6+}, O^{7+}/O^{6+}, C^{6+}/C^{5+}, and C^{6+}/C^{4+}. This HSS is a statistical forecast skill score that evaluates the accuracy of charge state parameter ICME now-casts with respect to an ICME reference list. The closer the HSS value is to unity, the better the threshold choice can reproduce the published ICME list. Two published ICME databases are used for this comparison. Blue results are based on the ICME boundaries given in the C&R ICME list (*Richardson and Cane*, 2010). Green results are based on ICME boundaries from the LJ et al. ICME list (*Jian et al.*, 2011). Golden points show the maximum HSS threshold used to determine the results presented in Section 2.6.

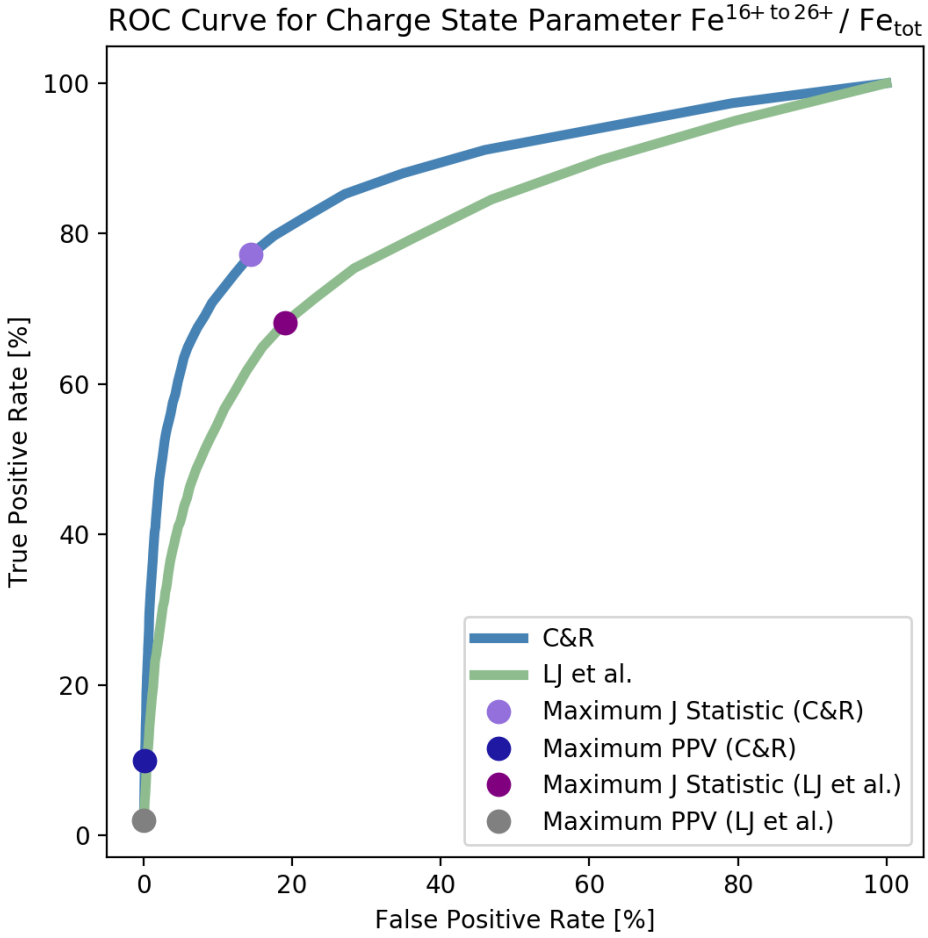

Figure 2.7: This Receiver Operating Characteristic (ROC) curve gives the ratio of true positive detection to false detection for the charge state parameter $Fe^{16+\,to\,24+}/Fe_{tot}$. Blue results are based on the interplanetary coronal mass ejection boundaries given in the C&R list (*Richardson and Cane*, 2010). Green results are based on ICME boundaries from the LJ et al. list (*Jian et al.*, 2011).

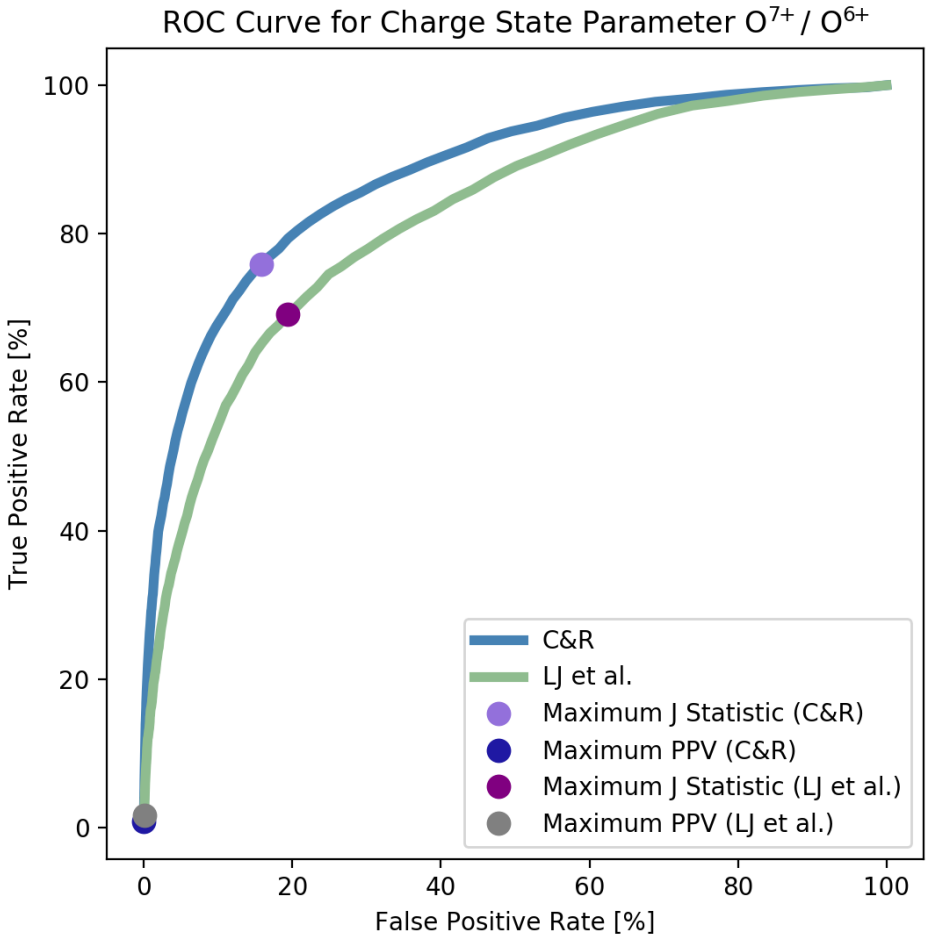

Figure 2.8: This Receiver Operating Characteristic (ROC) curve gives the ratio of true positive detection to false detection for the charge state parameter O^{7+}/O^{6+}. Blue results are based on the interplanetary coronal mass ejection boundaries given in the C&R ICME list (*Richardson and Cane*, 2010). Green results are based on ICME boundaries from the LJ et al. ICME list (*Jian et al.*, 2011).

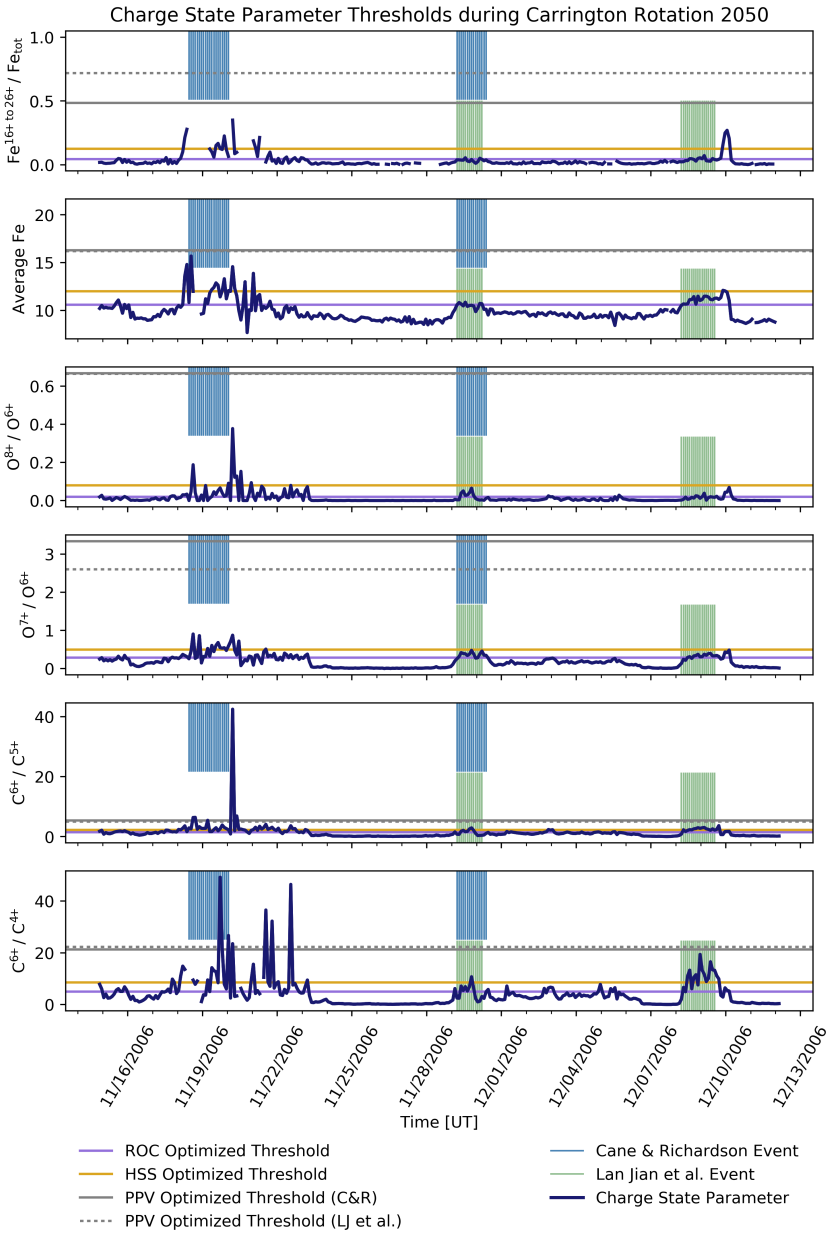

Figure 2.9: Plots of each of the six charge state parameters examined in this study over the course of Carrington Rotation 2050, from 11/14/2006 to 12/12/2006. The navy data points are the observed ACE/SWICS charge state parameter values. Shaded regions mark the time spans which were identified as ICME events by the C&R reference list (blue) and by the LJ et al. reference list (green). The HSS optimized threshold levels are marked with horizontal yellow lines and the ROC optimized threshold levels are marked with horizontal purple lines.

2.6 Results of Event Identification Optimization

The final analysis and results for each charge state parameter across the full study are shown in Table 2.2. The top section of Table 2.2 lists the results when optimizing the threshold choices for maximum HSS, while the center section optimizes for maximum J statistic, as defined in Table 2.1, which is the upper left corner in ROC space, the lower section of Table 2.2 shows results for thresholds optimized for maximizing positive predictive value (PPV). These are the results for the full study period from 1998 through 2011 using the Cane and Richardson ICME list as reference (*Richardson and Cane*, 2010) and across 1998 through 2009 when using the Jian et al. ICME list as reference (*Jian et al.*, 2011).

The strongest choice of charge state parameters were $Fe^{16+\,\mathrm{to}\,24+}/Fe_{\mathrm{tot}}$ and O^{7+}/O^{6+}, when selecting for greatest TPR, as defined in Table 2.1 as the percentage of ICME times where the charge state parameter was at or above the threshold or for lowest FPR, as defined in Table 2.1 as the percentage of non-ICME times where the charge state parameter was at or above the threshold.

There is a smooth trade-off between increasing the TPR and reducing the FPR for any given threshold and any given charge state parameter. This smooth trade-off can be seen in the detection rate plots, Figures 2.10 and 2.11, and in the ROC curves in Figures 2.7 and 2.8. Even while there is a clear and strong correlation between the threshold choice and the TPR, there is no magical threshold choice which optimizes well for TPR without likewise yielding on the FPR. Each of the three optimized threshold choices results from a different choice along that trade-off curve. For example, as can be seen in Table 2.2, the threshold with the lowest FPR was that which optimized for Positive Predictive Value (PPV), as defined in Table 2.1, the percentage of times with charge state parameters at or above the threshold, which were also identified by the ICME catalog as ICMEs, or the percentage of the positives which were true positives. This PPV optimized threshold resulted in an

FPR of less than 0.1% across all the charge state parameters for the C&R ICME catalog.

The PPV optimized threshold is so selective that while it fails to find the majority of the ICME times, when using this threshold one can have a strong confidence in its correct identification of ICME times. When a time is identified by this threshold as an ICME, one can be 99.9% sure that it is indeed inside of an ICME, because the FPR is less than 0.1% for each charge state parameter as shown in Table 1. The fact that a threshold exists at which ICMEs can be identified so confidently suggests strong proof that portions of ICME plasma have rates of ionization which are not observed in solar wind times outside of ICMEs.

The results of these statistical analyses show that each individual threshold has limitations, and that considering a combination of these thresholds will give the best results. If one is looking at real-time observations of solar wind heavy ion observations and for example the $Fe^{16+\,to\,24+}/Fe_{tot}$ charge state parameter rises above the HSS optimized threshold, one can have some confidence that this might be an ICME, once the observed charge states rise above the J statistic optimized threshold, one can be even more confident that this is an ICME, once the PPV optimized threshold is surpassed, one can be nearly certain that this is an ICME. At which point along this analysis one takes action may depend on the use and risks involved. Someone concerned with space weather forecasting for operational needs, whose mitigation costs are far lower than the costs of missing a major event might choose to use one of the HSS threshold values to now-cast. In contrast, if one values getting the ICME identification right about as equivalently as they hope to reduce their misidentification of ICME times, then perhaps the ROC space optimized thresholds are more appropriate. In contrast, for ICME study, if one wishes to create a list of ICME times which are more assuredly within ICME plasma, then the PPV optimized threshold would be the best choice.

Trailing ionized plasma following the ICME times of the ICME lists are frequently

found to be above the threshold and are considered false positives in this statistical analysis. This is often due to a drop in density or the end of the magnetic flux rope as observed in the solar wind observations. These are observational signatures considered by both C&R and Jian et al. when creating their ICME lists. This can be seen particularly well for example, during the first ICME event in Figure 2.9 when compared to the solar wind observations shown in Figures 2.3 and 2.4. These discrepancies lead into a discussion of the definition of an ICME. Is the trailing ionized plasma that has fallen behind a magnetic flux rope still part of an ICME? We suggest that these times of enhanced heavy ions should still be considered part of the ICME and while they appear as false positives in this analysis, we will be undergoing continued research to consider these and additional instances where false positives and false negatives are due to similar non-uniformity of ICME structure as opposed to poor ICME identification.

Across all six charge state parameter threshold choices, the thresholds optimized for maximum Heidke Skill Scores were significantly lower than the other thresholds. This was unsurprising given that the HSS is more heavily impacted by the significant class imbalance in number of ICME times versus non-ICME times than other optimization values, including the J statistic and the PPV. A full explanation of the impact of class imbalance on this study can be found in Section 2.4.

2.7 Conclusions

We conducted an assessment of how well heavy ion charge state parameters can identify ICME intervals, as originally identified in two published studies. Our main findings are as follows:

1. **The charge state parameter with the strongest positive predictive value (PPV) is $Fe^{16+\,to\,24+}/Fe_{tot}$, followed by O^{7+}/O^{6+}, across all sta-**

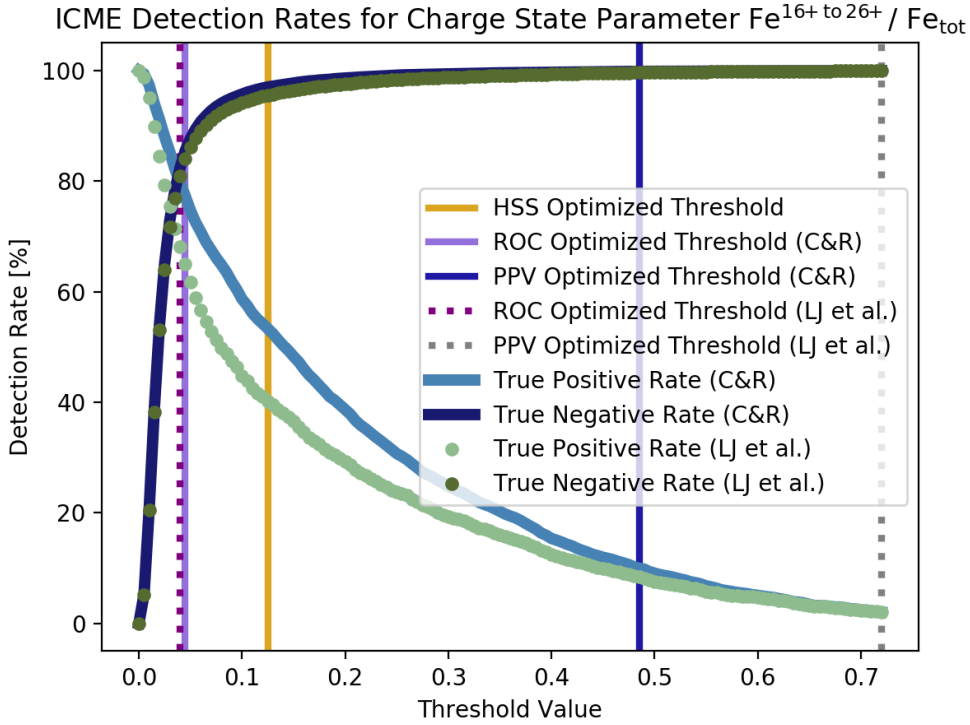

Figure 2.10: This figure shows how the detection rate of $Fe^{16+\,to\,24+}/Fe_{tot}$ varies with threshold choice. Vertical lines represent threshold choices that optimize for HSS and ROC. Solid lined results are based on the ICME boundaries from the C&R ICME list (*Richardson and Cane*, 2010). Dotted results are based on the ICME boundaries from the LJ et al. ICME list (*Jian et al.*, 2011). Navy results are based on the set of all non-event times binned by 2 hour intervals. Green results are based on the set of all ICME event times binned in 2 hour intervals.

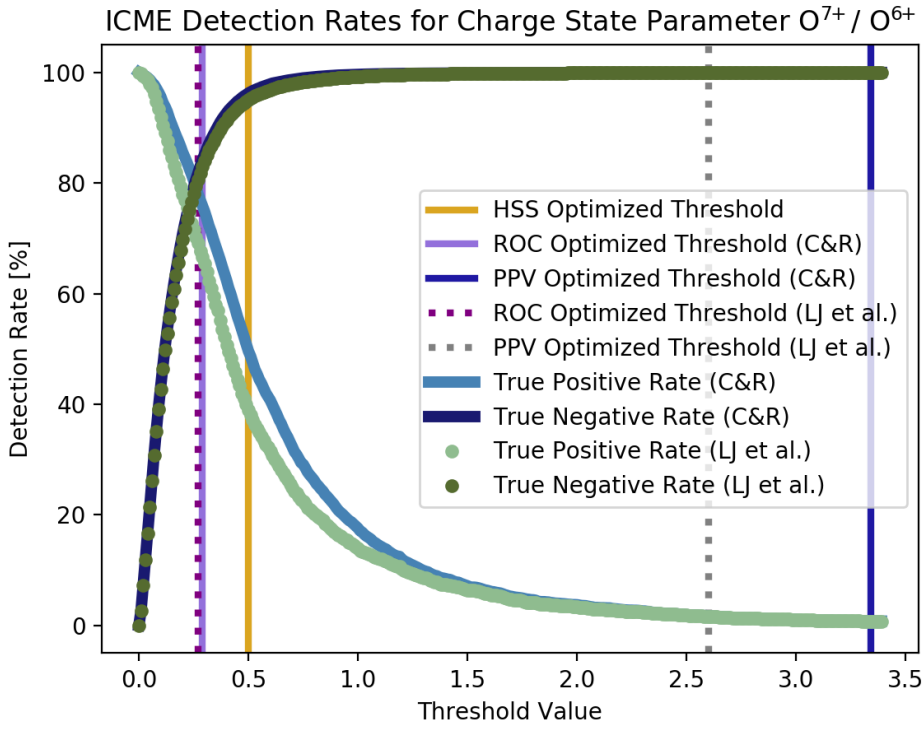

Figure 2.11: This figure shows how the detection rate of O^{7+}/O^{6+} varies with threshold choice. Vertical lines represent threshold choices that optimize for HSS and ROC. Solid lined results are based on the ICME boundaries from the C&R ICME list (*Richardson and Cane*, 2010). Dotted results are based on the ICME boundaries from the LJ et al. ICME list (*Jian et al.*, 2011). Navy results are based on the set of all non-event times binned by 2 hour intervals. Green results are based on the set of all ICME event times binned in 2 hour intervals.

Heidke Skill Score (HSS) Optimized Threshold Results

Charge State Parameter Threshold	TPR (C&R)	FPR (C&R)	PPV (C&R)	FDR (C&R)	TPR (LJ et al.)	FPR (LJ et al.)	PPV (LJ et al.)	FDR (LJ et al.)
$Fe^{16+\,to\,26+}$ / Fe_{tot} ≥ 0.125 (C&R), ≥ 0.125 (LJ)	53%	3%	61%	39%	40%	4%	42%	58%
Average Fe ≥ 12 (C&R), ≥ 12 (LJ)	40%	1%	70%	30%	31%	2%	49%	51%
O^{8+} / O^{6+} ≥ 0.08 (C&R), ≥ 0.08 (LJ)	40%	4%	44%	56%	33%	5%	32%	68%
O^{7+} / O^{6+} ≥ 0.5 (C&R), ≥ 0.5 (LJ)	50%	4%	53%	47%	39%	5%	37%	63%
C^{6+} / C^{5+} ≥ 2.25 (C&R), ≥ 2.25 (LJ)	22%	4%	31%	69%	19%	4%	25%	75%
C^{6+} / C^{4+} ≥ 8.5 (C&R), ≥ 8.5 (LJ)	27%	5%	30%	70%	25%	6%	26%	74%

Receiver Operating Characteristic (ROC) Optimized Threshold Results

Charge State Parameter Threshold	TPR (C&R)	FPR (C&R)	PPV (C&R)	FDR (C&R)	TPR (LJ et al.)	FPR (LJ et al.)	PPV (LJ et al.)	FDR (LJ et al.)
$Fe^{16+\,to\,26+}$ / Fe_{tot} ≥ 0.045 (C&R), ≥ 0.04 (LJ)	77%	14%	32%	68%	68%	19%	22%	78%
Average Fe ≥ 10.6 (C&R), ≥ 10.5 (LJ)	67%	13%	30%	70%	58%	17%	20%	80%
O^{8+} / O^{6+} ≥ 0.019 (C&R), ≥ 0.012 (LJ)	64%	18%	23%	77%	67%	26%	16%	84%
O^{7+} / O^{6+} ≥ 0.29 (C&R), ≥ 0.27 (LJ)	76%	16%	29%	71%	69%	19%	21%	79%
C^{6+} / C^{5+} ≥ 1.5 (C&R), ≥ 1.35 (LJ)	38%	15%	17%	83%	42%	20%	14%	86%
C^{6+} / C^{4+} ≥ 5 (C&R), ≥ 4.5 (LJ)	44%	17%	18%	82%	47%	21%	15%	85%

Positive Predictive Value (PPV) Optimized Threshold Results

Charge State Parameter Threshold	TPR (C&R)	FPR (C&R)	PPV (C&R)	FDR (C&R)	TPR (LJ et al.)	FPR (LJ et al.)	PPV (LJ et al.)	FDR (LJ et al.)
$Fe^{16+\,to\,26+}$ / Fe_{tot} ≥ 0.485 (C&R), ≥ 0.72 (LJ)	10%	0%	84%	16%	2%	0%	71%	29%
Average Fe ≥ 16.3 (C&R), ≥ 16.2 (LJ)	2%	0%	82%	18%	2%	0%	70%	30%
O^{8+} / O^{6+} ≥ 0.667 (C&R), ≥ 0.664 (LJ)	8%	0%	70%	30%	6%	0%	49%	51%
O^{7+} / O^{6+} ≥ 3.34 (C&R), ≥ 2.6 (LJ)	1%	0%	92%	8%	2%	0%	77%	23%
C^{6+} / C^{5+} ≥ 5.4 (C&R), ≥ 5 (LJ)	3%	0%	67%	33%	3%	0%	41%	59%
C^{6+} / C^{4+} ≥ 21.25 (C&R), ≥ 22.25 (LJ)	7%	0%	53%	47%	5%	1%	42%	58%

Table 2.2: Table of statistical results for three of the threshold tests: the HSS optimized thresholds, the ROC optimized thresholds and the PPV optimized thresholds. Each row in each subtable displays the statistical results for each charge state parameter threshold. The first column lists the threshold values tested for each parameter. Statistical rates of TPR, FPR, PPV and FDR are given as percentages in each subtable column, first with respect to the C&R ICME reference list, second with respect to the LJ et al. ICME reference list.

tistical metrics.

These two charge state parameters have the strongest correlation with ICME occurrence and are the strongest parameter choices for ICME event identification.

2. **The resulting lists of ICME events based on charge state parameters have stronger statistical agreement with the C&R ICME catalog, than the LJ et al. ICME catalog.**

   For each of the charge state parameters considered, the resulting true positive rates (TPRs) and positive predictive values (PPVs) are higher when compared to the C&R ICME catalog than the LJ et al. ICME catalog. This is consistent with expectations: the C&R ICME catalog considered heavy ion charge states, whereas LJ et al. did not. That said, the LJ et al. ICME catalog still decently correlated with times identified by the $Fe^{16+\,to\,24+}/Fe_{tot}$, and O^{7+}/O^{6+} parameters.

3. **HSS optimized thresholds have stronger positive predictive values (PPVs), and result in ICME now-casts with significantly lower false positive rates (FPRs) at the cost of reduced true positive rates (TPRs).**

   FPRs for the PPV optimized threshold range from 1% to 5% when compared to the C&R ICME catalog, and from 2% to 6% when compared to the LJ et al. ICME catalog. Whereas, TPR for the PPV optimized threshold range from only 22% to 53% when compared to the C&R ICME catalog, and from only 19% to 40% when compared to the LJ et al. ICME catalog. This weighting towards reduced false positives at the cost of true positives is primarily due to HSS sensitivity to the class imbalance of this data set due to the vastly different population sizes of ICME times compared with non-ICME solar wind times.

4. **The six charge state parameters considered here do not demonstrate a single obvious threshold choice.**

   The spectrum of threshold choices yield a steady trade-off between TPR and FPR with no single optimal threshold. As demonstrated by the smooth curves in ROC space of Figures 2.7 and 2.8, when one increases the charge state parameter threshold to capture all of the event times as true positives, there is an equally steady increase in false positive events identified.

5. **While PPV optimized thresholds identify only a small fraction of the ICME times in the ICME reference lists, they have FPRs of less than 0.1% for all charge state parameters when compared to the C&R ICME catalog.**

   Thus, the PPV optimized threshold choices do not produce ICME lists that have a complete set of ICME times, rather these lists contain times that are contained in the C&R ICME catalog and one can be confident are actually ICME times. That is, while they miss many of the events, you know that the events it detects are almost certainly ICMEs.

6. **Considering multiple charge state parameter thresholds can increase confidence in event identification.**

   When a time exceeds more than one charge state parameter threshold, there is a higher likelihood that the time is identified as an ICME in one of the ICME catalogs, as opposed to if it exceeds only one charge state parameter individually: for example, if a charge state parameter value exceeds both the PPV optimized threshold and the ROC optimized threshold, one can have greater confidence that this occurs in an ICME, than if it only exceeded the ROC optimized threshold. For future work, the authors intend to investigate the value

in considering a charge state parameter threshold which is an ensemble of both $Fe^{16+\,to\,24+}/Fe_{tot}$ and O^{7+}/O^{6+} for example.

7. **The ICME lists resulting from each charge state parameter threshold are worth further study.**

   False positives in this study, for example, contain times of enhanced charge state parameters either at the boundaries of ICMEs or during smaller transient events that may have been discounted by the ICME catalogs for reasons such as low proton density or a lack of a clear flux-rope magnetic field structure. Moreover, these false positive times do vary between ICME catalogs. Therefore, whether these times are "false" depends on the actual definition of what is required to be defined as an ICME. Further analysis of these heavy ion observations identified as false positives might lead to insights for determining what size of ICME, and what type of magnetic field structure should be required to be categorized as an ICME.

8. **Further investigation into the utility of heavy ion charge states for ICME now-casting using machine learning classification algorithms could be the next steps to continue this study.**

   As described in Section 2.4 and defined in Section 2.5, the forecast method used in this study is a classification algorithm. For this study we separately consider each charge state parameter threshold as a boundary between two classes, above the threshold or below. Future applications of this research will address a multitude of classes, where some classes are an ensemble of those considered here, such as a class which is defined with charge state parameters above both the $Fe^{16+\,to\,24+}/Fe_{tot}$, and O^{7+}/O^{6+} thresholds. Using a combination of the six charge state parameters to produce ensemble classes, which are not

mutually exclusive, one winds up with hundreds of possible classes. To test each individual ensemble threshold as a forecast method individually or to consider multiple classes which are not mutually exclusive, using the methods of this paper would be too computationally expensive. Thus, the authors seek to continue the study of these charge state parameters for ICME now-casting using machine learning classification algorithms. This study was essentially a baby machine learning classification algorithm which considered only two classes and used the C&R and LJ et al. ICME reference lists as training sets. Classification algorithms have been designed to handle much larger numbers of classes and the authors intend to use the results of this study as a guide to train a machine learning algorithm to investigate the value of a range of ensemble thresholds as forecast methods which might be more effective at ICME now-casting than a single charge state parameter alone.

CHAPTER III

Characterizing Magnetic Connectivity of Solar Flare Electron Sources to STEREO Spacecraft Using ADAPT-WSA Modeling

3.1 Preface

This study uses a combination of in situ observations of six SEP events which were observed by two or more satellites and solar wind modeling, to trace from 1 AU observations back to the solar origins of the SEP events and compare those origins to the Parker Spiral predicted magnetic connectivity. This study evaluates how well the Parker Spiral approximates the magnetic connectivity compared to ADAPT-WSA modeling using in situ observations of several case SEP events at multiple spatially separated observation points 1 AU from the Sun.

3.2 Abstract

From late 2013 through 2014 the STEREO A and B spacecraft were separated by $< 70^{\circ}$ in longitude, optimally located for simultaneous observations of impulsive energetic ($E > 30$ keV) electron events from solar flares. Temporal profiles of the electrons in common events at the two spacecraft can be compared to determine times

of injections and propagation characteristics along the different magnetic field-line paths connecting the spacecraft to the flare sources. Observations with the STEREO Solar Electron and Proton Telescope of several energetic electron events from known flare sources were analyzed by Klassen et al. to determine injection profiles and propagation along non-radial magnetic fields from the active regions (2015; 2016; 2018). Their analysis depended on a determination of magnetic field line connections using the Parker spiral field approximation. We have run multiple realizations of the ADAPT-WSA (Air Force Data Assimilative Photospheric flux Transport - Wang-Sheeley-Arge) solar wind forecast model to compare the model solar magnetic field connections at STEREO with those derived from the Parker approximation for the reported electron events. The advantages of the ADAPT-WSA model for establishing magnetic field line connections will be discussed.

3.3 Introduction

Characterizing the acceleration processes and solar source locations of solar energetic particle (SEP) events observed at 1 AU remains a challenging goal of SEP studies. The arrival-time profiles of higher-energy particles are generally more useful for inferring their solar injection profiles than those of the lower-energy particles, which are more dependent on interplanetary transport processes. In particular, near-relativistic electrons are an abundant SEP species that allow for detailed studies of their solar injection conditions (*Kahler*, 2007). Haggerty and Roelof (2009) showed that the class of spike events, defined as having nearly symmetric rise-and-fall intensity profiles, were associated with explosive events in the low corona. Their other classes were the pulse events, with fast rises but slower decays, and ramp events, which have gradual rises to plateaus.

Instruments on the STEREO A and STEREO B spacecraft have allowed studies of electron events in the 30 to 400 keV range with the Solar Electron and Proton

Telescope (SEPT) (*Müller-Mellin et al.*, 2008), their accompanying solar extreme ultraviolet (EUV) images with the Sun Earth Connection Coronal and Heliospheric Investigation (SECCHI) Extreme Ultraviolet Imager (EUVI) (*Howard et al.*, 2008), and radio emission spectra with the STEREO WAVES (SWAVES) instrument (*Bougeret et al.*, 2008). Early complementary observations of individual or sequences of electron events were done with only the STEREO A spacecraft (*Klassen et al.*, 2011, 2012). Those results indicated electron injections at the same times and locations as small active region (AR) EUV jets and type III radio bursts, confirming previous results (*Nitta et al.*, 2006). Dresing et al. (2014) statistically surveyed the peak intensities, onset delays, and anisotropies of 21 electron events observed on at least two of the STEREO A, STEREO B, and Advanced Composition (ACE) spacecraft from 2009-2013. At least one observation with a spacecraft longitudinal separation of $\geq 80^\circ$ from the flare source was required for each event. On the basis of event onset delays, and especially anisotropies in the time profiles, they concluded that the broadly distributed events were the result of a wide particle distribution near the Sun and/or perpendicular diffusion. Since 20 of the 21 events were associated with large CMEs and 18 with type II radio bursts, respectively, most of their events were likely produced in shocks.

The opportunity to compare electron events at closely spaced spacecraft began with the decrease of the STEREO A - STEREO B separation angle to $< 80^\circ$ in October 2013. One could now compare onset delays and intensity profiles at STEREO A and STEREO B for common events. Source regions of such events, occurring behind the Sun, could be imaged by the STEREO A and B EUVI instruments. An examination of an electron spike event on 2 May 2014 immediately proved troublesome. Klassen et al. (2015) found a higher intensity and earlier onset at the widely longitudinally separated ($\sim 48^\circ$) STEREO A than at the nominally closely connected STEREO B. They suggested the particle injection was non-radial followed by propa-

gation in a strongly non-radially diverging magnetic field to explain the observations.

An impulsive (probably classified as a pulse event by Haggerty and Roelof (2009)) electron event on 17 July 2014, suggested optimal magnetic connection of STEREO A and STEREO B to the particle source region (*Klassen et al.*, 2018) although STEREO A and STEREO B were magnetically connected 68° and 90° west of the source region. The authors suggested propagation through highly non-radial fields below the solar source surface. Bucik et al. (2018) found this event to be an intense ^{3}He- and Fe-rich event and emphasized its association with a helical blowout jet.

Klassen et al. (2016) selected four additional STEREO A and STEREO B solar electron events for study based on their determined STEREO A and STEREO B magnetic connectivity relative to the solar source regions. Two near-relativistic electron pulse events, observed at $\sim$ 18:00 UT and 24:00 UT on 1 August 2014 were associated with long and narrow EUV jets from the same AR, which lay southwest of STEREO A and STEREO B by 27° and 18°, respectively. However, contrary to expectation, STEREO A observed both electron events with earlier onsets and higher peak intensities than in STEREO B. For a third comparison electron event, on 11 October 2013, the source flare lay midway between the STEREO A and STEREO B magnetic footpoints, located 50° east and 49° west of the flare. This electron event, clearly a shock-associated ramp event, was confounding because of its much higher (12 $\times$) peak intensity and 13 min earlier onset at STEREO A than at STEREO B, despite their nearly identical magnetic separations. For their fourth event, on 25 February 2014 and another shock-associated ramp event, Klassen et al. (2016) compared STEREO A at 70° east and STEREO B at 42° east of the flare source. Again, despite the better magnetic connection of STEREO B, the electron event onset at STEREO A was 13 min earlier and the intensity higher during the first hours than at STEREO B. These two shock-associated electron events were also observed by the EPHIN instrument on SOHO (*Klassen et al.*, 2016), with onsets and peak intensity profiles typical for their

larger SOHO magnetic separations of 149° west and 125° west for 11 October and 25 February, respectively. However, the unexpected differences of these four electron events in STEREO A and STEREO B led Klassen et al. (2016) to suggest these electron intensity injections were Gaussian angular distributions superimposed with fringes or fingers.

While the previous studies of electron spike events (*Klassen et al.*, 2012) and of electron ramp events (*Dresing et al.*, 2014) were generally consistent with Gaussian intensity distributions, unexplained discrepancies were noted. The type III radio burst on 19 March 2011 appeared to track well northward and away from the magnetic footpoint of STEREO A, raising doubt about how the spike electron event could be observed at STEREO A (*Klassen et al.*, 2012). The four class-3 events of Dresing et al. (2014) are defined by higher electron anisotropies at more widely separated spacecraft than the best connected (of STEREO A, STEREO B, and ACE). The authors invoke "specific interplanetary magnetic configurations" as a possible explanation for those anisotropies. The anomalous results discussed here are all very dependent on properly locating the magnetic footpoints of the observing spacecraft.

Another problem dependent on the configuration of the interplanetary magnetic field (IMF) is the uncertainty about the solar release times of electron spike events relative to type III bursts. Klassen et al. (2011) found electron release onsets to follow within 6 min of type III burst onsets for each of six spike events observed on STEREO A on 22 February 2010. On the other hand, for a sample of eight spike events of E > 10 keV electrons observed with the Wind 3DP instrument, Wang et al. (2016) found somewhat longer electron release onset delays from type III onsets of 0 to 35 minutes. These delays bear on the question of whether the spike electrons are released during the type III burst or only after some significant delay from burst onset. Since the electron speeds are known, their deduced solar onset times depend on the assumed magnetic path lengths, with longer lengths requiring earlier onset times. Klassen et

al. (2011) used a path length of 1.04 AU, and Wang et al. (2016) a length of 1.2 AU, implying a discrepancy between their results larger than the nominal values.

The preceding studies depend on the basic assumption that the Parker spiral field (*Owens and Forsyth*, 2013), in which the solar wind convects the field radially from the Sun at a constant speed, usually determined by in situ spacecraft observations, is a good approximation to the interplanetary field traced back to an assumed solar potential field source surface (PFSS) above which the fields are radial. Below the PFSS, fields can be modeled to the photosphere. The photospheric footpoints are important for the spike and pulse electron events, whose sources are associated with small scale ($\leq$ few degrees) jets and flares. The photospheric sources may not be important for the ramp electron events, presumed to be produced by larger scale CME-driven shocks, but the accuracy of the source surface locations for those events remains to be tested.

Some earlier applications of the Parker spiral assumption to studies of SEP events were reviewed by *Kahler et al.* (2016), who ran the Air Force Data Assimilative Photospheric flux Transport - Wang-Sheeley-Arge (ADAPT-WSA) (*Arge and Pizzo*, 2000; *Arge et al.*, 2011) model to track the photospheric and 5 R_S locations of a forecasted 1 AU V_{SW} and compared those sources with the Parker spiral sources inferred from the ADAPT-WSA V_{sw} forecast. They found good agreement within several degrees except when the 1 AU solar wind lay within slow-fast interaction regions, in which case the errors could reach several tens of degrees. As outlined in Figure 5.1, the interaction regions between fast and slow solar wind streams create co-rotating interaction regions (CIRs) which contain compression regions where fast wind rams into slow wind, and rarefaction regions between them, which can greatly impact the shape and density of the IMF. The Parker spiral does not take these interaction regions into account, whereas ADAPT-WSA does feature these stream interactions when determining IMF shape. The *Kahler et al.* test of the Parker

spiral approximation was limited to comparisons within the context of the ADAPT-WSA model (2016), i.e., no spacecraft observations were used. Here we will run the ADAPT-WSA model for six of the electron SEP events discussed above to determine how well the critical Parker spiral assumption served to determine the PFSS and photospheric footpoint locations. This in turn permits a validation of the anomalous results of the STEREO A - STEREO B electron events discussed above.

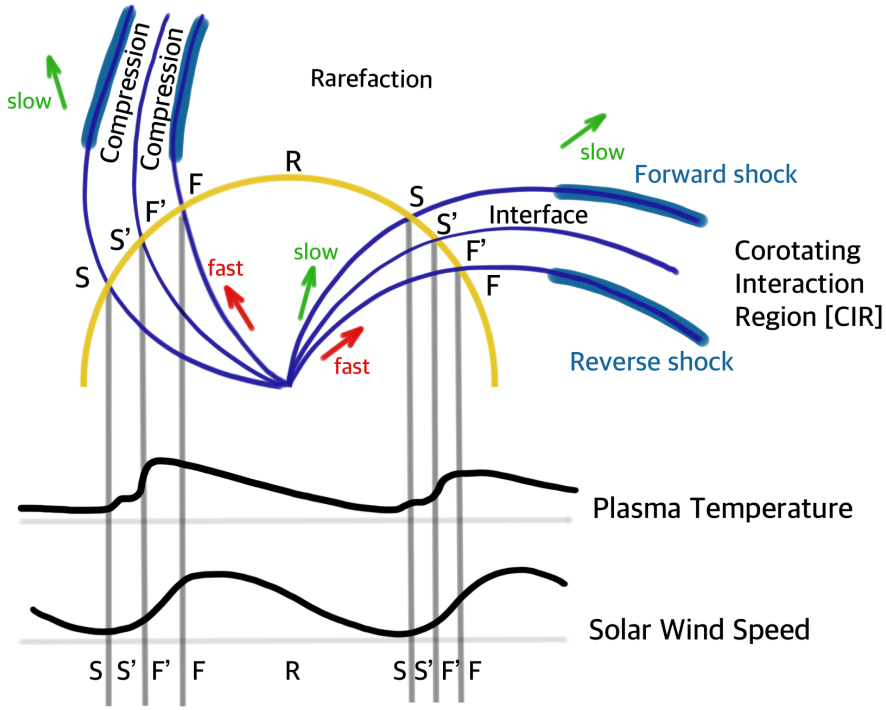

Figure 3.1: Diagram of a CIR in the solar wind. Green and red arrows indicate which regions are driven by slow and fast solar wind, respectively, these solar wind speeds are also marked with S for slow and F for fast. Blue magnetic field lines show the compression regions of bunched magnetic field lines and the rarefaction region between them where the density of magnetic field lines is lower. The golden arc represents the path of a spacecraft which observes the plasma temperature and solar wind speed depicted in black in the lower portion of the diagram. Based on a diagram of a CIR from (*Richardson*, 2004).

3.4 Event Selection and Criteria

We selected six energetic (> 50 keV) electron SEP events discussed by Klassen et al. (2015; 2016; 2018). Event 1 was observed on 11 October 2013, Event 2 on 25 February 2014, Event 3 on 02 May 2014, Event 4 on 17 July 2014, and Events 5 and 6 on 01 August 2014. Each event was observed by both STEREO A and STEREO B while the spacecraft were separated by less than 72° in angular separation.

Each of these six events were observed at times without preceding coronal mass ejections and when interactions with preceding SEP events were minimal. By considering SEP events that are not further complicated by interactions with other propagating structures or particle events, we are better able to isolate the differences between modeling the spacecraft magnetic connectivity using ADAPT-WSA versus the Parker Spiral approximation.

From October 11th, 2013 through August 1st, 2014, STEREO A and STEREO B are spaced apart by 32° to 72° of angular separation. This separation gives a unique opportunity for analyzing events observed at both spacecraft. At this separation distance, we can evaluate the spatial extent of events that are being simultaneously observed. The first of these events was observed on October 11th, 2013 when the spacecraft were separated by 72°, the second event was observed on February 25th, 2014 when the spacecraft were separated by 47°, the third on May 2nd, 2014 when the spacecraft were separated by 38°, the fourth on July 17th, 2014 when the spacecraft were separated by 32°, and the fifth and sixth events were observed on August 1st, 2014 when the spacecraft were separated by 34° of angular separation. Figures 3.2 and 3.3 display maps with the spacecraft locations for the first event on October 11th, 2013 and the fourth event on July 17th, 2014 in the ecliptic plane in Heliocentric Earth Ecliptic (HEE) coordinates. These maps display the range of spacecraft separation for these events relative to the Sun-Earth line from which the Solar Heliospheric Observatory (SOHO) and the Advanced Composition Explorer (ACE) observe the

Sun. Events 1, and 2 were additionally observed by the ACE or SOHO spacecraft at the L1 Lagrange point along the Sun-Earth line. Additional spacecraft location maps for the other SEP events are available as supplemental information.

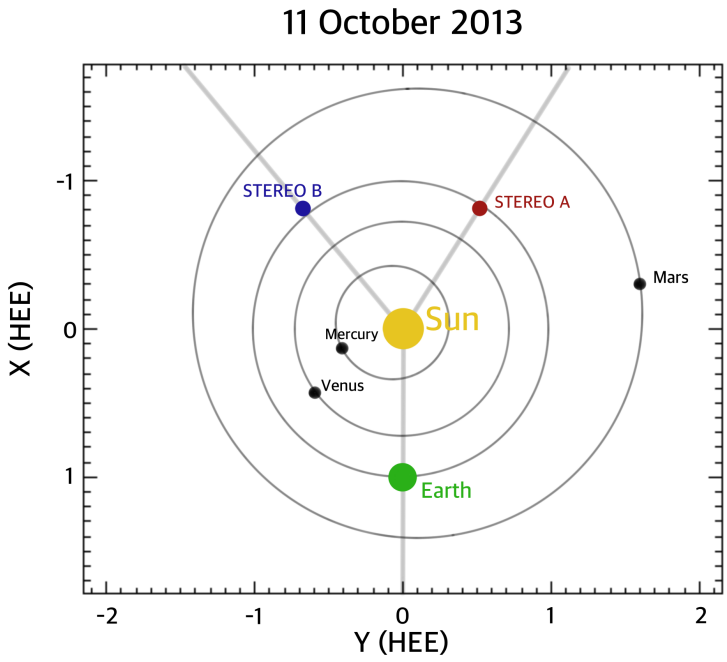

Figure 3.2: Map of the relative STEREO A, STEREO B and Earth locations in the heliocentric earth ecliptic plane. Coordinates are given in HEE. The spacecraft and planetary locations are shown at the time of Event 1 on October 11th, 2013 when the STEREO A and STEREO B angular separation was 72°. Of the six SEP events considered in this study, this was the furthest separation angle.

3.5 Modeling Methods

To model the magnetic connectivity for each observing spacecraft for each of the six particle events, we used the coupled ADAPT-WSA model. ADAPT-WSA is the Air Force Data Assimilative Photospheric flux Transport - Wang-Sheeley-Arge solar wind forecast model.

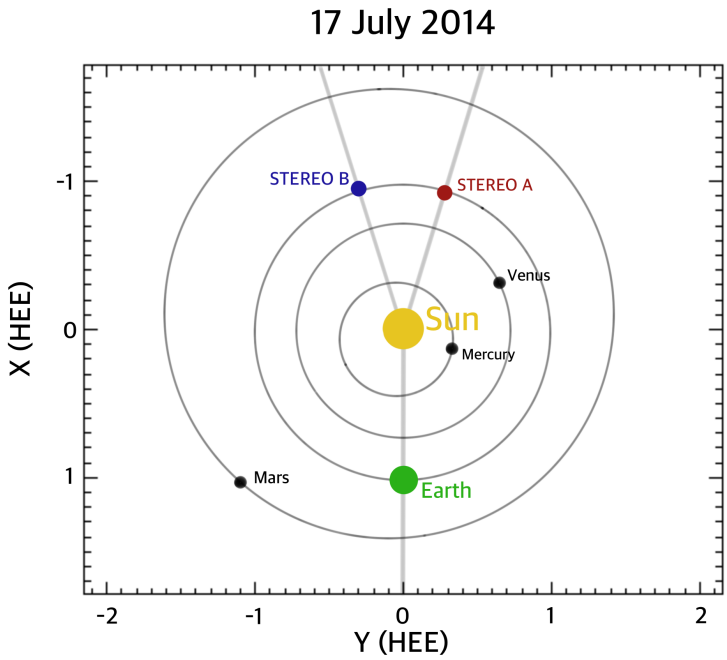

Figure 3.3: Map of the relative STEREO A, STEREO B and Earth locations in the heliocentric earth ecliptic plane. Coordinates are given in HEE. The spacecraft and planetary locations are shown at the time of Event 4 on July 17th, 2014 when the STEREO A and STEREO B angular separation was 32°. Of the six SEP events considered in this study, this was the narrowest separation angle.

ADAPT uses input synoptic maps from the Global Oscillation Network Group (GONG) ground-based magnetogram observations. From these GONG magnetograms, ADAPT stitches these observations of the photospheric magnetic field together and using photospheric flux transport modeling, forward models the photospheric magnetic flux to create an ensemble of synchronic photospheric magnetic field maps. ADAPT was run for multiple modeling runs, to create prediction maps for eight forecast prediction windows, 1-day through 7-day. Each ADAPT modeling run created an ensemble of 12 prediction maps, referred to subsequently as modeling realizations, which varied based on random walk variation in flux emergence and surface transport. Thus, for each SEP event, for each spacecraft, we had 12 realizations of ADAPT

prediction maps for each of the eight forecast windows.

These ADAPT photospheric, synoptic magnetic maps were then used as input into the Wang-Sheeley-Arge (WSA) solar wind model. Using the modeled magnetic active regions of the ADAPT map, WSA then modeled from the photospheric magnetic field out to a 2.5 R_S Schatten current sheet above which field lines are modeled to be open, but not necessarily radial (*Schatten*, 1972). From the 2.5 R_S Schatten current sheet WSA models the field lines to a 5 R_S potential field source surface (PFSS) using the magnetic expansion factor. The PFSS was modeled at the heliospheric latitude of the spacecraft's orbital plane, as was done by Klassen et al. for their 2.5 R_S PFSS (2015; 2016; 2018). From the 5 R_S PFSS, WSA ballistically modeled the solar wind flow out to the spacecraft locations at 1 AU from the Sun using observed solar wind velocities and magnetic polarities as empirical modeling validation while taking solar wind co-rotating stream interactions into account, such as seen diagrammed in Figure 5.1.

Thus, these runs of the coupled ADAPT-WSA model produced 12 realizations of solar wind velocity predictions and 12 realizations of heliospheric magnetic field (HMF) magnetic polarity predictions per eight forecast window per spacecraft per event. To extract useful modeled magnetic field connectivity predictions from these results, we then down-selected to optimal modeling runs and those field lines relevant to our SEP event observations.

To best select the most relevant magnetic field predictions produced by ADAPT, we used only those realizations which used forecast windows that corresponded to magnetic observations at the time the relevant solar wind tracing our magnetic connectivity actually left the Sun. To achieve this, we selected which of the 1-day to 7-day forecast windows to use based on solar wind travel times. For example, when the observed solar wind proton velocity was observed to be about 390 km/s as it was at STEREO A for Event 2, the travel time to 1 AU was estimated and the 4-day fore-

cast window results were selected. An example observation plot with corresponding ADAPT-WSA predictions for an ADAPT-WSA modeling realization for Event 2 is shown in Figure 3.4.

For each event we selected the top five (or fewer) most promising realizations per spacecraft based on best predicted HMF direction and proton bulk velocity observed within a 48 hour window surrounding the observations. Each realization is produced by a separate run of ADAPT-WSA and yields a different collection of modeled magnetic field lines to represent the connectivity of the spacecraft to the photosphere. Example prediction plots can be seen in Figures 3.4 and 3.5.

Figure 3.4 gives the ADAPT-WSA solar wind velocity predictions for Event 2 for the STEREO A spacecraft for the whole modeling period as calculated from the seventh realization of the forecasts made using the 4-day forecast ADAPT magnetic field maps. Figure 3.5 gives the ADAPT-WSA IMF polarity predictions for Event 2 for the STEREO A spacecraft for the whole modeling period as calculated from the seventh realization of the forecasts made using the 4-day forecast ADAPT magnetic field maps. The regions boxed in light blue on both figures mark the region near the spacecraft observation time of the event, which we considered when determining optimal realizations for down-selection. This seventh realization modeled the correct polarity for the majority of the time period and had reasonable agreement with the velocity predictions. Using these two criteria, this realization fell into the top 5 realizations for this event at this spacecraft, so was selected as one of the optimal realizations and the magnetic footpoints modeled in this realization were used in the subsequent analysis of this event.

Once the most promising forecast window and modeling realizations were selected, we then extracted those field lines which were relevant to the timing of the SEP events and the spacecraft locations. For each promising realization we extracted the modeled field lines that corresponded best to the spacecraft connectivity based on observed

event onset timing +/- 216 minutes (or 3.6 hours), which corresponds to an angular range of +/- 2°.

Thus each of the extracted field line footpoints corresponds to field lines modeled to be connected to the spacecraft within 3.6 hours of the observed event onset, but based on GONG magnetograms corresponding to the photospheric magnetic field configuration corresponding to the solar wind that shaped these field lines.

An example of the collection of extracted field lines for Event 2 are shown in Table 3.1. Such extracted footpoint collections were created for each of the six events, for each of the spacecraft. Table 3.1 displays the selected optimal forecast window and realizations in column 1, and displays the separation between the footpoint and the associated solar flare location in degrees in column 2, while the third and fourth columns show the full set of extracted footpoints for Event 2. As can be seen in Table 3.1, the number of field line footpoints per realization is not consistent. For example, 31 footpoints were modeled for the 5th realization of STEREO A, whereas only 4 footpoints were extracted from the 8th realization. When subsequently evaluated, each footpoint was weighted equally regardless of the number of footpoints from each realization, presuming that any modeled field line is as valid as any other for these optimal ADAPT-WSA modeling realizations.

When Klassen et al. examined these SEP events, their analysis depended on a determination of magnetic field line connections using the Parker spiral approximation and a 2.5 R_S potential field source surface (PFSS) (2015; 2016; 2018). ADAPT-WSA runs used for our analysis used a PFSS at 5 R_S. We discuss the resulting modeled footpoints as they relate to each other and the impacts on interpreting the observation of these SEP events in Section 3.6.

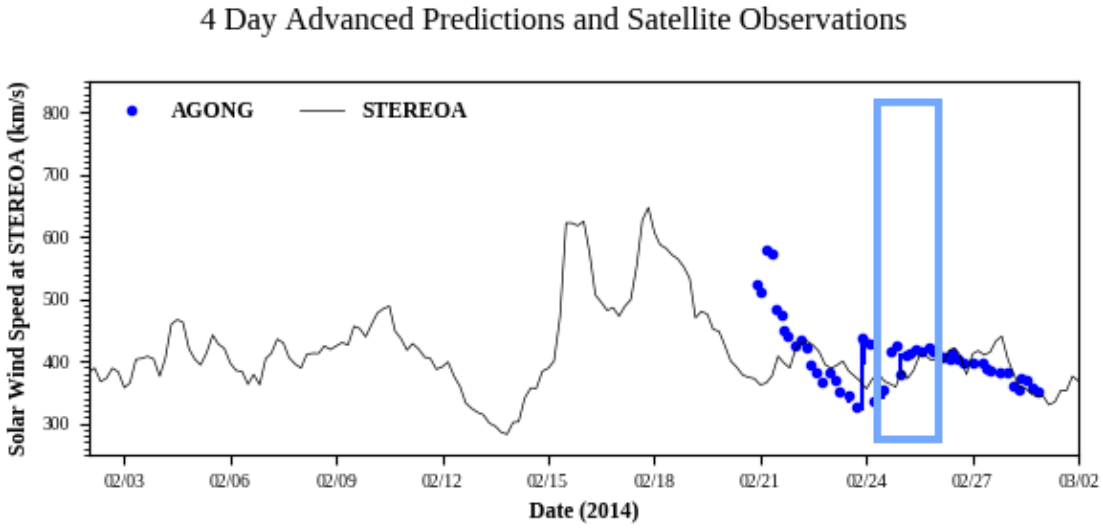

Figure 3.4: ADAPT-WSA predictions of solar wind speed for Event 2 at Stereo A from realization R007 using a GONG magnetogram of 4 days earlier. The light blue box surrounds the 48 hour window analyzed for agreement. Blue data points are the ADAPT-WSA model predictions. Black data are the observed values at the Stereo A spacecraft.

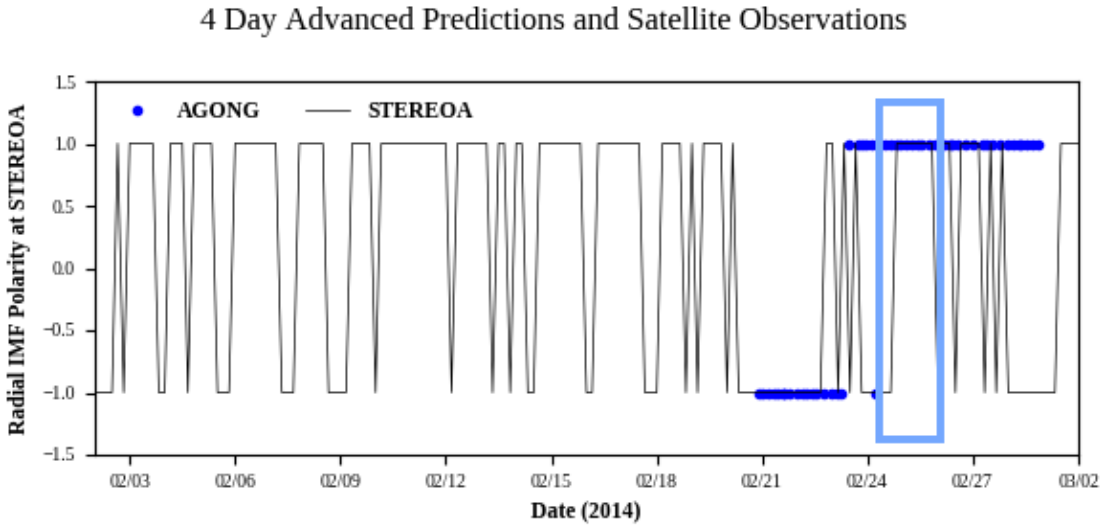

Figure 3.5: ADAPT-WSA predictions of magnetic field polarity for Event 2 at Stereo A from realization R007 using a GONG magnetogram of 4 days earlier. The light blue box surrounds the 48 hour window analyzed for agreement. Blue data points are the ADAPT-WSA model predictions. Black data are the observed values at the Stereo A spacecraft.

Event 2 ADAPT-WSA Modeled Magnetic Connectivity Results

Event 2 for STEREO A at 2014-02-25 01:09:00 (108, -13)

Forecast Window, Realization	Field Line to Flare Source Separation [deg.]	Field Line Footpoint Locations (long.,lat.)	Number of ADAPT-WSA Field Lines Comprising Results
04-Day Forecast, R001	105° to 105°	(30, 5) (28, 5) (26, 5) (29, 5)	4
04-Day Forecast, R004	56° to 105°	(28, 5) (26, 5) (29, 5) (42, 5)	4
04-Day Forecast, R005	99° to 105°	(45, 5) (43, 5) (41, 5) (39, 5) (37, 5) (35, 5) (33, 5) (31, 5) (50, 5) (48, 5) (46, 5) (44, 5) (42, 5) (40, 5) (38, 5) (36, 5) (34, 5) (32, 5) (30, 5) (28, 5) (26, 5) (45, 5) (43, 5) (41, 5) (39, 5) (37, 5) (35, 5) (33, 5) (31, 5) (29, 5) (27, 5)	31
04-Day Forecast, R007	102° to 106°	(30, 5) (28, 5) (26, 5) (24, 5) (43, 5) (41, 5) (39, 5) (37, 5) (35, 5) (33, 5) (31, 5) (29, 5)	12
04-Day Forecast, R008	104° to 105°	(30, 5) (28, 5) (26, 5) (29, 5)	4

Event 2 for STEREO B at 2014-02-25 01:22:00 (108, -13)

Forecast Window, Realization	Field Line to Flare Source Separation [deg.]	Field Line Footpoint Locations (long.,lat.)	Number of ADAPT-WSA Field Lines Comprising Results
03-Day Forecast, R000	52° to 52°	(61, 7) (62, 7) (60, 7) (62, 7) (60, 7) (61, 7) (59, 7)	7
03-Day Forecast, R001	51° to 52°	(62, 7) (61, 7) (59, 7) (62, 7) (60, 7) (60, 7) (59, 7)	7
03-Day Forecast, R008	52° to 52°	(62, 7) (61, 7) (59, 7) (60, 7) (60, 7) (59, 7)	6
03-Day Forecast, R009	52° to 52°	(62, 7) (61, 7) (59, 7) (62, 7) (60, 7) (60, 7) (59, 7)	7
03-Day Forecast, R011	52° to 53°	(62, 7) (61, 7) (59, 7) (62, 7) (60, 7) (60, 7) (59, 7)	7

Event 2 for ACE at 2014-02-25 02:04:00 (108, -13)

Forecast Window, Realization	Field Line to Flare Source Separation [deg.]	Field Line Footpoint Locations (long.,lat.)	Number of ADAPT-WSA Field Lines Comprising Results
04-Day Forecast, R003	129° to 178°	(254, -7) (252, -7) (250, -7) (248, -7) (253, -7) (252, -7) (250, -7) (248, -7) (246, -7) (244, -7) (242, -7) (240, -7) (238, -7) (240, -7) (238, -7)	15
04-Day Forecast, R006	129° to 178°	(254, -7) (252, -7) (253, -7) (252, -7) (250, -7) (248, -7) (246, -7) (244, -7) (242, -7) (240, -7) (238, -7) (250, -7) (248, -7) (246, -7) (244, -7) (242, -7) (240, -7) (238, -7)	18
04-Day Forecast, R007	129° to 172°	(250, -7) (253, -7) (250, -7) (248, -7) (246, -7) (244, -7) (242, -7) (240, -7) (238, -7)	9
04-Day Forecast, R008	130° to 175°	(253, -7) (254, -7) (252, -7) (250, -7) (248, -7) (246, -7) (244, -7) (242, -7) (240, -7)	9
04-Day Forecast, R010	130° to 172°	(253, -7) (246, -7) (244, -7) (242, -7) (240, -7)	5

Table 3.1: Table of extracted magnetic footpoints modeled using ADAPT-WSA for SEP Event 2 on 25 February 2014. Each subtable presents the connectivity results for each of the observing spacecraft, STEREO A, STEREO B and ACE. Column 1: The selected forecast window and modeling realization. Column 2: The range of angular separations between the location of the associated solar flare and the modeled footpoints. Column 3: The set of extracted ADAPT-WSA modeled magnetic footpoints. Column 4: The number of footpoints comprising the extracted set for each forecast window and realization.

3.6 Results and Discussion

The resulting ranges of the modeled magnetic connectivity of each spacecraft to the PFSS for each of the six near-relativistic electron SEP events in this study are displayed in Table 3.2. This table presents the Parker spiral approximated footpoints determined for each event by Klassen et al. (2015; 2016; 2018). The ADAPT-WSA mean footpoints for each event for each spacecraft and the separation distances between footpoints from the two methods are presented for comparison.

The ADAPT-WSA modeled photospheric footpoint results are presented in Table 3.3. This table presents the location of the associated EUV flares observed by the STEREO EUVI instruments for each event with the modeled ADAPT-WSA footpoints at the photosphere. The table includes the separation distances between these ADAPT-WSA photospheric footpoints and both the flare locations and the Parker spiral 2.5 R_S PFSS footpoints (*Klassen et al.*, 2015, 2016, 2018).

What follows in the rest of Section 3.6 are the results for the modeled magnetic connectivity for each event, a comparison between the ADAPT-WSA connectivity and the Parker spiral approximated connectivity, and discussion of these results compared to additional observational details relevant to each event. Observations of the near-relativistic 30 keV - 400 keV electron time profiles from the SEPT instruments, EUV images from the EUVI instruments, and observed onset times of type III radio bursts from the SWAVES instruments, all on board the STEREO spacecraft, are discussed when relevant.

3.6.1 Event 1: 11 October 2013

The first event of our study, observed on October 11th, 2013 is a shock-associated electron ramp event which was observed by both STEREO A and STEREO B when their angular separation was 72°, which was the furthest of the six events in this study. This event was observed first by STEREO A at 07:34 UT, then by STEREO

Comparison of ADAPT-WSA and Klassen et al. Modeled Magnetic Connectivity

Event 1: Oct 11 2013

Spacecraft	ADAPT-WSA Mean (long.,lat.) Modeled at 5 R_s	ADAPT-WSA Range of (long.,lat.) Modeled at 5 R_s	Number of Modeled Footpoints Comprising Each Range	Klassen et al. (long.,lat.) Modeled at 2.5 R_s	ADAPT-WSA vs Klassen et al. Longitude Difference
SOHO/ACE	(242, 6)	(236, 6) to (247, 6)	18	(240, 6)	2°
STEREOA	(32, -7)	(28, -7) to (35, -7)	27	(40, -7)	8°
STEREOB	(106, -3)	(89, -3) to (122, -3)	85	(127, -2)	21°

Event 2: Feb 25 2014

Spacecraft	ADAPT-WSA Mean (long.,lat.) Modeled at 5 R_s	ADAPT-WSA Range of (long.,lat.) Modeled at 5 R_s	Number of Modeled Footpoints Comprising Each Range	Klassen et al. (long.,lat.) Modeled at 2.5 R_s	ADAPT-WSA vs Klassen et al. Longitude Difference
SOHO/ACE	(246, -7)	(238, -7) to (254, -7)	56	(236, -7)	10°
STEREOA	(35, 6)	(24, 5) to (50, 6)	55	(39, 6)	4°
STEREOB	(60, 7)	(59, 7) to (62, 7)	34	(70, 7)	10°

Event 3: May 2 2014

Spacecraft	ADAPT-WSA Mean (long.,lat.) Modeled at 5 R_s	ADAPT-WSA Range of (long.,lat.) Modeled at 5 R_s	Number of Modeled Footpoints Comprising Each Range	Klassen et al. (long.,lat.) Modeled at 2.5 R_s	ADAPT-WSA vs Klassen et al. Longitude Difference
SOHO/ACE	N/A	N/A	N/A	N/A	N/A
STEREOA	(225, 6)	(223, 6) to (226, 6)	28	(253, 6)	28°
STEREOB	(271, 3)	(266, 3) to (275, 3)	29	(300, 3)	29°

Event 4: July 17 2014

Spacecraft	ADAPT-WSA Mean (long.,lat.) Modeled at 5 R_s	ADAPT-WSA Range of (long.,lat.) Modeled at 5 R_s	Number of Modeled Footpoints Comprising Each Range	Klassen et al. (long.,lat.) Modeled at 2.5 R_s	ADAPT-WSA vs Klassen et al. Longitude Difference
SOHO/ACE	N/A	N/A	N/A	(169, 4)	N/A
STEREOA	(334, -2)	(329, -2) to (341, -2)	47	(338, -3)	4°
STEREOB	(2, -6)	(1, -6) to (3, -6)	3	(0, -6)	2°

Event 5: Aug 01 2014

Spacecraft	ADAPT-WSA Mean (long.,lat.) Modeled at 5 R_s	ADAPT-WSA Range of (long.,lat.) Modeled at 5 R_s	Number of Modeled Footpoints Comprising Each Range	Klassen et al. (long.,lat.) Modeled at 2.5 R_s	ADAPT-WSA vs Klassen et al. Longitude Difference
SOHO/ACE	(308, 6)	(301, 5) to (321, 6)	75	(332, 6)	24°
STEREOA	(107, -4)	(105, -4) to (110, -4)	26	(133, -5)	26°
STEREOB	(158, -7)	(155, -7) to (162, -7)	13	(143, -7)	15°

Event 6: Aug 01 2014

Spacecraft	ADAPT-WSA Mean (long.,lat.) Modeled at 5 R_s	ADAPT-WSA Range of (long.,lat.) Modeled at 5 R_s	Number of Modeled Footpoints Comprising Each Range	Klassen et al. (long.,lat.) Modeled at 2.5 R_s	ADAPT-WSA vs Klassen et al. Longitude Difference
SOHO/ACE	(331, 5)	(319, 5) to (347, 5)	99	(318, 6)	13°
STEREOA	(105, -4)	(102, -4) to (107, -4)	22	(133, -5)	28°
STEREOB	(154, -7)	(141, -7) to (166, -7)	33	(137, -7)	17°

Table 3.2: Table of ADAPT-WSA modeled 5 R_S footpoints for SEP Events 1 - 6 observed by STEREO A and B in 2013-2014 compared to the Klassen et al. magnetic connectivity using the Parker spiral approximation (2015; 2016; 2018). Column 1: Observing spacecraft. Column 2: Mean ADAPT-WSA footpoint location at the 5 R_S PFSS. Column 3: Range of ADAPT-WSA footpoint locations at the 5 R_S PFSS. Column 4: The number of modeled footpoints that comprised the range of ADAPT-WSA results for the set of extracted modeled footpoints for that spacecraft. Column 5: Klassen at al. modeled footpoints at the 2.5 R_S PFSS using the Parker spiral approximation (2015; 2016; 2018). Column 6: Longitude difference between the ADAPT-WSA mean 5 R_S footpoints and the corresponding Klassen et al. 2.5 R_S footpoints.

Comparison of SEP and Flare Arrivals and Locations

Event 1: Oct 11 2013

Spacecraft	Photospheric Flare Location (long.,lat.)	ADAPT-WSA Mean Modeled (long.,lat.) at the Photosphere	ADAPT-WSA Flare-Connectivity Longitude, Total Difference	Klassen et al. Connectivity at 2.5 R_s (long.,lat.)	Klassen et al. Flare-Connectivity Longitude, Total Difference	Observed EUV Flare Arrival Time	Observed SEP Arrival Time	Flare-SEP Arrival Time Diff.
SOHO/ACE	(83, 21)	(264, -18)	179°, 183°	(240, 6.0)	157°, 158°	07:11 UT	11:10 UT	239 minutes
STEREOA	(83, 21)	(37, 13)	46°, 46°	(40, -7.3)	43°, 51°	07:11 UT	07:34 UT	23 minutes
STEREOB	(83, 21)	(95, 19)	12°, 13°	(127, -2.5)	44°, 50°	07:11 UT	07:47 UT	36 minutes

Event 2: Feb 25 2014

Spacecraft	Photospheric Flare Location (long.,lat.)	ADAPT-WSA Mean Modeled (long.,lat.) at the Photosphere	ADAPT-WSA Flare-Connectivity Longitude, Total Difference	Klassen et al. Connectivity at 2.5 R_s (long.,lat.)	Klassen et al. Flare-Connectivity Longitude, Total Difference	Observed EUV Flare Arrival Time	Observed SEP Arrival Time	Flare-SEP Arrival Time Diff.
SOHO/ACE	(108, -13)	(252, -15)	144°, 144°	(236, -7.1)	128°, 128°	00:46 UT	02:04 UT	78 minutes
STEREOA	(108, -13)	(5, -11)	103°, 103°	(39, 5.9)	69°, 72°	00:46 UT	01:09 UT	23 minutes
STEREOB	(108, -13)	(65, 16)	43°, 52°	(70, 7.2)	38°, 43°	00:46 UT	01:22 UT	36 minutes

Event 3: May 2 2014

Spacecraft	Photospheric Flare Location (long.,lat.)	ADAPT-WSA Mean Modeled (long.,lat.) at the Photosphere	ADAPT-WSA Flare-Connectivity Longitude, Total Difference	Klassen et al. Connectivity at 2.5 R_s (long.,lat.)	Klassen et al. Flare-Connectivity Longitude, Total Difference	Observed EUV Flare Arrival Time	Observed SEP Arrival Time	Flare-SEP Arrival Time Diff.
SOHO/ACE	(250, -8)	N/A	N/A	N/A	N/A	05:09 UT	N/A	N/A
STEREOA	(250, -8)	(235, -8)	15°, 15°	(253, 6.1)	3°, 14°	05:09 UT	05:33 UT	24 minutes
STEREOB	(250, -8)	(247, -11)	3°, 4°	(300, 2.7)	50°, 51°	05:09 UT	05:32 UT	23 minutes

Event 4: July 17 2014

Spacecraft	Photospheric Flare Location (long.,lat.)	ADAPT-WSA Mean Modeled (long.,lat.) at the Photosphere	ADAPT-WSA Flare-Connectivity Longitude, Total Difference	Klassen et al. Connectivity at 2.5 R_s (long.,lat.)	Klassen et al. Flare-Connectivity Longitude, Total Difference	Observed EUV Flare Arrival Time	Observed SEP Arrival Time	Flare-SEP Arrival Time Diff.
SOHO/ACE	(270, -10)	N/A	N/A	(169, 4.5)	101°, 102°	08:08 UT	N/A	N/A
STEREOA	(270, -10)	(273, -9)	3°, 3°	(338, -2.8)	68°, 68°	08:08 UT	08:42 UT	34 minutes
STEREOB	(270, -10)	(42, -11)	132°, 132°	(0, -5.9)	90°, 90°	08:08 UT	08:34 UT	26 minutes

Event 5: Aug 01 2014

Spacecraft	Photospheric Flare Location (long.,lat.)	ADAPT-WSA Mean Modeled (long.,lat.) at the Photosphere	ADAPT-WSA Flare-Connectivity Longitude, Total Difference	Klassen et al. Connectivity at 2.5 R_s (long.,lat.)	Klassen et al. Flare-Connectivity Longitude, Total Difference	Observed EUV Flare Arrival Time	Observed SEP Arrival Time	Flare-SEP Arrival Time Diff.
SOHO/ACE	(155, -22)	(271, -10)	116°, 116°	(332, 5.8)	177°, 179°	16:13 UT	N/A	N/A
STEREOA	(155, -22)	(120, -32)	35°, 36°	(133, -4.6)	22°, 28°	16:13 UT	16:34 UT	21 minutes
STEREOB	(155, -22)	(188, -34)	33°, 35°	(143, -6.8)	12°, 19°	16:13 UT	16:54 UT	41 minutes

Event 6: Aug 01 2014

Spacecraft	Photospheric Flare Location (long.,lat.)	ADAPT-WSA Mean Modeled (long.,lat.) at the Photosphere	ADAPT-WSA Flare-Connectivity Longitude, Total Difference	Klassen et al. Connectivity at 2.5 R_s (long.,lat.)	Klassen et al. Flare-Connectivity Longitude, Total Difference	Observed EUV Flare Arrival Time	Observed SEP Arrival Time	Flare-SEP Arrival Time Diff.
SOHO/ACE	(155, -22)	(272, -12)	117°, 117°	(318, 5.8)	163°, 165°	23:24 UT	N/A	N/A
STEREOA	(155, -22)	(120, -31)	35°, 37°	(133, -4.6)	22°, 28°	23:24 UT	23:45 UT	21 minutes
STEREOB	(155, -22)	(164, -19)	9°, 10°	(137, -6.8)	18°, 24°	23:24 UT	23:54 UT	30 minutes

Table 3.3: Table of ADAPT-WSA modeled photospheric footpoints for SEP Events 1 - 6 compared to the associated Solar flare locations and the Klassen et al. magnetic connectivity using the Parker spiral approximation (2015; 2016; 2018). Column 1: Observing spacecraft. Column 2: Photospheric longitude and latitude of the associated solar flare (*Klassen et al.*, 2015, 2016, 2018). Column 3: Mean ADAPT-WSA footpoint location at the photosphere. Column 4: Longitude difference and total angular difference between the flare location and the ADAPT-WSA modeled photospheric footpoint. Column 5: Klassen et al. 2.5 R_S footpoint locations (*Klassen et al.*, 2015, 2016, 2018). Column 6: Longitude difference and total angular difference between the flare location and the Klassen et al. modeled 2.5 R_S PFSS footpoint. Column 7: Arrival time of associated observed EUV solar flare. Column 8: Observed electron event arrival time at the observing spacecraft. Column 9: Difference in EUV solar flare and electron event arrival times.

B at 07:47 UT, and then much later, after 11:10 UT, the EPHIN instrument on SOHO observed the electron onset with a much lower peak intensity (*Klassen et al.*, 2016). The event was associated with an M1.5 X-ray flare, a full-halo CME, circular EIT wave and type II radio burst observed at 07:11 UT, and a type III radio burst observed at 07:12 UT - 07:25 UT by SWAVES (*Klassen et al.*, 2016).

As can be seen in Figure 3.6, the ADAPT-WSA modeled 5 R_S PFSS footpoints for Event 1 ranged from 28° to 35° longitude, with a mean longitude of 32° for STEREO A, and from 89° to 122° longitude, with a mean longitude of 106° for STEREO B. ADAPT-WSA footpoints for Event 1 at SOHO or ACE ranged from 236° to 247° longitude, with a mean longitude of 242°.

The Parker spiral approximated footpoints were located at a longitude of 40° for STEREO A, an average of 8° east of the ADAPT-WSA footpoints, and at a longitude of 127° for STEREO B, an average of 21° east of the ADAPT-WSA footpoints (*Klassen et al.*, 2016). As can be seen in Figure 3.6, for all three spacecraft there is overlap between the ADAPT-WSA 5 R_S footpoints and the Parker spiral approximated 2.5 R_S footpoints for Event 1 (*Klassen et al.*, 2016).

When Klassen et al. examined this October 11th event, they concluded there was a non-uniform particle distribution or strongly non-radial magnetic field structure between the flare and the PFSS (*Klassen et al.*, 2016). To analyze whether the ADAPT-WSA offers any clues for analysis of this hypothesis, we compare the separation distances between the spacecraft connectivity at the photosphere and the source flare location, as can be seen in Table 3.3. Modeling with ADAPT-WSA suggests that STEREO A was connected to the photosphere 46° east of the flare, STEREO B was connected 13° west of the flare and SOHO was connected 183° from the flare. In contrast the Parker spiral 2.5 R_S footpoints suggested STEREO A was connected 51° east of the flare, STEREO B was 50° west of the flare, and SOHO was 158° west of the source flare. As such, ADAPT-WSA models STEREO B as connected closer

to the flare source location than the Parker spiral, and STEREO A further from the source flare than the Parker spiral, at both the photosphere and the 5 R_S PFSS. Yet, STEREO A observed the electron event first by 13 minutes and with higher particle intensities.

Thus, our ADAPT-WSA footpoint modeling for this event at the 5 R_S PFSS and at the photosphere do not support the theory that a strongly non-radial field below the PFSS would explain away the arrival time and connectivity discrepancies observed. This leaves the possibility that this event is highly non-uniform. However, we propose that modeling the spacecraft connectivity during these events might fail to solve onset time and intensity discrepancies due rather to variations in the IMF propagation of these field lines caused by the associated full-halo CME (which was not included in our ADAPT-WSA modeling) and interplanetary shock acceleration as is known to be associated with near-relativistic ramp events (*Haggerty and Roelof*, 2009) and was shown to be associated with this event (and with Event 2) by Cohen et al. (2017).

3.6.2 Event 2: 25 February 2014

Event 2 was a shock-associated electron ramp event observed on 25 February 2014. The event was observed by STEREO A at 01:09 UT, STEREO B at 01:22 UT and SOHO before 02:04 UT. The initial near-relativistic electron intensity observed by the SEPT instruments was very similar at both STEREO A and STEREO B, with STEREO A having a higher intensity decay phase. The event was associated with an X4.9 X-ray flare starting at 00:39 UT, simultaneously a type II radio burst and interplanetary type III burst observed at 00:46 UT, a fast asymmetric full-halo CME, and an EIT-wave (*Klassen et al.*, 2016). The flaring active region associated with these events was at (108,-13) as seen in Figure 3.7.

As shown in Figure 3.7, the range of ADAPT-WSA determined 5 R_S PFSS foot-

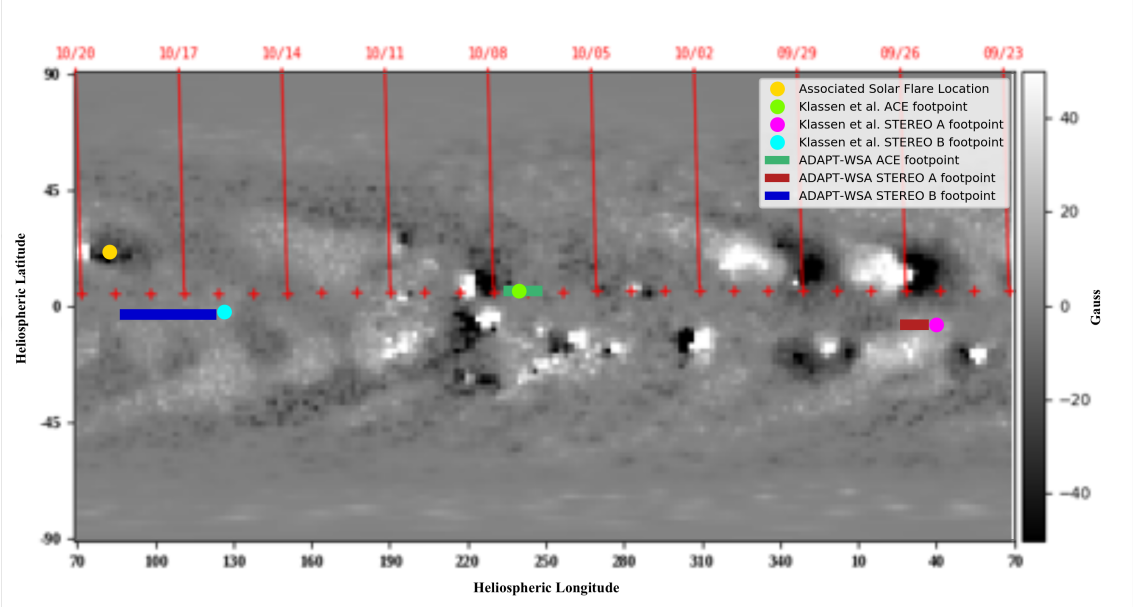

Figure 3.6: Map of SEP Event 1 ADAPT-WSA modeled 5 R_S footpoints and Klassen et al. 2.5 R_S footpoints (2016). These modeled PFSS footpoints are overlaid on a photospheric synoptic magnetic field map from ground-based GONG magnetograms. Coordinates are in heliospheric latitude and Carrington longitude. The solar equator is at 0° latitude and the Earth ecliptic plane is marked by red plus symbols. Vertical red lines mark the central meridians, labeled with the corresponding observational dates, of the GONG magnetograms that form the composite synoptic map.

points for STEREO A were found to range from 24° to 50° longitude, with a mean longitude of 35°, and for STEREO B from 59° to 62° longitude, with a mean longitude of 60°. This results in modeled separation of 76° east of the associated flaring active region for STEREO A, and 52° east of the active region for STEREO B.

This event was observed by the EPHIN instrument on SOHO with a weaker onset and peak intensity profile than seen by the STEREO spacecraft (*Klassen et al.*, 2016), which is consistent with the ADAPT-WSA modeled footpoints for SOHO/ACE which range from 238° to 254° longitude, with a mean footpoint at 246°. These footpoints result in the mean separation from the flare active region of 138°, which is a much further separation than either STEREO A or B.

Klassen et al. modeled the footpoints of this event using a Parker spiral approximation and a 2.5 R_S PFSS (2016), this suggested footpoints for STEREO A at 39° longitude, which was 72° east of the flaring region, for STEREO B at 70° longitude, which was 43° east of the flaring region, and for SOHO at 236° longitude, which was 128° west of the flaring region.

The ADAPT-WSA modeled photospheric footpoints ranged from (2,-14) to (9,-12) for STEREO A with a mean longitude of 4° (with one additional modeled footpoint at 61° longitude), yielding a modeled separation of ° from the source location, from (65,16) to (66,17) with a mean longitude at 65° for STEREO B, which is a modeled separation of 104° east of the source location, and from (237,-22) to (296,-10) with a mean longitude at 252° for SOHO or ACE, which is a modeled separation of 144° west of the flare location.

ADAPT-WSA modeling suggests that the 5 R_S PFSS footpoints for STEREO A are on average 76° east of the source flare, which is 4° further east from the source region than the Parker spiral footpoints, and for STEREO B on average 52° east of the source region, which is 9° further east than the Parker spiral approximation (*Klassen et al.*, 2016). Both methods of determining footpoints suggested that STEREO B

was better connected than STEREO A or SOHO to the source region, yet STEREO A still observed the event first by 13 minutes and with greater decay phase intensity.

When Klassen et al. examined this event, they concluded there was a non-uniform particle distribution or strongly non-radial magnetic field structure between the flare and the PFSS (2016). The ADAPT-WSA footpoint modeling for this event at the 5 R_S PFSS and at the photosphere do not support the theory that a strongly non-radial field below the PFSS would explain away the arrival time and connectivity discrepancies observed. This leaves the possibility that this event is highly non-uniform. However, we propose that modeling the spacecraft connectivity during these events might fail to produce a clear picture due rather to variations in the IMF propagation of these field lines caused by the associated full-halo CME (which was not included in our ADAPT-WSA modeling) and interplanetary shock acceleration as is known to be associated with near-relativistic ramp events (*Haggerty and Roelof*, 2009) and was shown to be associated with this event (and with Event 1) by Cohen et al. (2017).

3.6.3 Event 3: 02 May 2014

Event 3 was a near-relativistic electron spike event observed on 2 May 2014. Both SEPT instruments on STEREO A and STEREO B observed nearly identical, symmetric spike events with a duration of less than 12 minutes. STEREO A observed the event at 05:33 UT and STEREO B observed the event at 5:32 UT.

Our ADAPT-WSA modeled 5 R_S footpoints ranged from 223° to 226° longitude for STEREO A, with a mean longitude of 225°, and from 266° to 275° longitude for STEREO B, with a mean longitude of 271°, as can be seen in Figure 3.8. These modeled footpoints are separated by 29° and 24°, respectively, from an associated solar flare observed by the STEREO EUVI instruments. STEREO A and STEREO B were modeled to be connected 33° and 14°, respectively, from the associated EUV

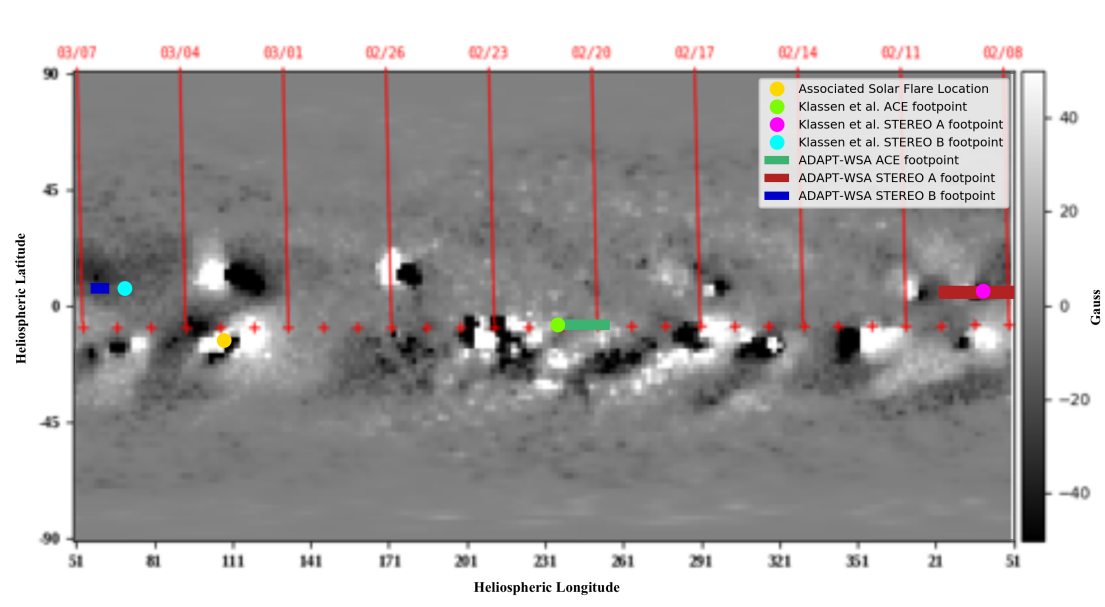

Figure 3.7: Map of SEP Event 2 ADAPT-WSA modeled 5 R_S footpoints and Klassen et al. 2.5 R_S footpoints (2016). These modeled PFSS footpoints are overlaid on a photospheric synoptic magnetic field map from ground-based GONG magnetograms. Coordinates are in heliospheric latitude and Carrington longitude. The solar equator is at 0° latitude and the Earth ecliptic plane is marked by red plus symbols. Vertical red lines mark the central meridians, labeled with the corresponding observational dates, of the GONG magnetograms that form the composite synoptic map.

jet, and connected 25°-38° and 8°-21°, respectively, from observed EUVI coronal loops. Altogether, this modeled connectivity supports why both spacecraft observed the electron event within a minute of each other and with such similar intensity profiles. Following the initial spike event, the decay phase electron intensity observed at STEREO B was greater than at STEREO A (*Klassen et al.*, 2015), which is consistent with STEREO B being ∼5° more closely connected to the flare and ∼19° closer to the EUV jet.

When Klassen et al. used the Parker spiral approximation to evaluate the STEREO A and B connectivity they approximated 2.5 R_S footpoints at 253° longitude for STEREO A and 300° longitude for STEREO B (2015). These footpoints would suggest that STEREO B was connected much further from the observed EUV jet, 37°-50°, and the solar flare source location, 51°, than STEREO A with separations of 3°-10° and 14°, respectively. Klassen et al. hypothesized that there might be a strongly non-radial field below their 2.5 R_S PFSS given that the Parker spiral approximation suggested that STEREO A should have a smaller angular separation from the flare location than STEREO B and yet STEREO B in fact observed the event onset at 05:32 UT only a minute earlier than STEREO A.

ADAPT-WSA indicated that the photospheric footpoint of STEREO B was actually 11° closer to the flare location than STEREO A, supporting the fact that STEREO B observed the SEPs first. The sub-PFSS magnetic field lines do seem to expand non-radially in the WSA modeling results as can seen by comparing the 5 R_S PFSS footpoints which can be seen in Figure 3.8 with the photospheric footpoints as shown in Figure 3.3, which shows that a large range of longitudes are magnetically connected to the flaring active region responsible for the SEP event, which helps explain why STEREO A observed the SEP onset at 05:33 UT only a minute after STEREO B.

Taken together, the ADAPT-WSA modeled field line footpoints better explain

the onset times of the STEREO observations, since STEREO B observed the onset of the SEP event just a minute before STEREO A, as opposed to the Parker spiral approximated footpoints which suggested STEREO A was significantly more closely connected to the source region.

Wiedenbeck et al. (2015) determined this event to be scatter-free, in which minimal interplanetary scattering occurred. We find the anisotropic nature of this event, as additionally noted by Klassen et al. (2015), supports the conjecture that the longitudinal spread of this SEP event and the acceleration of its near-relativistic electrons occurred near the corona rather than during interplanetary propagation.

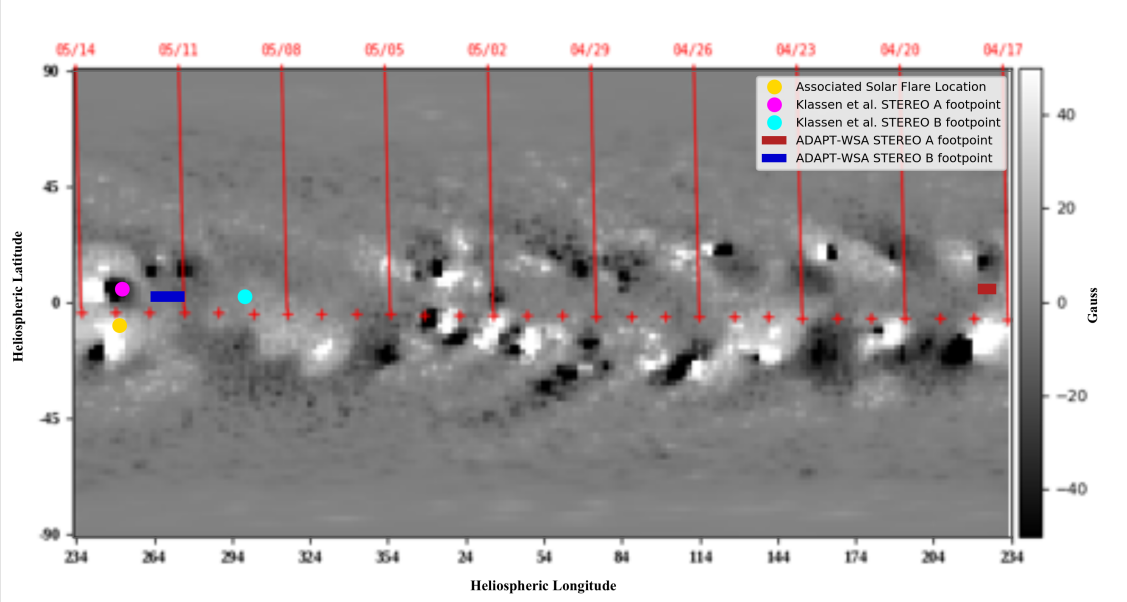

Figure 3.8: Map of SEP Event 3 ADAPT-WSA modeled 5 R_S footpoints and Klassen et al. 2.5 R_S footpoints (2015). These modeled PFSS footpoints are overlaid on a photospheric synoptic magnetic field map from ground-based GONG magnetograms. Coordinates are in heliospheric latitude and Carrington longitude. The solar equator is at 0° latitude and the Earth ecliptic plane is marked by red plus symbols. Vertical red lines mark the central meridians, labeled with the corresponding observational dates, of the GONG magnetograms that form the composite synoptic map.

3.6.4 Event 4: 17 July 2014

STEREO A observed a series of 10 impulsive electron events July 17th - 21st associated with recurrent flares from an active region (AR), while STEREO B only saw the first event on July 17th (*Klassen et al.*, 2018). At this time the orbital separation of the two spacecraft was 34°. Event 4 of this study, is that first electron spike event observed by both spacecraft on 17 July 2014. SEPT on STEREO A observed the electron onset at 08:42 UT, while SEPT on STEREO B observed the onset at 08:34 UT. The near-relativistic electron event was an anisotropic pulse event as seen in SEPT observations at STEREO A and STEREO B. The time profiles observed by the SEPT instruments on both spacecraft have nearly identical onset intensities, with the STEREO B profile dropping off in intensity more quickly than STEREO A, which then observed additional subsequent electron events over the next four days. The event originated from a region at (270,-10) on the border of a coronal hole with an EUV solar flare observed 08:07 UT - 08:09 UT, and an EUV jet observed at 08:11 UT by the STEREO EUVI instruments. This electron event was also associated with type III radio bursts observed between 08:08 UT to 08:16 UT by the SWAVES instruments on both STEREO spacecraft.

Our ADAPT-WSA modeling yielded 5 R_S PFSS footpoints ranging from 329° to 341° longitude for STEREO A, with a mean longitude of 334°, and from 1° to 3° longitude for STEREO B, with a mean longitude of 2°, as can be seen in Figure 3.9. These modeled footpoints are separated by 64° and 92°, respectively, from the flaring source region.

The Parker spiral approximated footpoints for STEREO A at the time of the SEP onset were at 338° longitude, and at 0° longitude for STEREO B (*Klassen et al.*, 2018). This would have STEREO A connected 68° from the flaring region and STEREO B connected 90° from the flaring region.

When one additionally considers the ADAPT-WSA modeled photospheric foot-

points for STEREO A and B, 273° and 42° respectively, as seen in Figure 3.3, we find that STEREO A is modeled to be directly connected to the flaring region on the photosphere, whereas STEREO B is more distantly connected with a 132° separation. It is worth noting here that the number of STEREO B footpoints extracted from the optimal realizations for this event numbered only three, which was much fewer than for any of the other modeled events, each of which numbered between 13 and 99 footpoints per spacecraft. This means the range of possible footpoint connections for STEREO B was reduced for this set of modeling runs. The modeled individual footpoint results for this event, and for each of the other 5 events, can be found in Appendix A.

The ADAPT-WSA modeling between the photosphere and the 5 R_S PFSS for this event does indicate a strongly non-radial field due to the coronal hole boundary. The source region is modeled to be connected to a huge swath of longitudes. This suggests that the near-corona longitudinal spread of the first electron pulse event was large, explaining why it was so well observed by both STEREO, and supports why STEREO A was able to observe that first electron pulse event 8 minutes earlier and then observed so clearly each of the 9 subsequent electron spike events associated with the recurring EUV flares observed July 17th to 21st, 2014.

Bučík et al. (2018) studied this near-relativistic electron event and found it to be an intense ^{3}He- and Fe-rich event, with scatter-free interplanetary propagation, and associated with a helical blowout jet. The broad curtain-like nature of a helical blowout jet supports our hypothesis that this event experienced significant near-corona longitudinal spreading.

In this case, the two methods of determining magnetic connectivity find similar results at the PFSS, with ADAPT-WSA modeling STEREO A closer by 4°, and STEREO B further by 2° from the source region than the Parker spiral approximation. Both methods suggest closer connectivity for STEREO A than STEREO B,

despite the fact that the initial electron intensity profiles observed by STEREO A and B on July 17th are quite similar (*Klassen et al.*, 2018). ADAPT-WSA modeling indicates that the sub-PFSS magnetic field is strongly non-radial due to the coronal hole boundary at the location of the flaring source region, indicating that this near-relativistic pulse event, while more closely connected to STEREO A, experienced near-corona longitudinal spreading which enabled it to be seen by both STEREO spacecraft.

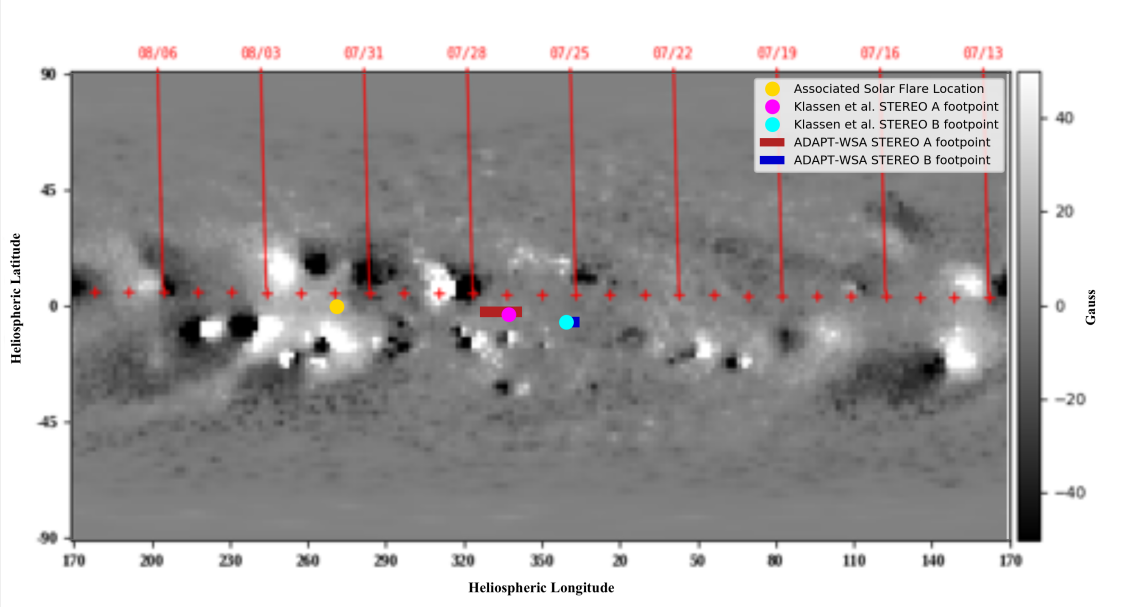

Figure 3.9: Map of SEP Event 4 ADAPT-WSA modeled 5 R_S footpoints and Klassen et al. 2.5 R_S footpoints (2018). These modeled PFSS footpoints are overlaid on a photospheric synoptic magnetic field map from ground-based GONG magnetograms. Coordinates are in heliospheric latitude and Carrington longitude. The solar equator is at 0° latitude and the Earth ecliptic plane is marked by red plus symbols. Vertical red lines mark the central meridians, labeled with the corresponding observational dates, of the GONG magnetograms that form the composite synoptic map.

3.6.5 Events 5 and 6: 01 August 2014

Events 5 and 6 were both observed on 1 August 2014. Event 5 was a near-relativistic electron pulse event observed at STEREO A at 16:34 UT and at STEREO

B at 16:54 UT. Event 6 was observed seven hours later at STEREO A at 23:45 UT and at STEREO B at 23:54 UT. Both events were associated with EUV solar flares and long, narrow EUV jets originating at (155,-22) as observed by the STEREO EUVI instruments, and type III radio bursts at 16:22 UT as observed by the ground-based CALLISTO network and 23:24 UT as observed by the SWAVES instruments. STEREO A observed both Event 5 and 6 with an earlier onset, a higher intensity and a more anisotropic time profile than STEREO B (*Klassen et al.*, 2016). While both events were electron pulse events, the SEPT electron time profiles for both events were observed to be less impulsive at STEREO B.

Our ADAPT-WSA modeling for Event 5 at a 5 R_S PFSS yielded footpoints ranging from 105° to 110° longitude, with a mean longitude of 107° for STEREO A, and ranging from 155° to 162° longitude, with a mean longitude of 154° for STEREO B. The ADAPT-WSA modeled footpoints for the ACE or SOHO spacecraft ranged from 301° to 321° longitude with a mean longitude of 308°. ADAPT-WSA models the STEREO A mean 5 R_S footpoint as 51° east of the EUV flare and jet source region, the mean STEREO B 5 R_S footpoint 16° north of the source region, and the mean ACE/SOHO R_S footpoint 156° west of the source region. These footpoint locations are shown overlaid on a synoptic magnetic field map in Figure 3.10.

Our ADAPT-WSA modeling for Event 6 yielded 5 R_S PFSS footpoints ranging from 102° to 107° longitude for STEREO A, with a mean longitude of 105°, and from 141° to 166° longitude for STEREO B, with a mean longitude of 154°, as can be seen in Figure 3.9. The ADAPT-WSA modeled footpoints for the ACE or SOHO spacecraft ranged from 319° to 347° longitude with a mean longitude of 331°. ADAPT-WSA models the STEREO A mean 5 R_S footpoint as 37° southeast of the EUV flare and jet source location, and the mean STEREO B 5 R_S footpoint 15° north of the source region, and the mean ACE/SOHO R_S footpoint 178° west of the source region. These footpoint locations are shown overlaid on a synoptic magnetic field map in Figure 3.11.

Klassen et al. approximated the Parker spiral footpoints for Event 5 to be at 133° longitude for STEREO A and at 143° longitude for STEREO B (*Klassen et al.*, 2016). The Parker spiral approximated footpoints for Event 6 were located at 133° longitude for STEREO A and at 137° longitude for STEREO B. These footpoints suggested STEREO A separations of 28° and STEREO B separations of 19° from the EUV flare and jet source location for Event 5, and similarly suggested a STEREO A separation of 28° and a STEREO B separation of 24° from the source location for Event 6.

Klassen et al. noted that STEREO A and B ought to be located near a coronal hole which was responsible for a series of high speed streams observed by STEREO B from July 31st - August 3rd overlapping with Event 5 and 6 SEP observations, and by STEREO A beginning late August 2nd (*Klassen et al.*, 2016). Yet, the Parker spiral PFSS footpoints are located further north than the coronal hole which produced these observed high speed solar wind streams. It is not until one includes the ADAPT-WSA modeling between the photosphere and the 5 R_S PFSS that one can see how well-connected STEREO B was to the coronal hole region, explaining the solar wind observations. The ADAPT-WSA modeled 5 R_S PFSS was widely connected to a range of photospheric longitudes. The mean ADAPT-WSA photospheric footpoints for STEREO A were located 36° southeast of the source location for Event 5 and 37° southeast of the source location for Event 6. Whereas, the ADAPT-WSA photospheric footpoints for STEREO B were on average 35° southwest of the source location for Event 5 and were modeled to two clusters of photospheric footpoint locations for Event 6, one located 9° northeast of the source location, and the other located 38° southwest of the source location. These ADAPT-WSA photospheric footpoints for STEREO B for both events falls right on the edge of the coronal hole boundary responsible for the high speed solar wind streams observed by STEREO B July 31st - August 3rd.

Event 5 was observed by STEREO A 20 minutes earlier than STEREO B and Event 6 was observed by STEREO A 9 minutes before STEREO B. STEREO A observed both events with SEPT intensity profiles with higher onset intensities which were more impulsive and closer to spike events. STEREO A ADAPT-WSA modeled PFSS footpoints were 35° further from the source location than STEREO B for Event 5, and STEREO A ADAPT-WSA footpoints were 22° further from the source location than STEREO B for Event 6. Similarly, the Parker spiral approximated STEREO A footpoints were 9° further from the source region than STEREO B for Event 5 and Parker spiral STEREO A footpoints were 4° further from the source region than STEREO B for Event 6. Both ADAPT-WSA modeled PFSS footpoints and Parker spiral approximated footpoints suggest that STEREO A should be less connected to the source region, yet STEREO A observed both events earlier and with stonger intensities. ADAPT-WSA magnetic field modeling sub-PFSS does support the explanation that non-radial fields allowed both spacecraft to be connected enough to see the events clearly, yet like the Parker spiral approximated footpoints, the ADAPT-WSA 5 R_S PFSS footpoints do not explain why STEREO A observed the events first. Further investigation into the impacts of the co-rotating interaction regions and high speed streams on the IMF line length for this event using ADAPT-WSA might shed light on this question.

3.7 Conclusions

As was discussed in Section 3.4, these six near-relativistic electron SEP events were all observed by both STEREO A and STEREO B when the spatial distance between the two spacecraft ranged from 32° to 72°. For these six events we have evaluated the impact of considering ADAPT-WSA modeled HMF lines to estimate near-relativistic electron propagation through interplanetary space as opposed to relying on the Parker spiral approximation. Our main findings are as follows:

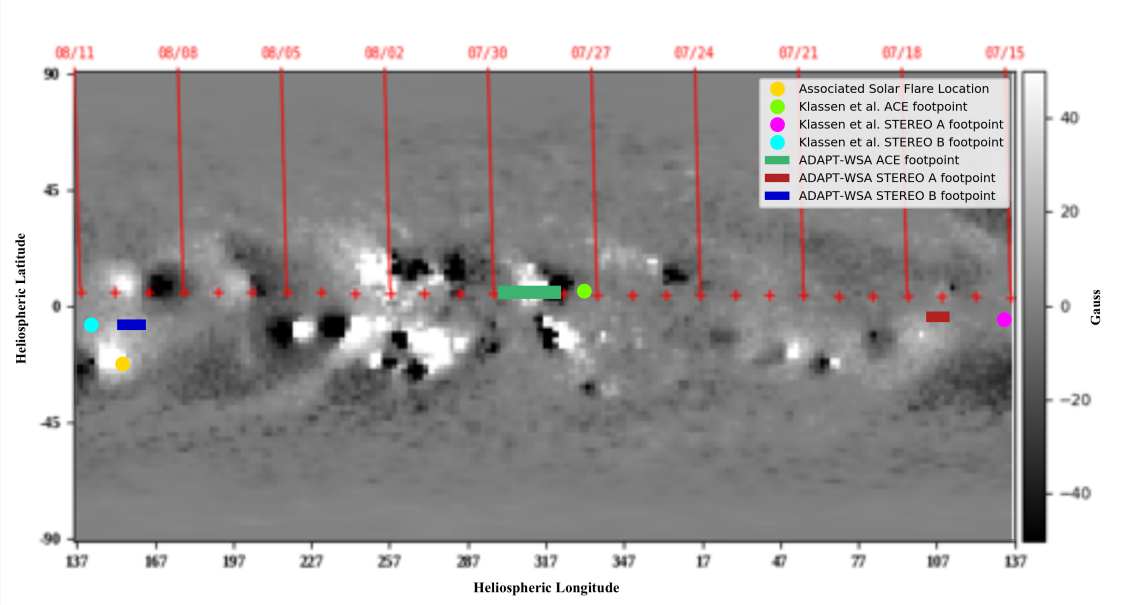

Figure 3.10: Map of SEP Event 5 ADAPT-WSA modeled 5 R_S footpoints and Klassen et al. 2.5 R_S footpoints (2016). These modeled PFSS footpoints are overlaid on a photospheric synoptic magnetic field map from ground-based GONG magnetograms. Coordinates are in heliospheric latitude and Carrington longitude. The solar equator is at 0° latitude and the Earth ecliptic plane is marked by red plus symbols. Vertical red lines mark the central meridians, labeled with the corresponding observational dates, of the GONG magnetograms that form the composite synoptic map.

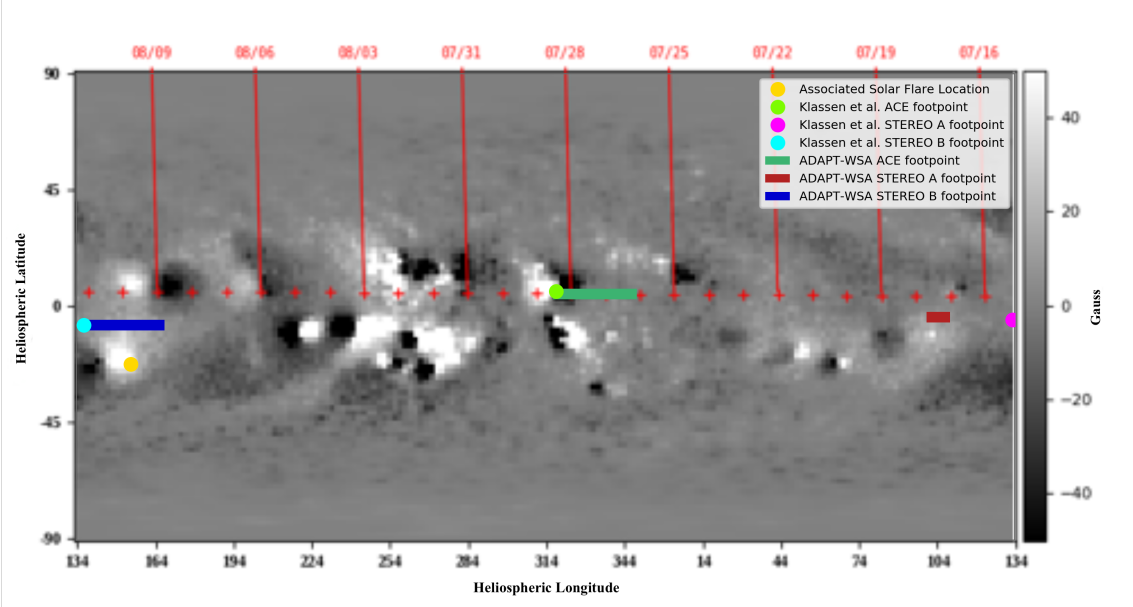

Figure 3.11: Map of SEP Event 6 ADAPT-WSA modeled 5 R_S footpoints and Klassen et al. 2.5 R_S footpoints (2016). These modeled PFSS footpoints are overlaid on a photospheric synoptic magnetic field map from ground-based GONG magnetograms. Coordinates are in heliospheric latitude and Carrington longitude. The solar equator is at 0° latitude and the Earth ecliptic plane is marked by red plus symbols. Vertical red lines mark the central meridians, labeled with the corresponding observational dates, of the GONG magnetograms that form the composite synoptic map.

- Events 1 and 2 were both near-relativistic ramp events associated with full-halo CMEs and expected to be impacted by interplanetary shock acceleration. ADAPT-WSA modeling fell short of explaining the discrepancies in connectivity and onset times and intensities. We suggest that our ADAPT-WSA modeling was unable to improve upon the Parker spiral approximation for these events due to the propagation effects due to interplanetary shock acceleration and distortions to the IMF caused by the associated full-halo CME, which we did not include in our ADAPT-WSA modeling. The additional impacts of these more complex magnetic field lines which were likely impacted by the propagating full-halo CME made any improvements due to ADAPT-WSA modeling less pronounced. Interplanetary shock acceleration as is known to be associated with near-relativistic ramp events (*Haggerty and Roelof*, 2009) and was shown to be associated with both of these events by Cohen et al. (2017).

- Event 3, observed on 02 May 2014, was a scatter-free electron spike event for which our modeled footpoints using ADAPT-WSA offered better agreement with observed onset times and intensity profiles at STEREO A and B than the Parker spiral approximated footpoints from Klassen et al. (2015).

- Event 4 was a scatter-free electron pulse event observed on 17 July 2014. ADAPT-WSA modeling indicates that the sub-PFSS magnetic field is strongly non-radial due to the coronal hole boundary at the location of the associated flaring source region, indicating that this near-relativistic pulse event, while more closely connected to STEREO A, experienced near-corona longitudinal spreading which enabled it to be seen by both STEREO spacecraft.

- Events 5 and 6 were two near-relativistic electron pulse events observed on 01 August 2014. ADAPT-WSA modeling for these events between the photosphere and the 5 R_S PFSS suggests that STEREO B was well-connected to the southern

coronal hole region, explaining observations of high speed solar wind streams at STEREO B from July 31st - August 3rd, which was not explained by 2.5 R_S PFSS footpoint locations approximated using the Parker spiral (*Klassen et al.*, 2016).

- Events 3 - 6 were near-relativistic electron spike or pulse events which were scatter-free as they propagated through interplanetary space, without SEP or CME interactions, enabling clearer analysis of the connectivity differences between ADAPT-WSA modeling and Parker spiral approximation. For each of these events, ADAPT-WSA modeling appeared to support improved onset time and intensity profile analysis compared to Parker spiral connectivity.

- Because Events 3 - 6 of this study were specifically during times where interactions from coronal mass ejections and previous SEP events are minimal, a future comparison between these events presented here and additional events which travel along more complex magnetic field topologies or with missing observational data, may help indicate how SEP propagation is impacted by the magnetic topology of the inner heliosphere.

Altogether, this analysis suggests that the impact of modeling near-relativistic electron SEP events using ADAPT-WSA as opposed to using the Parker spiral approximation does help improve the full picture of acceleration and connectivity for electron spike and pulse events, as was the case for Events 3-6, whereas modeling using ADAPT-WSA has less of an impact on electron ramp events like Events 1 and 2, which are expected to be impacted by interplanetary shock-acceleration due to associated CME interactions which are not included in our ADAPT-WSA modeling.

CHAPTER IV

A Characterization of Counterstreaming Suprathermal Electrons and Their Correlation with Interplanetary Coronal Mass Ejections 1998 - 2011

4.1 Preface

The following chapter presents a study which quantitatively characterizes the occurrence of counterstreaming suprathermal electrons over a complete solar cycle using in situ observations from NASA's Advanced Composition Explorer satellite from 1998 - 2011. While counterstreaming suprathermal electrons are known to occur during ICMEs and are expected to indicate closed magnetic field connections, this is the first study to actually quantitatively characterize the occurrence rate of counterstreaming and strahl suprathermal electrons of varying widths for both ICME and solar wind observations over a multi-year study that spans a complete solar cycle.

4.2 Abstract

Counterstreaming suprathermal electrons (CSEs) are widely regarded to be a signature of closed heliospheric magnetic field lines associated with interplanetary

coronal mass ejections (ICMEs). Thorough investigation indicates that CSEs are not always continuously or consistently observed in ICMEs (*Anderson et al.*, 2012). We present a statistical study quantitatively classifying CSEs and strahl suprathermal electrons (SSEs) and their occurrence with relation to ICMEs. This study is a multi-event study spanning 1998-2011 using observational data from the Solar Wind Electron, Proton, Alpha Monitor (SWEPAM), the Solar Wind Ion Composition Spectrometer (SWICS), and the Magnetic Field Experiment (MAG) onboard the Advanced Composition Explorer (ACE) located at the Lagrange point between the Earth and the Sun (L1). We present the occurrence rate analysis and preliminary discussion of expected suprathermal electron (SE) pitch angle distributions (PADs) for the inner heliosphere based on these multi-year observations.

4.3 Introduction

Suprathermal electrons are the population of electrons in the solar wind which have energies about 70 eV and above, which extend beyond the Maxwellian population of thermal electrons (*Vocks et al.*, 2005). Suprathermal electrons propagate through the inner heliosphere in gyrating paths around magnetic field lines. The angles that these gyrating paths form with magnetic field lines are known as pitch angles. By studying these pitch angles, one can glean certain information about the topology of the magnetic field lines (*Gosling and McComas*, 1987). The observed pitch angle distributions (PADs) of those suprathermal electrons observed in situ in the solar wind at L1 are affected by the topology of the field line to which they are bound, the strength of the magnetic field, and processes that cause scattering as they propagate through the inner heliosphere (e.g., *Feldman et al.*, 1975; *Gosling et al.*, 1987; *Pilipp et al.*, 1987a,b; *Gary and Li*, 2000; *Steinberg et al.*, 2005; *Pagel et al.*, 2007).

Beams of suprathermal electrons which are field-aligned with pitch angles near 0°, or anti-aligned with pitch angles near 180°, are known as suprathermal electron strahl.

We define those PADs of suprathermal electrons which are characterized by beams of unidirectional strahl, as strahl suprathermal electron (SSE) PADs. The width of the strahl is the spread of the pitch angles about 0° or 180°. Magnetic field lines which are closed, meaning both of their footpoints are connected to the Sun, have sources of electrons at each end and are therefore expected to have counterstreaming suprathermal electrons (CSEs), meaning suprathermal electrons are traveling both directions along the field line, with pitch angles near 0° and near 180° (*Gosling et al.*, 1987).

The strength of the magnetic field, the scattering processes in the inner heliosphere and the magnetic topology of the field line all impact the shape of the suprathermal electron PAD. The magnetic field strength of the heliospheric magnetic field lines decrease as they propagate outward from the Sun causing the beam of pitch angles to narrow, decreasing the SSE width. This effect is a result of the first adiabatic invariant which states that $\sin(\alpha_1)^2/B_1 = \sin(\alpha_2)^2/B_2 = \text{constant}$. In this case, say α_1 is the pitch angle of an electron on a field line near the Sun and B_1 is its magnetic field strength, then at a later time that same electron is further along that field line, which now has a lower magnetic field strength B_2 due to the divergence of solar magnetic fields as they spread out into the heliosphere, thus the electron now necessarily has a narrower pitch angle, α_2. This process is known as adiabatic focusing. If adiabatic focusing were the only process at work on these suprathermal electrons, then the beam width of SSEs and CSEs would be less than 1° wide by 1 AU (*Anderson et al.*, 2012). However, adiabatic focusing is not the only process at work.

While adiabatic focusing works to narrow SSE and CSE PADs (*Rosenbauer et al.*, 1977), there are scattering processes in the solar wind, such as wave-particle interactions like whistler waves (*Gary and Li*, 2000) and Coulomb collisions (*Pagel et al.*, 2007), which cause the pitch angles of deflected suprathermal electrons to spread, increasing the SSE and CSE width, causing the PAD to become more isotropic (*Pagel*

et al., 2007; *Vocks et al.*, 2016). The features of the HMF field lines along which SEs propagate also impacts the SE beam width. Kinks in field lines, magnetic reconnection and stream interaction regions can result in the focusing and scattering of SEs (*Feldman et al.*, 1982; *Steinberg et al.*, 2005).

The highly idealized case for how to interpret SE PADs is shown in Figure 4.1. This picture compares an idealized PAD plot of pitch angle versus time with suprathermal electron flux represented with the rainbow color bar. These idealized PADs map to particular magnetic field topologies, A, B, C or D. Ideally unidirectional beams of SEs are strahl and are either anti-aligned as with case A, or aligned as with case C with their magnetic field lines. A disconnected field line which has no source of SEs from the Sun would have no SE signature as seen with case D. Case B shows the CSE case when a closed magnetic field loop has solar sources of SEs along both magnetic footpoints and therefore has a very clear counterstreaming signature of two beams with electron flux along both 0° and 180°. While Figure 4.1 is wonderful at demonstrating the connection between SE PAD observations and corresponding magnetic field topology, it leaves off the more complicated cases. This standard set of cases does not address how to handle observations of isotropic fully-scattered PADs, how to interpret strongly asymmetric counterstreaming or how to identify broadened CSEs from 90° PAD depletions on open fields (*Gosling et al.*, 2001; *Skoug et al.*, 2006).

Previous investigations have used a broad range of beam widths for both SSEs and CSEs, from 5° to 60° whether using Helios-1 observations (*Rosenbauer et al.*, 1977; *Pilipp et al.*, 1987b) or using observations at 1 AU (e.g., *Feldman et al.*, 1982; *Fitzenreiter et al.*, 1998; *Ogilvie et al.*, 1999, 2000; *De Koning et al.*, 2006, 2007; *Pagel et al.*, 2007). The range of PAD widths that have been classified as narrow, as strahl and as SE beams, varies throughout past investigations, making comparison between these studies difficult. *Anderson et al.* ((2012)) began a quantitative approach to present-

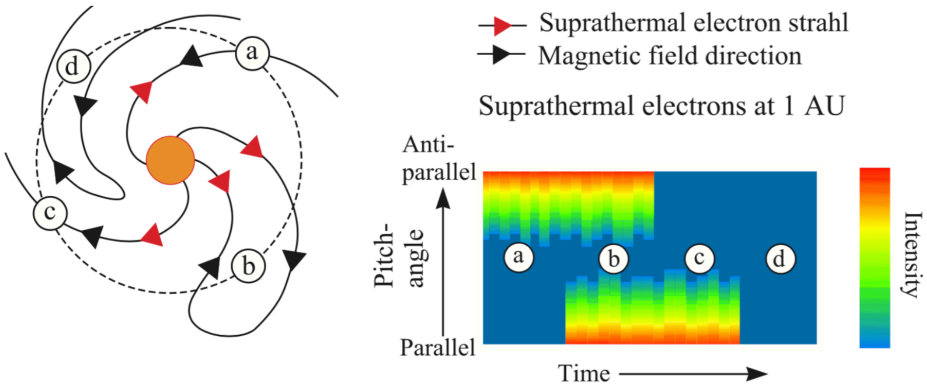

Figure 4.1: Diagram of heliospheric magnetic field lines and the corresponding idealized observations of suprathermal electron PADs. Region A & C: Open field lines with SSEs. Region B: Closed field lines with CSEs. Region D: Disconnected field lines with no suprathermal electron source (*Owens and Forsyth*, 2013).

ing the range of widths they observed from 1998 to 2002 using ACE SWEPAM PADs of SEs comparing observations during ICMEs with overall observations. Anderson et al. quantified the PADs of SSEs and CSEs using a Gaussian fit for the SE beam and a half-width half-maximum to characterize the beam width, and they used these to classify SEs into three types: unidirectional, counterstreaming and narrow ($< 20°$). We expand upon that initial work of *Anderson et al.* (2012) by covering a much more extended survey which spans 1998 to 2011. To better characterize SE PAD width observations and enable better characterization for comparison to other observational studies, this study seeks to quantitatively define not only a range of widths which could be defined as strahl, but to quantify the actual individual occurrence rates of various beam widths for both SSEs and CSEs during ICMEs and during non-ICME times.

CSEs have long been shown to be associated with interplanetary coronal mass ejections (ICMEs) (*Gosling*, 1990), while unidirectional SSEs have long been known to be associated with open magnetic field solar wind (*Rosenbauer et al.*, 1977). Streaming of both aligned and anti-aligned suprathermal electrons is theorized to occur along

closed magnetic fields which maintain footpoint connections at the Sun on both ends, which act as sources for the streaming SEs (*Gosling et al.*, 1987). While the idealized picture for case B of Figure 4.1 is oversimplified, these closed field topologies do occur along magnetic flux ropes which are observed in situ within ICMEs (e.g., *Gosling et al.*, 2001; *Skoug et al.*, 2000; *Zurbuchen and Richardson*, 2006; *Anderson et al.*, 2012).

Observations of coronal mass ejections (CMEs) indicate that the magnetic substructure of CMEs evolve as they propagate through the inner heliosphere (as explained in Section 1.2.2). When CMEs are observed near the Sun using coronagraphs, they typically have a three-part structure; flux-rope, cavity, and core (*Lepri and Zurbuchen*, 2010). Further out at 1 AU, this three-part structure is typically observed in situ. Understanding how the magnetic structure of ICMEs evolves and how magnetic topology relates to observed ICME properties is crucial in improving ICME modeling.

Additional topologies of magnetic structures can give rise to other PADs of suprathermal electrons. Reflection off magnetic obstacles such as planetary bow shocks or interplanetary shocks can cause bidirectional streaming (e.g., *Feldman et al.*, 1982; *Stansberry et al.*, 1988; *Gosling*, 1993; *Steinberg et al.*, 2005; *Skoug et al.*, 2006; *Owens and Forsyth*, 2013), which can be mis-characterized as CSEs despite their not being on a closed field structure, as can 90° PAD depletions (*Gosling et al.*, 2001; *Skoug et al.*, 2006). Yet these distinctions are not well-defined quantitatively. For instance, at what width or what background scattering level is an observation of broadened counterstreaming actually a 90° PAD depletion? Characterizing the expected PAD signatures on closed field magnetic structures, and distinguishing which features are unique to closed fields specifically gives a foundational basis to distinguish between each of these structures and will lead to the ability to more conclusively identify magnetic topology. The analysis in this study seeks to offer that quantitative definition to build upon with subsequent research.

This study seeks to quantitatively characterize the PADs of observed suprathermal electrons in the solar wind compared to those observed during ICMEs. This preliminary study uses suprathermal electron pitch angle observations by the ACE Solar Wind Electron, Proton, and Alpha Monitor (SWEPAM), which will be described in Section 4.4.1. The overall survey results are presented in Section 4.5. This observational survey gives an indication of the range of the widths of observed SSEs and CSEs and how those widths vary from observations during ICMEs compared to observations outside of ICMEs using two published ICME databases, which will be described in Section 4.4.1. The occurrence rates presented in Table 4.1 vary depending on what quantitative parameters for counterstreaming are used. This investigation produces cross-sections of the PADs so that quantitative thresholds such as those used for Table 4.1 or by *Anderson et al.* (2012) can be defined by quantitative features which can be compared across solar wind conditions, ICME substructure, and magnetic topologies. Thus these features of SE PADs, which are impacted by interplanetary propagation and magnetic topology, can be better studied in quantitative surveys with detailed investigation into their correlation with ICME properties such as magnetic flux ropes, filament plasma, heavy ion charge state distributions of Fe, C and O, plasma temperature, density and velocity.

4.4 Event Analysis

4.4.1 Observational Data

The data for this study were observed by the Advanced Composition Explorer (ACE). ACE was launched 25 August 1997 and has since been taking continuous data in orbit around the L1 point, between the Sun and the Earth. This study primarily uses observations from the Solar Wind Electron, Proton, and Alpha Monitor (SWEPAM) (*McComas et al.*, 1998) and the magnetic fields experiment (MAG)

(*Smith et al.*, 1998) on ACE beginning 1 January 1998 when science operations began.

SE pitch angles are observed by SWEPAM in 64 second time resolution and are compared with ACE MAG observations of the magnetic field direction to determine the PADs. Every 64 seconds the SWEPAM instrument sweeps from 0° to 180°, and bins each pitch angle into bins of 9° wide (*McComas et al.*, 1998). The MAG experiment on ACE provides continuous in situ observations of the local magnetic field (*Smith et al.*, 1998). Magnetic field alignment for the SE PADs is determined using these observations from the MAG instrument. This means the bin of pitch angles aligned with the magnetic field contains pitch angles 0° to 9°, and the next contains pitch angles 10° to 18°, and so on, through to the anti-aligned pitch angle bin of 171° to 180°. The SWICS instrument onboard ACE provides in situ ion charge state observational data, and observations of bulk proton velocity, density and temperature (*Gloeckler et al.*, 1998), which we additionally consider while discussing the substructure of individual ICME events in our Results and Discussion Section. The ACE observational data from SWEPAM, SWICS and MAG are available at the ACE Science Center (http://www.srl.caltech.edu/ACE/ASC/level2/index.html).

We used two published databases of ICME observations to evaluate whether our SE PAD observations were observed during ICMEs. One such ICME database uses observational data from SWEPAM, SWICS and MAG instruments onboard ACE to identify ICMEs from May 1996 to October 2011, referred to here as the C&R ICME List (*Cane and Richardson*, 2003; *Richardson*, 2004; *Richardson and Cane*, 2010) (available online at http://www.srl.caltech.edu/ACE/ASC/DATA/level3/icmetable2.html). The second ICME database spans February 1995 to December 2009 using observations from instruments on both Wind and ACE to identify ICMEs, referred to subsequently as the LJ et al. ICME List (*Jian et al.*, 2006, 2011). This study covered the overlap between the set of ACE SWEPAM observational data with that of the ICME databases. Thus the study spanned 1 January 1998 to 17 October 2011

when referencing the C&R ICME database, and covered the time span of 1 January 1998 to 31 December 2009 when referencing the LJ et al. ICME database.

4.4.2 Quantifying the Pitch Angle Distributions

We use the ACE SWEPAM observations of SEs described in Section 4.4.1 to quantify the PADs of SEs. A standard PAD plot compares the pitch angle versus time with suprathermal electron flux represented with a rainbow color bar. Examples of such PADs as observed by ACE SWEPAM are shown in the lower panels of Figures 4.2 and 4.3. A cross-section plot of these PAD panels therefore shows the SE flux versus pitch angle for one 64 second observational sweep. Such cross-section plots are given in the top panel of Figure 4.2 and the top four panels of Figure 4.3.

Figures 4.2 and 4.3 both display the PAD cross-section figures which show the complexity of qualitatively describing SE PADs. The top panel of Figure 4.2 presents the SE flux for 0° to 180° of observed SE pitch angles on 14 July 2008 at 04:48 UT. Given the singular unidirectional beam of field-anti-aligned SEs, this cross-section is an observation of SSEs. For example, the top four panels of Figure 4.3 represent the SE cross-section PADs for several observational times taken from the lowest panel. These top panels present the SE flux for 0° to 180° of observed SE pitch angles on 18 Aug 1998 at 12:30 UT, 20 Aug 1998 at 23:56 UT, 22 Aug 1998 at 02:22 UT and 20 Aug 1998 at 07:12 UT. The top-most panel shows an observation of a very narrow beam of SSEs observed in the solar wind ahead of the ICME observations. The second panel shows a broadened SSE beam with some background scattered SEs observed in the middle of the ICME. The third panel shows an observation of fully-scattered SEs, without distinct SSE or CSE beams. The fourth panel shows a clear CSE observation from during the ICME. This range of PAD types displayed across these example figures, while difficult to consistently differentiate qualitatively, lend well to a quantitative characterization based on observational features which can be

compared from one time to another, independent of color bar choice and without making assumptions about the definition of "narrow."

As explained in the Introduction, Section 4.3, we are characterizing the features of the observed SE PADs further than simply unidirectional SSE or bidirectional CSE. To quantitatively characterize the observed SE PADs, we use three primary parameters: 1) the flux at the half-maximum of the SE beam 2) the width at half-maximum of the SE beam and 3) the mean observed flux across each observation bin.

The first parameter is the half-maximum of the SE beam height in SE flux. The maximum beam height is determined as the maximum SE flux value of any pitch angle bin from 0° to 180° pitch angle bin.

The second parameter is the width at half-maximum. The width at half-maximum is the SE pitch angle beam width from 0° for the field-aligned beam or from 180° for the anti-field-aligned beam. This width at half-maximum is then the beam width to within the 9° pitch angle range. Given that the beam width shown in a 0° to 180° cross-section PAD plot is actually half the beam width in 360° pitch angle space, our width at half-maximum parameter value is equivalent to an SSE beam's half-width half-maximum in 360° space. In the case of CSE observations, the width at half-maximum is determined for each beam separately, while the same half-maximum is used across each PAD. Thus, the beam with lower flux, or the minor beam, must then be greater than the half-maximum of the major beam to be considered a CSE PAD. While this requirement creates a dependence between the two beams, it forces a minor beam to rise well above the mean flux to be classified as counterstreaming, preventing scattered pitch angles in a PAD with a high flux SSE beam from masquerading as a counterstreaming beam. The half-maxima are shown as horizontal purple lines in the cross-section panels of Figures 4.2 and 4.3.

The third parameter we use to quantify the SE PAD is the mean SE flux across

all pitch angles for each observational time bin. This parameter gives a quantitative value to the amount of overall SE flux in the PAD for a given observational sweep. Thus by comparing this value to the flux at the half-maximum, we can characterize the level of scattering or background halo SEs. This second parameter is depicted as a blue horizontal line in each of the cross-section PAD panels of Figures 4.2 and 4.3.

Using these three primary parameters, we created an algorithm that sweeps the full survey of ACE SWEPAM observations from 1998 to 2011 at the 64 second cadence of observations. For each time cadence our algorithm defines the quantitative parameters for each PAD observation while classifying the observation as occurring during an ICME or during a non-ICME time. If the 64 second SWEPAM time bin of the PAD observation contained the start time of the ICME according to the ICME list, then that time bin was classified as an ICME time. If an observation time bin extended past the end of the ICME according to the ICME list, it was classified as a non-ICME time. These two quantitative parameters are then used to classify the SSE PADs and CSE PADs by beam width and to identify periods of isotropic scattering. The particular PAD characterizations used in our algorithm and their occurrence rates within ICMEs are determined using both the C&R and LJ et al. ICME lists are presented in Section 4.5.

4.5 Results and Discussion

We present here the results of applying our quantitative scheme for characterizing SWEPAM SE PADs over a fourteen-year 64 second cadence survey from 1998 to 2011. This scheme not only enables identification of whether an SE PAD is counterstreaming or strahl, but also identifies characteristics of the observed PADs such as the beam width for SSEs and CSEs, a scattering index and a symmetry index. The occurrence rates of these metrics when compared to ICME and non-ICME observations are presented in Tables 4.1, 4.2 and 4.3.

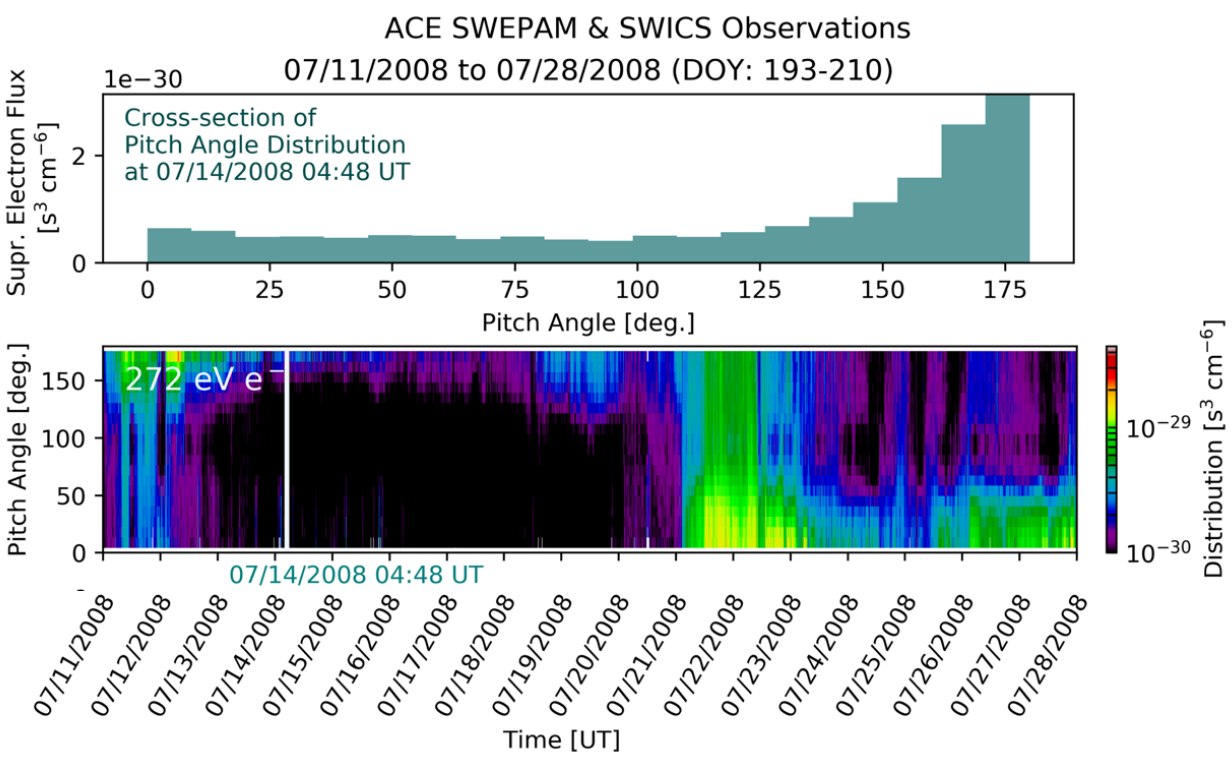

Figure 4.2: ACE SWEPAM observations of 272 eV SEs from 11 July 2008 to 28 July 2008. This period of solar wind observations does not contain an ICME. The lower panel plot shows the observed SE pitch angles versus time with the rainbow color bar representing the SE flux for each pitch angle bin. The vertical white line in the lower panel marks the location of the PAD cross-section shown in the panel above. This top panel presents the SE flux for 0° to 180° of observed SE pitch angles on 14 July 2008 at 04:48 UT. Given the singular unidirectional beam of field-anti-aligned SEs, this cross-section is an observation of SSEs.

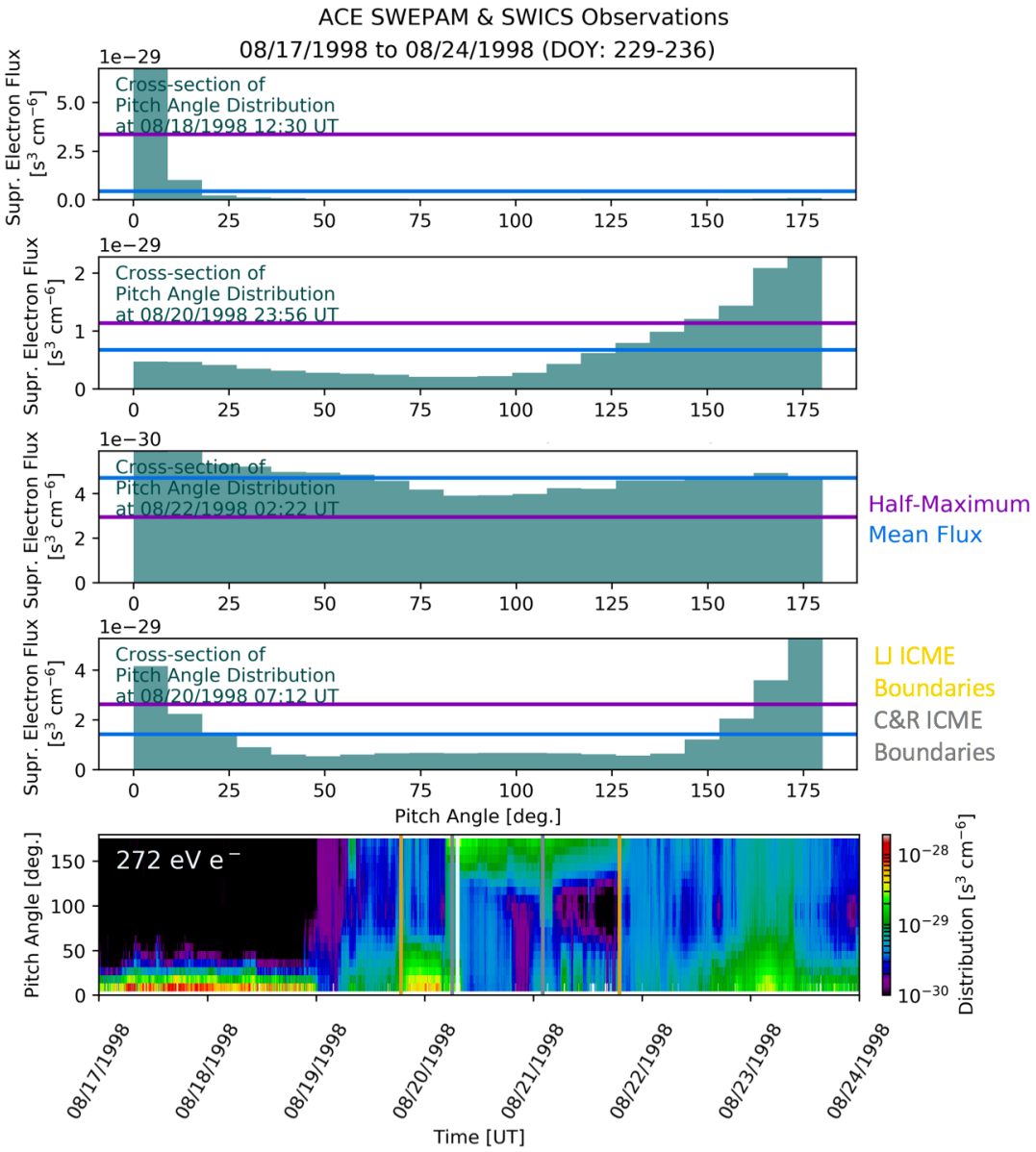

Figure 4.3: ACE SWEPAM observations of 272 eV SEs spanning a week from 17 Aug 1998 to 24 Aug 1998. This time period contains observations of an ICME with boundaries from the C&R ICME list in silver and the LJ et al. ICME list in gold. Panels 1-4 give the SE flux for 0° to 180° for several observational times taken from the lowest panel. Panel 1 shows a very narrow beam of SSEs observed in the solar wind ahead of the ICME observations on 18 Aug 1998 at 12:30 UT. Panel 2 shows a broadened SSE beam with some background scattered SEs observed in the middle of the ICME on 20 Aug 1998 at 23:56 UT. Panel 3 shows an observation of fully-scattered SEs, without distinct SSE or CSE beams on 22 Aug 1998 at 02:22 UT. Panel 4 shows a clear CSE observation from during the ICME on 20 Aug 1998 at 07:12 UT, which is marked by the vertical white line in panel 5. Panel 5 shows the observed SE pitch angles versus time with the rainbow color bar representing the SE flux for each pitch angle bin.

Table of Results: Survey of ICME Suprathermal Electron Strahl and Counterstreaming Occurrence Rates

PAD Type	Percent of C&R ICME Times with PAD Type	Percent of C&R non-ICME Times with PAD Type	Percent of LJ ICME Times with PAD Type	Percent of LJ non-ICME Times with PAD Type
CSE: ≤ 9° widths	0.140%	0.001%	0.126%	0.003%
CSE: ≤ 18° widths	1.418%	0.045%	1.351%	0.065%
CSE: ≤ 27° widths	2.756%	0.109%	2.549%	0.149%
CSE: ≤ 36° widths	4.122%	0.236%	3.606%	0.301%
CSE: ≤ 45° widths	5.121%	0.423%	4.557%	0.493%
CSE: ≤ 54° widths	6.047%	0.729%	5.511%	0.814%
SSE: ≤ 9° width	7.758%	3.640%	7.374%	4.188%
SSE: ≤ 18° width	13.254%	6.705%	13.060%	7.501%
SSE: ≤ 27° width	15.380%	8.119%	14.925%	9.023%
SSE: ≤ 36° width	16.582%	9.371%	16.059%	10.337%
SSE: ≤ 45° width	17.242%	10.448%	16.881%	11.437%
SSE: ≤ 54° width	17.638%	11.241%	17.316%	12.266%
SSE: ≤ 63° width	17.906%	11.656%	17.678%	12.699%
Scattered: Pitch Angles of 54° to 126° > 0.75 · Mean PAD Flux	1.719%	4.063%	2.719%	4.115%
Scattered: Scattering Index > 1	6.832%	14.085%	8.225%	14.045%

Table 4.1: Table of occurrence rates of various suprathermal electron PAD widths for SSE and CSE observations during times identified as ICMEs according to the C&R ICME database (*Richardson and Cane*, 2010) and the LJ et al. ICME database (*Jian et al.*, 2011). Observational data is from ACE SWEPAM from 1998 to 2011 for C&R and 1998 to 2009 for LJ. The widths presented here are the beam widths at half-maximums. Scattered PADs are identified using two metrics. One metric identifies a PAD as scattered when the fluxes of the pitch angles 54° to 126° are greater than 3/4 the mean PAD flux. The second metric is a scattering index, defined in Section 4.5 which is greater than 1 when the mean PAD flux is greater than the flux at the half-maximum.

Survey of ICME Suprathermal Electron Scattering Index Occurrence Rates

Scattering Index	Percent of C&R ICME Times	Percent of C&R non-ICME Times	Percent of LJ ICME Times	Percent of LJ non-ICME Times
$0.0 \leq I_{scatter} \leq 0.25$	10.9%	4.9%	10.7%	5.7%
$0.25 < I_{scatter} \leq 0.5$	28.2%	14.2%	28.4%	15.3%
$0.5 < I_{scatter} \leq 0.75$	24.9%	20.1%	23.1%	20.1%
$0.75 < I_{scatter} \leq 1.0$	18.2%	25.5%	18.3%	24.3%
$I_{scatter} > 1.0$	16.1%	33.9%	17.7%	33.0%

Table 4.2: Table of SE scattering index occurrence rates during times identified as ICMEs according to the C&R ICME list (*Richardson and Cane*, 2010) and the LJ et al. ICME list (*Jian et al.*, 2011). The scattering index is the ratio of the mean flux across all pitch angles to the flux at the half-maximum of the major SE beam. Note that the scattering index, $I_{scatter}$, is greater than 1 when the mean PAD flux is greater than the flux at the half-maximum of the major SE beam. When $I_{scatter}$ is near zero, then the half-maximum flux is much greater than the mean PAD flux, corresponding to a PAD with the majority of the SE flux in the SE beams.

As can be seen in Table 4.1 we use the aforementioned quantitative parameters to characterize the ACE SWEPAM SE PAD observations. We characterize SSE and CSE PADs by their widest beam width. For example, a PAD with a major SE beam width at half-maximum between 0° and 9° and a minor beam width between 10° and 18° would be classified as a CSE with $\leq 18°$ widths. Our algorithm then identifies whether the observation of this PAD were made at a time between the published start and end times of an ICME according to the C&R (*Richardson and Cane*, 2010) or LJ et al. (*Jian et al.*, 2011) ICME list. The results of the overall classification for each SSE or CSE PAD in the survey is shown in Table 4.1.

As presented in Table 4.1 and 4.2, we use a scattering index as a metric to characterize the magnitude of scattered halo SEs to the flux height of the SE beam for

Survey of ICME Suprathermal Electron Symmetry Index Occurrence Rates

Symmetry Index	Percent of C&R ICME Times	Percent of C&R non-ICME Times	Percent of LJ ICME Times	Percent of LJ non-ICME Times
$0.0 \leq I_{symmetry} \leq 0.25$	40.8%	34.2%	41.5%	36.3%
$0.25 < I_{symmetry} \leq 0.5$	27.6%	36.2%	26.7%	35.0%
$0.5 < I_{symmetry} \leq 0.75$	17.6%	19.3%	17.1%	18.7%
$0.75 < I_{symmetry} \leq 1.0$	12.3%	8.8%	12.9%	8.5%

Table 4.3: Table of SE symmetry index occurrence rates during times identified as ICMEs according to the C&R ICME list (*Richardson and Cane*, 2010) and the LJ et al. ICME list (*Jian et al.*, 2011). The symmetry index is the ratio of the flux at the half-maximum of the minor beam to the flux at the half-maximum of the major beam. The occurrence rates are sorted by 0.25 bins. Note that a symmetry index value of $I_{symmetry} = 1$ indicates a symmetric PAD. As $I_{symmetry}$ approaches zero, the PAD becomes more asymmetric.

each SE PAD. The scattering index is defined as the ratio of the mean flux across all pitch angles to the flux at the half-maximum of the major SE beam. We include in Table 4.1 in the second lowest row an additional metric for scattering, which identifies those PADs with SE flux in the 54° to 126° which exceed 3/4 the mean PAD flux as scattered PADs.

The use of the symmetry index, $I_{symmetry}$, presented in Table 4.3, enables characterization of the difference between the half-maxima of two CSE beams. We define this symmetry index simply as the ratio of the flux at the half-maximum of the minor beam to the flux at the half-maximum of the major beam. This means the symmetry index will be equal to 1 when the CSE beams are equal. By requiring minor beams to be greater than the half-maxima of the major beam, our algorithm necessarily requires $I_{symmetry} \geq 1/2$ to be classified as a CSE PAD.

The occurrence rates presented in Table 4.1 give expected widths for both SSEs and CSEs in ICME and non-ICME observations over a fourteen-year span which covers a complete solar cycle, which gives us a few results worthy of noting. We observe narrow CSEs at much higher rates during ICMEs; over 100 times more frequently for 9° or narrower than during non-ICME solar wind. Very narrow CSEs with SE beam widths ≤18° are nearly exclusively observed during ICMEs. More than 76% of ICME times are not actually classified as either CSE or SSE by our algorithm.

The results shown in Tables 4.5, 4.2 and 4.3 do lead to a few conclusions that can be drawn about suprathermal electrons in ICMEs compared to non-ICME solar wind. It does appear that PADs with narrow CSEs, narrow SSEs, lower scattering indices and lower symmetry indices occur more frequently within ICMEs than during non-ICME times. Fully scattered SE observations ($I_{scatter} > 1.0$) occur more than twice as frequently in non-ICME times. A higher percentage of SE observations during ICME times have low symmetry indices (0 to 1/4) and low scattering indices (0 to 1/4) than during non-ICME times. These observations are supported by the fact that ICMEs have lower plasma beta which results in reduced whistler wave interactions, which in turn reduces whistler mode scattering (*Gary and Li*, 2000). Thus SE PADs with narrower beams and less scattering should be expected within ICMEs.

We observe narrow CSEs at much higher rates during ICMEs, for example over 100 times more frequently for 9° or narrower than during non-ICME solar wind. While ICMEs do contain higher percentages of CSEs than non-ICME solar wind does, it is still clear from the results that more than 76% of ICME times are not CSEs. Since the magnetic flux rope of an ICME is a closed-loop expanding magnetic coil, we should expect that greater adiabatic focusing would occur and so we should expect higher percentages of narrower CSEs along the magnetic flux ropes. Magnetic flux ropes are only observed in 1/3-1/2 of ICMEs at 1 AU (*Gosling*, 1990). Even those ICMEs with observed flux ropes, the flux rope structure is not typically seen throughout the entire

ICME observation (*Richardson*, 2004). Still, the observation that more than 76% of ICME times are not CSEs should be expected. One of the more surprising conclusions we find, is the fact that SSEs are actually observed more frequently within ICMEs.

The quantitative description of SE PADs enables careful consideration of ICME case events which can be compared to the long-term survey of results. For example, consider an ICME event observed 08-10 September 2002. ACE observations of this ICME using SWEPAM, SWICS and MAG are shown in Figure 4.4. The boundaries of this ICME are in near agreement between both C&R and LJ et al. ICME databases, marked by silver and gold respectively. The top panel on the left shows the 272 eV SE cross-section PAD on September 10^{th} at 01:55 UT. This particular cross-section comes from the region marked with a white line on the second panel of the left set of observations. This second panel on the left is a typical PAD figure, ranging from 0° to 180° pitch angle up the y-axis and time on the x-axis, with the SE flux represented with a rainbow color bar.

One might notice the brief period of CSEs on 07 September 2002. This period is observed well before the ICME and likely indicates a stream interaction region, as it is accompanied by a jump in magnetic field magnitude, a velocity jump in the solar wind speed, a jump in temperature and enhancements in high charge state Carbon and Oxygen ions. This is a clear example of CSEs outside of an ICME. Characterization of the scattering index and SE beam for such CSEs in the solar wind may offer insights into the magnetic topology for such interesting observations.

As demonstrated with the top panel of Figure 4.4, there are certain cases of extremely asymmetric SE PADs where the minor beam is discounted by our algorithm since its half-maximum is below the mean flux value. How best to classify such cases might be up for debate. Are these two beams so asymmetric due to an extremely asymmetric closed field loop, where one footpoint might be much more distant than the other? Or are the beams so asymmetric, because this is actually a case of an

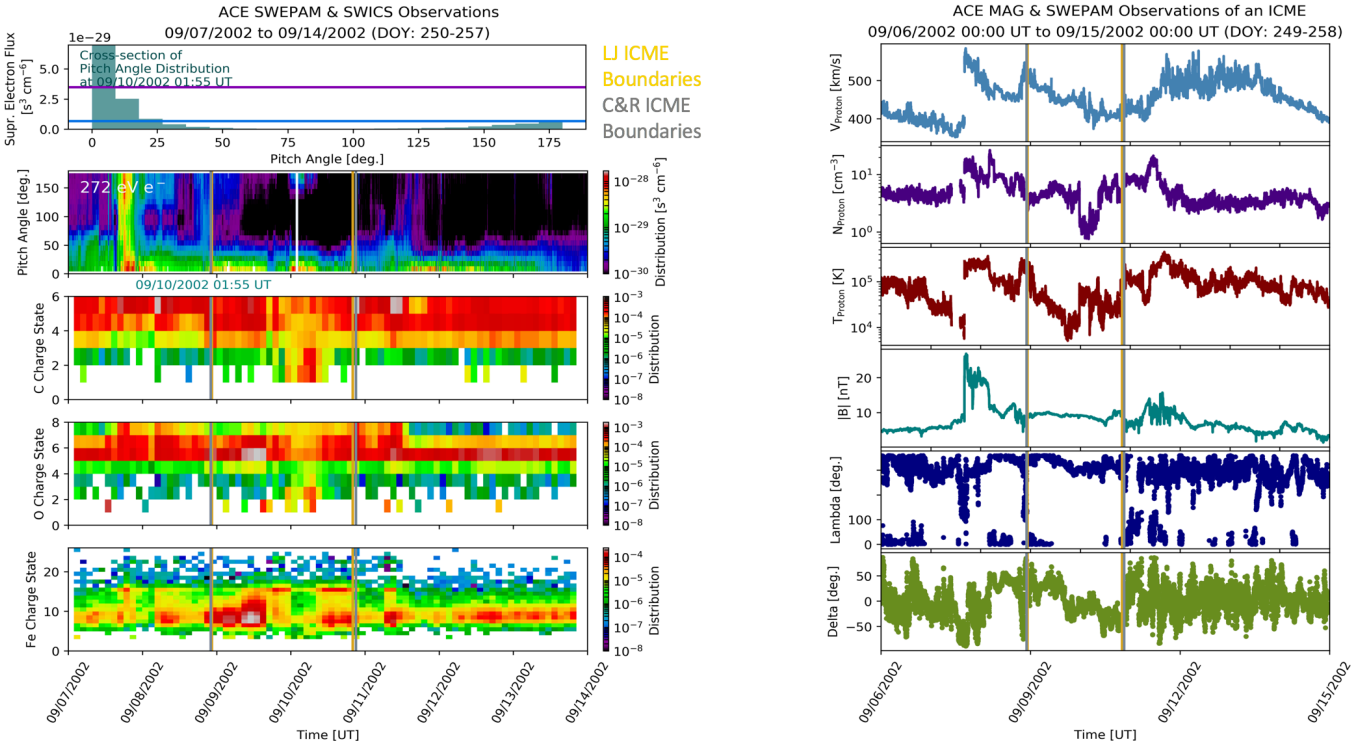

Figure 4.4: Solar wind observations spanning 07 September 2002 to 14 September 2002 using observations from SWEPAM, SWICS and MAG onboard ACE. The top two panels on the left show observed SE PADs from SWEPAM. The top panel presents the SE flux for 0° to 180° of observed SE pitch angles on 10 September 2002 at 01:55 UT. The second panel shows the observed SE pitch angles versus time with the rainbow color bar representing the SE flux for each pitch angle bin. The vertical white line in the second panel marks the location of the PAD cross-section shown in the panel above. The three lower panels on the left present charge state observations for Carbon, Oxygen, and Iron. The upper three panels on the right present proton observations from SWEPAM indicating the bulk solar wind velocity, density and temperature. The lower three panels on the right show magnetic field observations from MAG of the magnetic field magnitude and the lambda and delta magnetic field components.

SSE PAD where a small portion of the beam is reflected some distance ahead of the observation location? Or is the asymmetry due to differences in the initial electron population of the source region at the Sun? Low PAD symmetry could perhaps be caused by differing conditions of interplanetary propagation which resulted in more scattering and electron loss to one beam than the other. The classification algorithm used here interprets an observation such as that seen in the first panel of Figure 4.4 as an SSE PAD. Perhaps in subsequent work, a constant background scattering value might be considered rather than the mean flux, which for highly asymmetric beams would then classify this case as an asymmetric CSE PAD instead. Discussion of such observations with low symmetry is greatly assisted using a quantitative characterization of the symmetry, such as is possible using a symmetry index. This index also enables further study of how the asymmetry relates to the magnetic topology and the occurrence of these observations in various conditions, such as ICME or non-ICME as is presented in Table 4.3.

Anderson et al. (2012) also conducted a study to characterize and define SE PADs. Their study used ACE SWEPAM observations from 1998 to 2002. They used a Gaussian fit to determine the SSE or CSE beam width along with a constant term to define an isotropic constant background halo. Their Gaussian fit was calculated about their observations mirrored about 0° or 180°, and used the fitted half-width half-maximum to define the SE beam width. Thus their beam width is the fitted equivalent to our width at half-maximum parameter. From their survey of observations and curve fit, *Anderson et al.* created a single definition evaluating what a CSE ought to be. Their definition allowed for beam widths ranging from 4° to 90°, required a monotonic decrease from 0° to 90° or from 180° to 90°, and required that the 0° to 45° SE flux (or 135° to 180°) be more than twice the mean flux of the central pitch angles from 45° to 90° (or 90° to 135°) or another metric that likewise required the flux for the central pitch angles to be some fraction below the flux of the SE beam.

A histogram showing their calculated beam widths for SEs of 272 eV for CSEs (blue) and SSEs (red) as a fraction of observations can be seen in Figure 4.5. A table of their occurrence rates during C&R ICMEs and during LJ et al. ICMEs is shown in Table 4.4. They define an SE beam width as narrow when the width is less than 20°.

When we compare the occurrence rates found using our algorithm, shown in Table 4.1, with those of *Anderson et al.* (2012) shown in Table 4.4, we find that the occurrence rates between the two characterization algorithms differ significantly. Across the board, the occurrence rates are much lower using our algorithm than those calculated by *Anderson et al.*. When the *Anderson et al.* results for unidirectional narrow SSE beams, which they define as $\leq 20°$ widths, are compared with our results for the SSE PADs with widths $\leq 18°$, they find 15% overall, 15% during C&R ICMEs, and 16% during LJ et al. ICMEs, whereas we find 6.7% during C&R non-ICME wind, 13.3 % during C&R ICMEs, 7.5% during LJ et al. non-ICME wind, and 13.1% during LJ et al. ICMEs. Some of the difference might lie in the fact that our study spanned an entire solar cycle whereas the *Anderson et al.* survey only spanned 4 years, from 1998 to 2002, during the rising phase of the solar cycle. Alternatively, some difference might lie in the method of calculating the half-width half-maximum. We used bins that matched the 9° pitch angle bins of the observations, whereas *Anderson et al.* used a Gaussian fit with a constant suprathermal halo term, which effectively interpolated widths narrower than the precision of the pitch angle observations. For the case of counterstreaming PADs, our algorithm classifies the PAD collectively, so the wider beam determines the width classification of the PAD, whereas *Anderson et al.* classified each beam width separately.

4.6 Conclusions

We produce a quantitative characterization scheme of SE PADs which uses three primary parameters to analyze ACE SWEPAM PAD observations. This scheme en-

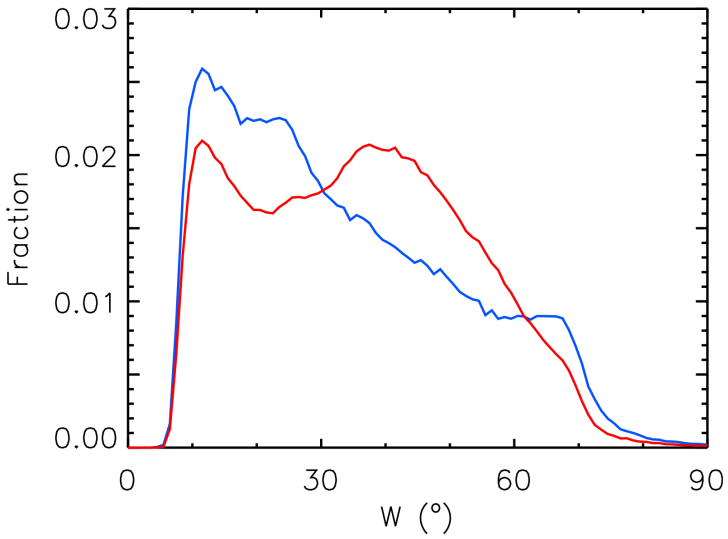

Figure 4.5: Histogram of SE beam width occurrence rates from (*Anderson et al.*, 2012). This study was conducted using ACE SWEPAM observations from 1998 to 2002 of 272 eV SE PADs. Anderson et al. identified SE beams using criteria discussed in Section 4.5. SE PADs were categorized as counterstreaming (blue) whenever SE beams were identified in both directions, and unidirectional (red) whenever only one SE beam was identified.

Counterstreaming and Narrow Strahls in General and ICME Solar Wind[a]

	1998–2002	CR-03	J-06
Narrow strahl present	20%	35%	33%
Unidirectional	64%	51%	54%
Counterstreaming	10%	35%	29%
Unidirectional and narrow	15%	15%	16%
Counterstreaming and narrow	5%	21%	16%
Portion of unidirectional that are narrow	23%	29%	30%
Portion of counterstreaming that are narrow	53%	60%	55%

[a]All results 272 eV. CR-03, *Cane and Richardson* [2003]; J-06, *Jian et al.* [2006].

Table 4.4: Table of results from *Anderson et al.* (2012). This study was conducted using ACE SWEPAM observations from 1998 to 2002 of 272 eV SE PADs. Occurrence rates were compared with C&R (*Cane and Richardson*, 2003) and LJ et al. (*Jian et al.*, 2006) ICME lists, labeled CR-03 and J-06 respectively. Narrow SE beams were classified as those with beam widths $< 20°$. Anderson et al. identified SE beams using criteria discussed in Section 4.5. Any SE PAD containing an SE beam was categorized as "strahl present." SE PADs were categorized as counterstreaming whenever SE beams were identified in both directions, and unidirectional whenever only one SE beam was identified.

ables characterization of the width of SSEs and CSEs, the background scattering and the PAD symmetry. This quantitative characterization enables direct comparison of SE observations over a large survey and in various conditions, such as ICME or non-ICME times. By characterizing these CSE and SSE observations over a fourteen-year survey and determining occurrence rates of varying SE beam widths during both ICMEs and non-ICME solar wind times according to published ICME lists *Richardson and Cane* (2010); *Jian et al.* (2011), we find several observations worthy of noting:

1. We observe narrow CSEs at much higher rates during ICMEs, over 100 times more frequently for 9° or narrower than found during non-ICME solar wind.

2. Very narrow CSEs with SE beam widths $\leq 18°$ are nearly exclusively observed during ICMEs.

3. Distinct SSEs are actually observed more frequently within ICMEs than the solar wind.

4. Fully scattered SE observations ($I_{scatter} > 1.0$) occur twice as frequently in non-ICME times.

5. More than 76% of ICME times are not actually classified as either CSE or SSE by our algorithm.

6. A higher percentage of SE observations during ICME times have low symmetry indices (0 to 1/4) than during non-ICME times.

7. A higher percentage of SE observations during ICME times have low scattering indices (0 to 1/4) than during non-ICME times.

4.7 Acknowledgements

Special thanks to Ruth Skoug and John Steinberg of Los Alamos National Laboratory for their early assistance with interpreting ACE/SWEPAM data.

CHAPTER V

Conclusions

5.1 Discussion of Findings and Implications

5.1.1 Now-casting ICMEs Using Heavy Ion Charge States

Chapter II demonstrated:

1. **Elevated heavy ion charge states are often seen in interplanetary coronal mass ejections (ICMEs) and can be used for event now-casting.** Enhancements of iron, carbon, and oxygen ratios have been shown to occur in ICMEs (*Lepri et al.*, 2001). In this chapter we will demonstrate that solely using observations of heavy ion charge states, such as iron, carbon and oxygen could identify ICMEs in situ.

2. **Based on published ICME lists, we use event identification metrics to assess the utility of certain charge states as predictors of ICMEs across a full solar cycle.**

   We select the best thresholds to use for CME forecasting by creating a set of now-casts based on observational data from 1998-2011 and evaluating their accuracy compared to ICME catalogs published by Cane and Richardson (*Richardson and Cane*, 2010) and Jian et al. (*Jian et al.*, 2011).

3. **The best ICME identifiers were $Fe^{16+\,to\,24+}/Fe_{tot}$ and O^{7+}/O^{6+}, with the optimal threshold depending on user need.**

   When identifying ICMEs using in situ ACE (Advanced Composition Explorer) SWICS (Solar Wind Ion Composition Spectrometer) observations spanning 1998 to 2011, we find the charge state ratios with the highest positive predictive value for identifying ICMEs from in situ observations were $Fe^{16+\,to\,24+}/Fe_{tot}$ and O^{7+}/O^{6+}.

5.1.2 Modeling Magnetic Connectivity of SEP Sources Using ADAPT-WSA

As was discussed in Chapter III, six near-relativistic electron SEP events were all observed by both STEREO A and STEREO B when the spatial distance between the two spacecraft ranged from 32° to 72°. For these six events we evaluated the impact of considering ADAPT-WSA modeled HMF lines to estimate near-relativistic electron propagation through interplanetary space as opposed to relying on the Parker spiral approximation. Our main findings are as follows:

- Events 1 and 2 were both near-relativistic ramp events associated with full-halo CMEs and expected to be impacted by interplanetary shock acceleration. ADAPT-WSA modeling fell short of explaining the discrepancies in connectivity and onset times and intensities. We suggest that our ADAPT-WSA modeling was unable to improve upon the Parker spiral approximation for these events due to the propagation effects due to interplanetary shock acceleration and distortions to the IMF caused by the associated full-halo CME, which we did not include in our ADAPT-WSA modeling. The additional impacts of these more complex magnetic field lines which were likely impacted by the propagating full-halo CME made any improvements due to ADAPT-WSA modeling less pronounced. Interplanetary shock acceleration as is known to be associated

with near-relativistic ramp events (*Haggerty and Roelof*, 2009) and was shown to be associated with both of these events by Cohen et al. (2017).

- Event 3, observed on 02 May 2014, was a scatter-free electron spike event for which our modeled footpoints using ADAPT-WSA offered better agreement with observed onset times and intensity profiles at STEREO A and B than the Parker spiral approximated footpoints from Klassen et al. (2015).

- Event 4 was a scatter-free electron pulse event observed on 17 July 2014. ADAPT-WSA modeling indicates that the sub-PFSS magnetic field is strongly non-radial due to the coronal hole boundary at the location of the associated flaring source region, indicating that this near-relativistic pulse event, while more closely connected to STEREO A, experienced near-corona longitudinal spreading which enabled it to be seen by both STEREO spacecraft.

- Events 5 and 6 were two near-relativistic electron pulse events observed on 01 August 2014. ADAPT-WSA modeling for these events between the photosphere and the 5 R_S PFSS suggests that STEREO B was well-connected to the southern coronal hole region, explaining observations of high speed solar wind streams at STEREO B from July 31st - August 3rd, which was not explained by 2.5 R_S PFSS footpoint locations approximated using the Parker spiral (*Klassen et al.*, 2016).

- Events 3 - 6 were near-relativistic electron spike or pulse events which were scatter-free as they propagated through interplanetary space, without SEP or CME interactions, enabling clearer analysis of the connectivity differences between ADAPT-WSA modeling and Parker spiral approximation. For each of these events, ADAPT-WSA modeling appeared to support improved onset time and intensity profile analysis compared to Parker spiral connectivity.

- Because Events 3 - 6 of this study were specifically during times where interactions from coronal mass ejections and previous SEP events are minimal, a future comparison between these events presented here and additional events which travel along more complex magnetic field topologies or with missing observational data, may help indicate how SEP propagation is impacted by the magnetic topology of the inner heliosphere.

Altogether, this analysis suggests that the impact of modeling near-relativistic electron SEP events using ADAPT-WSA as opposed to using the Parker spiral approximation does help improve the full picture of acceleration and connectivity for electron spike and pulse events, as was the case for Events 3-6, whereas modeling using ADAPT-WSA has less of an impact on electron ramp events like Events 1 and 2, which are expected to be impacted by interplanetary shock-acceleration due to associated CME interactions which are not included in our ADAPT-WSA modeling.

5.1.3 Quantitative Analysis of Suprathermal Electrons during ICMEs

In Chapter IV we present a quantitative characterization scheme for analyzing ACE SWEPAM PAD observations. This scheme not only enables identification of whether an SE PAD is counterstreaming or strahl, but also identifies characteristics of the observed PADs such as the beam width for SSEs and CSEs, a scattering index and an asymmetry index. These characterization metrics are defined using three quantitative observable parameters. This scheme enables direct comparison of SSE and CSE beam width, background scattering and PAD asymmetry over large multi-year surveys and in various conditions, such as ICME or non-ICME times.

We applied this characterization scheme over a fourteen-year span from 1998-2011 which covers a complete solar cycle to determine the occurrence rates of varying widths for both SSE and CSE observations directly comparing rates during ICME and non-ICME times according to published ICME lists (*Richardson and Cane*, 2010;

Jian et al., 2011). We find several observations worthy of noting:

1. We observe narrow CSEs at much higher rates during ICMEs, over 100 times more frequently for 9° or narrower than found during non-ICME solar wind.

2. Very narrow CSEs with SE beam widths $\leq$18° are nearly exclusively observed during ICMEs.

3. Distinct SSEs are actually observed more frequently within ICMEs than the solar wind.

4. Fully scattered SE observations ($I_{scatter} > 1.0$) occur twice as frequently in non-ICME times.

5. More than 76% of ICME times are not actually classified as either CSE or SSE by our algorithm.

6. A higher percentage of SE observations during ICME times have low symmetry indices (0 to 1/4) than during non-ICME times.

7. A higher percentage of SE observations during ICME times have low scattering indices (0 to 1/4) than during non-ICME times.

5.1.4 Science Questions Revisited

Altogether, each of the studies presented in this dissertation endeavours to classify and quantify some of the effects propagation through the inner heliosphere have on solar particle populations, particularly those that are drivers of geo-effective space weather. We have seen that not only can in situ measurements of heavy ion charge states inform us of the solar source region conditions of interplanetary coronal mass ejections, but there are also particular values which can be used to now-cast ICMEs, which could be used to aid in ICME identification and forecasting. We have seen when

we compare the modeled magnetic connectivity of solar energetic particles using the ADAPT-WSA model to estimates that rely on the Parker spiral approximation for a set of events observed by multiple spacecraft, that for those that are scatter-free electron spike events, the ADAPT-WSA modeling yields improvement. We have found that we can quantitatively classify and quantify the distributions of suprathermal electrons observed in the solar wind compared with those observed in interplanetary coronal mass ejections over a complete solar cycle to study the magnetic topology and perhaps even the substructure of ICMEs.

1. **How well do heavy ion charge distributions now-cast ICMEs at 1 AU?**

   As established in Chapter II, we sought to determine how effectively certain parameters of heavy ion charge states can be used to now-cast in situ observations of ICMEs. Three optimal threshold values were found for each of six different charge state parameters of carbon, oxygen and iron. The most effective of the charge state parameters were $Fe^{16+\,\mathrm{to}\,24+}/Fe_{\mathrm{tot}}$ and O^{7+}/O^{6+}. The choice of which threshold to use has trade-offs which were presented in Chapter II. Ultimately the optimal threshold to use depends on the application and priorities of the now-caster.

2. **How do arrival time, velocity and intensity of SEP electrons compare to modeled magnetic connectivity using ADAPT-WSA vs Parker Spiral?**

   As established in Chapter III, our analysis suggests that the impact of modeling near-relativistic electron SEP events using ADAPT-WSA as opposed to using the Parker spiral approximation does help improve the full picture of acceleration and connectivity for electron spike and pulse events, whereas modeling using ADAPT-WSA has less of an impact on electron ramp events like those observed on 11 October 2013 and 25 February 2014, which are expected to be

impacted by interplanetary shock-acceleration caused by interactions with associated full-halo CMEs which are not included in our ADAPT-WSA modeling.

3. **How often are CSEs and strahl observed during in situ observations of ICMEs and what are their characteristics when compared to suprathermal electrons in the solar wind?**

   As established in Section IV we find that narrow CSEs are observed at much higher rates during ICMEs, over 100 times more frequently for 9° or narrower than found during non-ICME solar wind. We find that very narrow CSEs with SE beam widths $\leq$18° are nearly exclusively observed during ICMEs. We find that narrow, distinct SSEs are actually observed more frequently within ICMEs than the solar wind.

Connecting all the studies of this dissertation together: each aim to improve understanding and tracing of the heliospheric magnetic field and the factors that play a role in the propagation of ICMEs, SEPs and SEs in the inner heliosphere. These studies successfully set us up to continue researching space weather propagation through the inner heliosphere. They established classification methods which can be implemented over new data sets and quantitative analysis which can be applied to new case events.

We will discuss the next steps for continuing the research presented in this dissertation in the next section. The classification methods used in Chapter II will be refined for use in now-casting by looking at charge state threshold ensembles. These methods will also be applied to a new study investigating the correlation between observations of solar energetic particles and features related to acceleration mechanisms at the source and during interplanetary propagation. Now that a quantitative characterization scheme has been established to classify CSEs and SSEs, and a baseline created, the analysis presented in Chapter IV can be applied to case events to

investigate the magnetic fields and substructure within ICMEs during interplanetary propagation.

5.2 Future Work

5.2.1 Now-Casting ICMEs Using Machine Learning

The heavy ion charge state ICME classification study, which was discussed in Chapter II, used a classification algorithm as a forecast method. Future applications of this research will address a multitude of classes, where some classes are an ensemble of those considered here, such as a class which is defined with charge state parameters above both the $Fe^{16+\,\mathrm{to}\,24+}/Fe_{tot}$, and O^{7+}/O^{6+} thresholds. Using a combination of the six charge state parameters to produce ensemble classes, which are not mutually exclusive, one winds up with hundreds of possible classes. To test each individual ensemble threshold as a forecast method individually or to consider multiple classes which are not mutually exclusive, using the methods of this paper would be too computationally expensive. Thus, we seek to continue the study of these charge state parameters for ICME now-casting using machine learning classification algorithms. This study was essentially a baby machine learning classification algorithm which considered only two classes and used the C&R and LJ et al. ICME reference lists as training sets. Classification algorithms have been designed to handle much larger numbers of classes and we intend to use the results of this study as a guide to train a machine learning algorithm to investigate the value of a range of ensemble thresholds as forecast methods which might be more effective at ICME now-casting than a single charge state parameter alone.

5.2.2 Interplanetary Propagation of SEPs

5.2.2.1 Problem Statement

Space Weather events such as solar energetic particles (SEP) originate at the Sun and propagate through interplanetary space towards Earth. When these events reach Earth they shower the space environment with charged particles which damage or interfere with spacecraft, in turn interfering with ground communications and GPS navigation (*National Science and Technology Council*, 2015). The Air Force Research Laboratory's Battlespace Environment Division is engaged in efforts to improve the ability to forecast and diagnose variations in the space environment which may pose a threat to ongoing space-based operations and assets. A major limitation in forecasting geo-effective SEP events is the difficulty modeling propagation through interplanetary space and producing accurate predictions for time of arrival. Whether an event will be geo-effective is highly dependent upon time of arrival. If timing is off a geo-effective event may be incorrectly forecasted to miss Earth entirely or an event may arrive hours ahead of predictions. This project is meant to improve understanding of how SEP events are affected by intervening magnetic structures and transient events in interplanetary space, improving understanding of SEP propagation through interplanetary space, which can then inform forecasting models to improve SEP time of arrival predictions.

We will conduct a multi-event SEP survey quantifying the correlations between interplanetary magnetic structures and interplanetary transient events and the impacts on the intensity-time profiles of solar energetic particle (SEP) observations. We will address the question: "What impacts do behavior of the surrounding heliospheric magnetic field and interplanetary transient events have on the intensity-time profiles of SEP proton events?"

5.2.2.2 Background

Intensity-time profiles of SEPs (E > 10 MeV) at 1 AU reflect the impacts of a number of physical processes both during acceleration and interplanetary transport (*Kahler and Ling*, 2017). SEP intensity-time profiles are often used as the basis for diagnostic timescales, which are used in modeling and describing the acceleration and transport of SEPs (e.g., *Chollet et al.*, 2010; *Mewaldt et al.*, 2008; *Crosby et al.*, 2015).

SEP research has long classified SEP events into two groups, impulsive and gradual, largely classified by their correlations with observed solar eruptive events known to be associated with their acceleration: solar flares and coronal mass ejections (CMEs), respectively (e.g., *Lin*, 1970; *Reames*, 2013). While studying the associations of SEP events with solar eruptions that are associated with their acceleration has long dominated SEP research, a thorough observation-driven study of associations related to interplanetary transport still needs to be performed.

There have been a great many studies which investigate the impacts of interplanetary CME (ICME) acceleration on SEPs (e.g., *Kahler and Vourlidas*, 2013, 2014a; *Aschwanden et al.*, 2017, and references therein), and for example, *Lario et al.* (2014), has already demonstrated a positive correlation between the SEP peak intensity, I_p, with associated CME-driven shock acceleration. Many impacts, however, of interplanetary transport are neglected in SEP surveys. For example, the effects of transport across the heliospheric current sheet, while expected to have an impact, have yet to be thoroughly studied (*Laitinen and Dalla*, 2017) and are frequently neglected entirely (e.g., *Ragot*, 2006). The effects of nearby solar wind conditions on the SEP intensity-time profiles have begun to be investigated (e.g., *Kahler and Vourlidas*, 2014b). Some have been modeling the impacts of the interplanetary magnetic field (IMF) on SEP intensity-time profiles (e.g., *Chollet et al.*, 2010), however observational data-based studies are lacking. Hence, for this study we will include analysis of suprathermal electron pitch angle distributions - which give an indication as to the magnetic topol-

ogy and scattering processes along the IMF, CIRs - which are transient events that greatly distort the nearby IMF (as shown in Figure 5.1), and heliospheric current sheet crossings - which are theorized to cause cross-field particle diffusion (*Laitinen and Dalla*, 2017).

For this study we seek to quantitatively compare the correlation of these interplanetary magnetic structures and transient events with certain features that characterize SEP intensity-time profiles. We will include the following interplanetary structures: ICMEs (CME-association, ICME velocities, ICME plasma temperature), solar wind (solar wind speed, solar wind heavy ion charge distributions), suprathermal electron pitch angle distributions, CIRs, and heliospheric current sheet crossings.

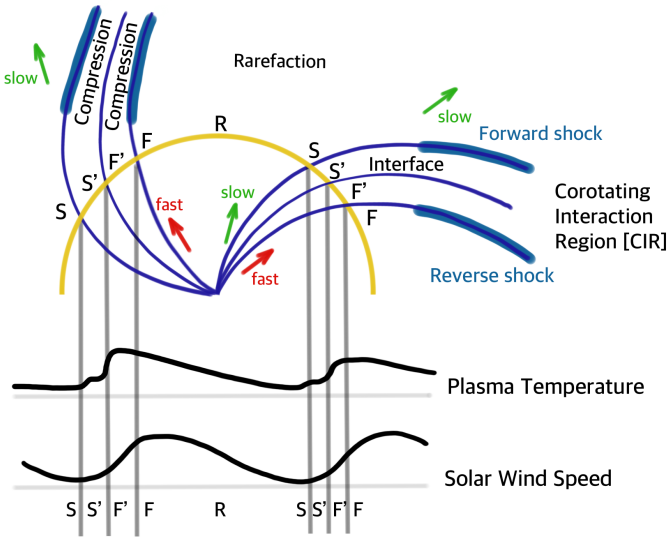

Figure 5.1: Diagram of a CIR in the solar wind. Green and red arrows indicate which regions are driven by slow and fast solar wind, respectively, these solar wind speeds are also marked with S for slow and F for fast. Blue magnetic field lines show the compression regions of bunched magnetic field lines and the rarefaction region between them where the density of magnetic field lines is lower. The golden arc represents the path of a spacecraft which observes the plasma temperature and solar wind speed depicted in black in the lower portion of the diagram. Based on a diagram of a CIR from (*Richardson*, 2004).

5.2.2.3 General Methodology

We will conduct this SEP-interplanetary structure correlation study in three stages:

1. We will characterize the in situ observed features of time-intensity profiles of SEP events, using the proton peak intensity, I_p and a two-parameter fit, using α and β of a modified Weibull function as described by *Kahler and Ling* (2017; 2018b). We will begin with a data set of 72 gradual SEP proton events (E > 50 MeV) observed by the Geostationary Operational Environmental Satellites (GOES) satellites from 1998 to 2006, which we have already compiled. We may choose to subsequently expand this survey to include impulsive SEP events and more recent observations, such as those events included in *Kahler and Ling* (2017).

2. We will classify the associations of interplanetary structures using in situ observational data from the Advanced Composition Explorer (ACE) (available at the ACE Science Center, http://www.srl.caltech.edu/ACE/ASC/level2/), for each SEP event in our SEP data set. We will be including the following structures and transients: ICMEs (CME-association, ICME velocities, ICME plasma temperature), solar wind (solar wind speed, solar wind heavy ion charge distributions), suprathermal electron pitch angle distributions, CIRs, and heliospheric current sheet crossings.

3. We will use receiver operating characteristic (ROC) curves as metrics to quantitatively evaluate the correlation strength between each SEP intensity-time profile feature and the observable interplanetary structures related to the interplanetary propagation, IMF and transient events of our classification scheme. Our methods for the correlation analysis using ROC curves is discussed in Section 5.2.2.4.

An example intensity-time profile for an event included in the initial data set for this survey can be seen in Figure 5.2. This particular event was observed on 15 June 2001. The 50 MeV profile has a steep rise which will be characterized by a smaller magnitude α, a sharper drop in the tail which will be characterized by a negative α, and a medium length tail which will be described by β, and a I_p near 20 pfu or 2 protons/cm^2/s/sr (*Kahler and Ling*, 2017).

There are a number of interplanetary structures and transients for which we would like to evaluate correlation strength. However, this study is meant to span two years. We intend to expand the analysis to include each interplanetary structure one at a time. During the first year, we expect to evaluate the correlation of three of the SEP intensity-time profile features, α, β, and I_p, with the occurrence of associated ICMEs, nearby CIRs, surrounding solar wind speed, and solar wind heavy ion charge state distributions. Subsequently, during the second year we will add each of the other interplanetary structures to our analysis one at a time.

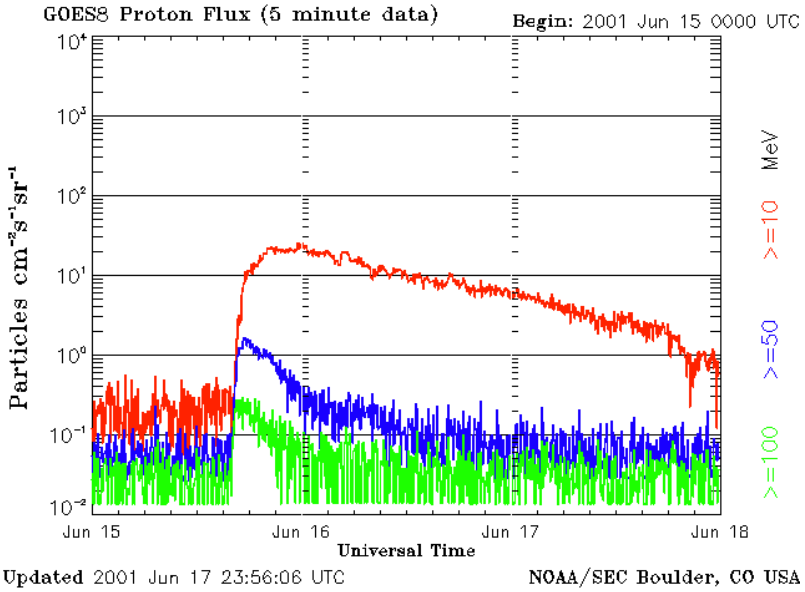

Figure 5.2: Proton intensity-time profile of a gradual SEP event observed by GOES-8 on 15 June 2001. The intensity versus time profiles for each energy band, 10 MeV, 50 MeV and 100 MeV are shown in red, blue and green, respectively. This is the 5 minute averaged observational data.

5.2.2.4 Unusual Method: ROC Curves

Receiver operating characteristic (ROC) curves are frequently used in statistics and computational fields to evaluate relative accuracy of a forecast or model. The use of ROC curves are growing with the advent of machine learning, particularly when used with classifiers (*Lachiche and Flach*, 2003). For this study we will be using ROC curves to quantitatively evaluate the correlation between intensity-time profile features with associated interplanetary structures.

ROC curves can be used as metrics to evaluate the relative accuracy of a set of forecasts with respect to a reference list of observed events. They graphically show the correlation between a forecast parameter and the occurrence of an event. For the purposes of this study, we will be using the features of intensity-time profiles of SEPs as forecast parameters and evaluate their correlation with the occurrence of interplanetary structures.

ROC curves plot true positive rate (TPR) versus false positive rate (FPR). In the case of this study, a true positive is when the SEP intensity-time profile feature is above a certain threshold value when the event is associated with the interplanetary structure. Then a false positive is when the SEP profile feature is above the threshold when the event is not associated with the interplanetary structure.

Figure 5.3 is an example of an ROC curve, with a clear positive correlation, which was used to evaluate the forecast ability of the O^{7+}/O^{6+} heavy ion charge state ratio with the occurrence of ICME events. Observations from the Advanced Composition Explorer Solar Wind Ion Composition Spectrometer from 1998 to 2011 were used in reference to ICME observations as listed in the Richardson and Cane ICME list (*Richardson and Cane*, 2010) and the Jian et al. ICME list (*Jian et al.*, 2011).

Every point along an ROC curve gives the TPR and FPR of a different threshold choice. Following the curve, the highest threshold choices fall where TPR and FPR are close to zero, or the lower-left corner, and the lowest threshold choices are where

TPR and FPR are near one, or the upper-right corner in ROC space. The stronger the predictive strength of the selected forecast parameter, the closer the curve will bend towards the upper-left corner in ROC space, where TPR = 1 and FPR = 0. Therefore, it is promising when the forecast parameter in question bends clearly towards the upper-left corner. A straight unity line, (where TPR = FPR,) would indicate no clear threshold choice. A curve that bends to the lower-right corner, (where TPR = 0 and FPR = 1,) would indicate that the parameter was anti-correlated with event occurrence.

Youden's J statistic (TPR + TNR - 1), ranges from zero to one and is a maximum in the upper-left corner of ROC space, optimizing for maximum TPR and minimum FPR equally. The maximum J statistic will be used in our study as a quantitative value related to the maximum correlation strength for each ROC curve.

Classification metrics based in ROC space are not automatically skewed by extreme class imbalance (*Ferri et al.*, 2011). In the case of this study the class imbalance will vary for each transient evaluated. For example, in the case of ICME observations, the ratio of ICME observations to non-ICME solar wind observations is about 0.078, when using the Richardson et al. ICME list (*Richardson and Cane*, 2010), which is far from the 0.5 that the ratio would be were the classes balanced. The independence of ROC curves to class balance makes ROC curves as described throughout this section better for evaluating correlation strength as opposed to other forecast skill metrics, which often are skewed by class imbalance (*Ferri et al.*, 2011). We will be able to compare the ROC curves for each interplanetary structure and use them to evaluate their correlation strength with each SEP intensity-time profile feature, without considering the differing occurrence rates for each interplanetary structure.

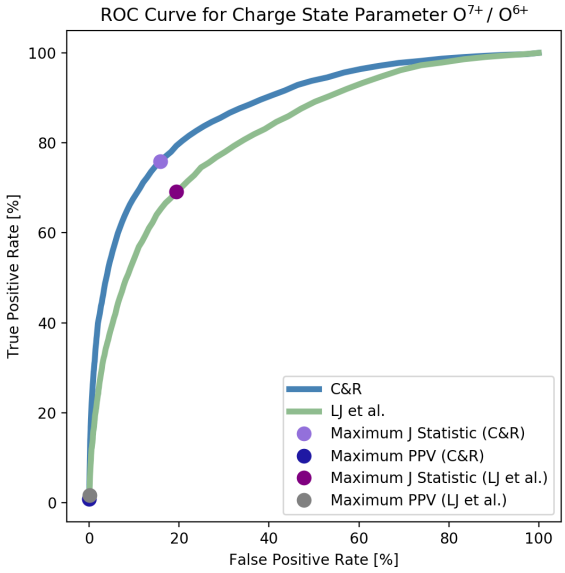

Figure 5.3: This Receiver Operating Characteristic (ROC) curve gives the ratio of true positive detection to false detection for the observed heavy ion charge state ratio O^{7+}/O^{6+}. Blue results are based on the interplanetary coronal mass ejection boundaries given in the Richardson et al. ICME list (*Richardson and Cane*, 2010). Green results are based on ICME boundaries from the Jian et al. ICME list (*Jian et al.*, 2011). The maximum J statistic values (TPR + TNR - 1) and the maximum positive predictive values (TPR / (TPR+FPR)·100) are marked with purple and blue/grey dots respectively.

5.2.2.5 Expected Results

We expect to produce ROC curves (described in Section 5.2.2.4) for each of features of the SEP intensity-time profiles compared to each of the interplanetary structures described in Section 5.2.2.3. For each intensity-time profile feature and each interplanetary structure, we will then have a resulting graphical metric and a single quantitative J statistic value to effectively compare their correlation strengths.

During the first year we intend to publish the results of the correlation analysis for the association with ICMEs and CIRS in the Journal of Geophysical Research: Space Physics or Solar Physics. We plan to start with the correlation with ICMEs given that we expect a positive correlation between associated ICMEs and greater SEP peak

intensity, I_p, due to the work of Lario et al. (2014) and others. Since this positive correlation is already known, beginning with the ICME correlation analysis will offer a stronger foundation from which to compare the other less studied interplanetary structure correlation strengths. While we expect CIRs to cause longitudinal spreading of SEP events (*Richardson*, 2004; *Laitinen and Dalla*, 2017), the impact on the peak intensity and intensity-time profile has not been directly studied for a survey of SEP events, making this an optimal comparison to begin with.

During the second year, once the creation of ROC curves for each correlation comparison is complete, we intend to publish on the structures with the strongest correlation strengths, and analyze their interplanetary impacts on SEPs. Thus enabling further subsequent research into the causes of these correlations.

Due to the nature of this study - that we rank each and every correlation - should the correlation strengths be lower than expected, we will still have interesting results. A major outcome of this study will be a ranked list, which will give us the ability to direct research attention towards interesting or promising correlations, regardless of their actual quantitative strengths. This simple ranking already enables interesting follow-on studies, as will be described in the next section.

Some proton intensity-time profiles do not lend themselves well to the characterization using the α, β, and I_p fit. In a preliminary study we have already classified 24 gradual SEP events observed by GOES as having "unusual" profiles and if these events prove themselves unfit for characterization using the α, β, and I_p features, then they will be considered separately as an additional SEP intensity-time profile feature, and may be removed from the statistical analysis of the larger data set.

5.2.2.6 Significance and Application

Once the creation of ROC curves for each correlation comparison is complete, we will have a set of ROC curves to compare to one another, giving us the ability to

rank each interplanetary structure for its correlation strength to each intensity-time profile feature.

Efforts are already being made to modify and improve SEP forecasting at the Air Force Research Laboratory, for example with the use of the Proton Prediction System (*Kahler et al.*, 2017; *Kahler and Ling*, 2018a). The set of ranked correlation comparisons resulting from this study will be able to be used by the Air Force Research Laboratory to direct subsequent research to the characterization of the impacts of those interplanetary structures with the greatest correlation strengths to improve SEP forecasting. For example, say our study finds that increased β, or a longer duration of the intensity-time profile, is highly correlated with CIRs, then investigation into the impacts of CIRs, which are recurring events which can last through multiple solar rotations, see Figure 5.1 (*Richardson*, 2004), could lead to a feature which can be characterized well before SEP eruptions, thus if incorporated into forecast modeling, could thereby enable better forecasting of SEP duration.

In order to calculate the energy flux budget of SEP events, the integration of the entire I(t) intensity-time profile over both time and energy is necessary(*Kahler and Ling*, 2018b). Knowledge of the energies of SEP events allows for comparison to the entire energy flux budget of the solar eruptive events (e.g. *Chollet et al.*, 2010; *Aschwanden et al.*, 2017) and with CMEs directly (e.g., *Mewaldt et al.*, 2008; *Kahler and Vourlidas*, 2013; *Aschwanden et al.*, 2017). Our analysis in this study of the α and β parameters of the Weibull function which fits I(t), then enables further analysis to compare how estimates of the energy budget of SEP events is actually impacted by interplanetary propagation effects as opposed to the solar eruptive acceleration mechanisms to which they are so often compared.

5.2.3 Counterstreaming Suprathermal Electrons and ICME Substructure

In continuation of the study presented in Chapter IV, we intend to further evaluate the occurrence of the various SSE and CSE widths, scattering coefficients and asymmetry indices with relation to ICME substructure. We intend to conduct a survey to quantify the occurrence of the CSE and SSE PAD properties defined and discussed in Section 4.4.2 with respect to ICME features and plasma properties, such as magnetic structure, filament plasma, heavy ion charge state distributions of Fe, C and O, plasma temperature, density and velocity.

APPENDICES

APPENDIX A

Supplemental Figures for Chapter II

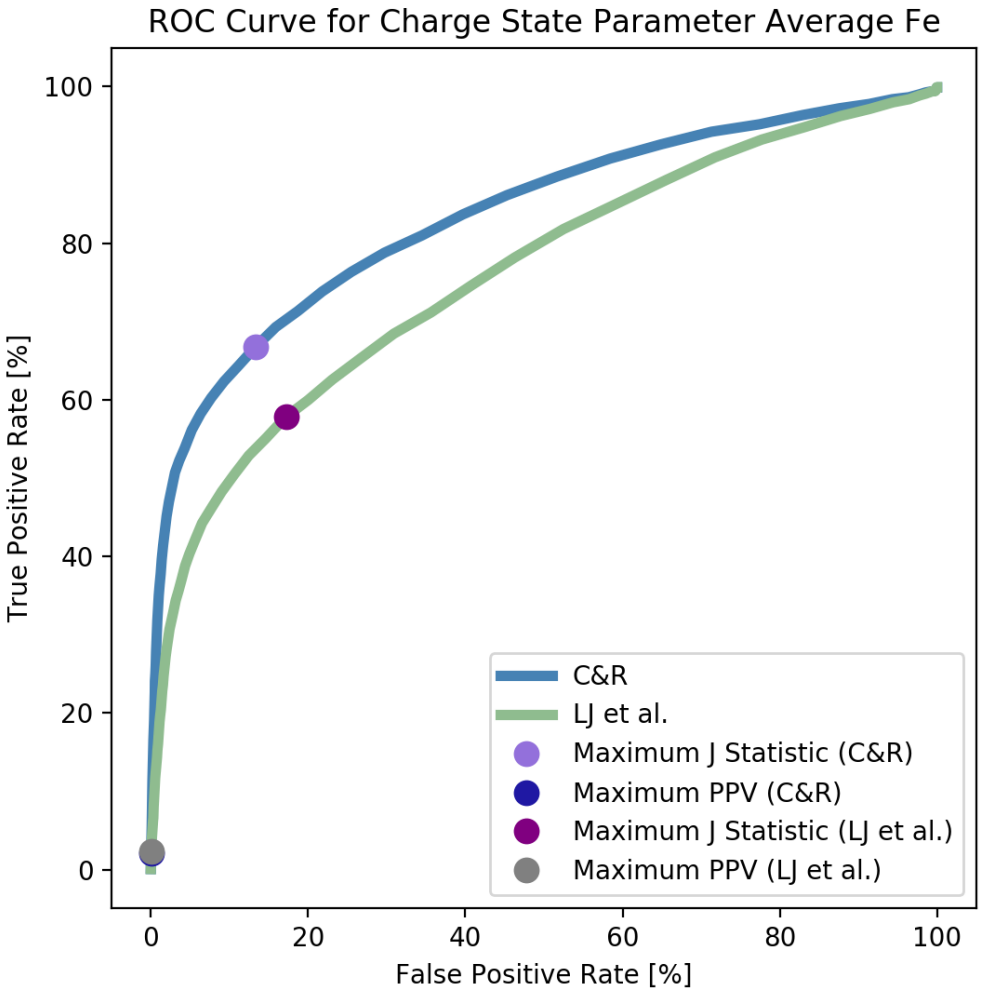

Figure A.1: This Receiver Operating Curve (ROC) gives the ratio of true positive detection to false detection for the charge state parameter $< Q_{\mathrm{Fe}} >$. Blue results are based on the interplanetary coronal mass ejection boundaries given in the C&R ICME list (*Richardson and Cane*, 2010). Green results are based on ICME boundaries from the LJ et al. ICME list (*Jian et al.*, 2011).

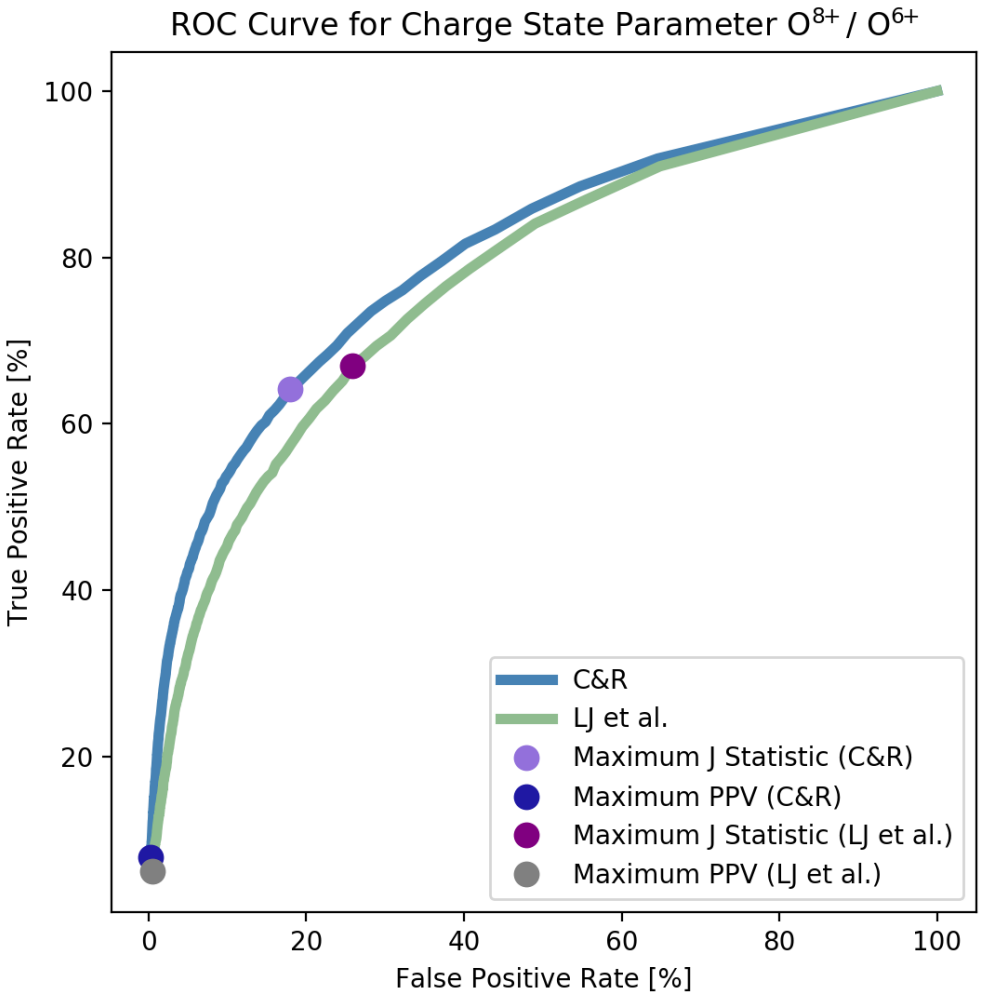

Figure A.2: This Receiver Operating Curve (ROC) gives the ratio of true positive detection to false detection for the charge state parameter O^{8+}/O^{6+}. Blue results are based on the interplanetary coronal mass ejection boundaries given in the C&R ICME list (*Richardson and Cane*, 2010). Green results are based on ICME boundaries from the LJ et al. ICME list (*Jian et al.*, 2011).

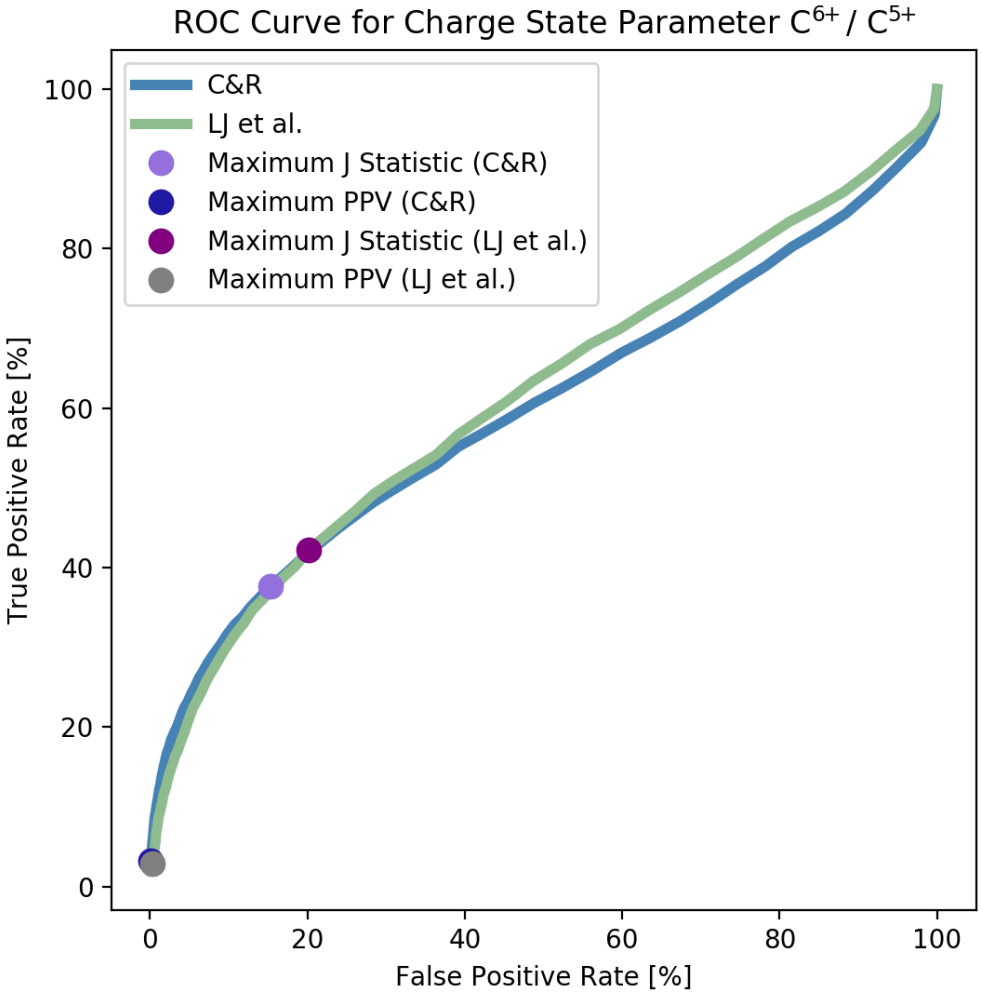

Figure A.3: This Receiver Operating Curve (ROC) gives the ratio of true positive detection to false detection for the charge state parameter C^{6+}/C^{5+}. Blue results are based on the interplanetary coronal mass ejection boundaries given in the C&R ICME list (*Richardson and Cane*, 2010). Green results are based on ICME boundaries from the LJ et al. ICME list (*Jian et al.*, 2011).

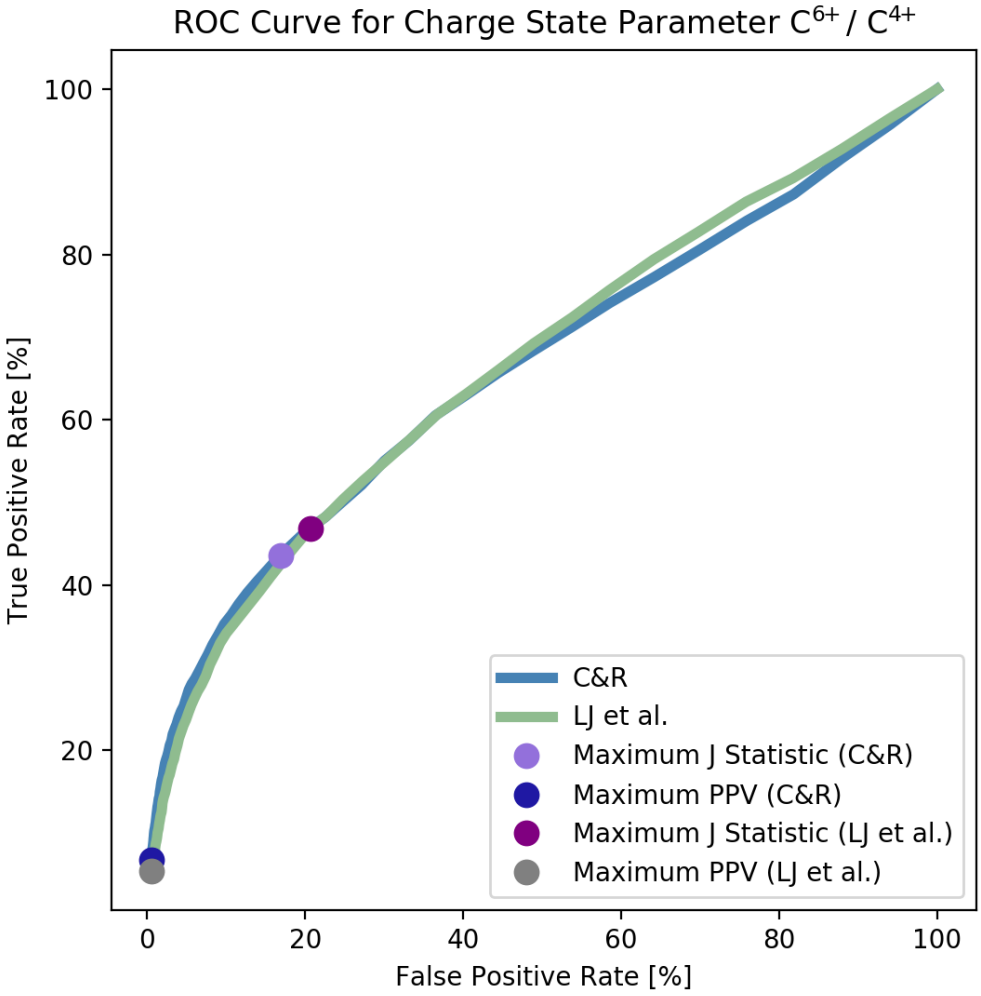

Figure A.4: This Receiver Operating Curve (ROC) gives the ratio of true positive detection to false detection for the charge state parameter C^{6+}/C^{4+}. Blue results are based on the interplanetary coronal mass ejection boundaries given in the C&R ICME list (*Richardson and Cane*, 2010). Green results are based on ICME boundaries from the LJ et al. ICME list (*Jian et al.*, 2011).

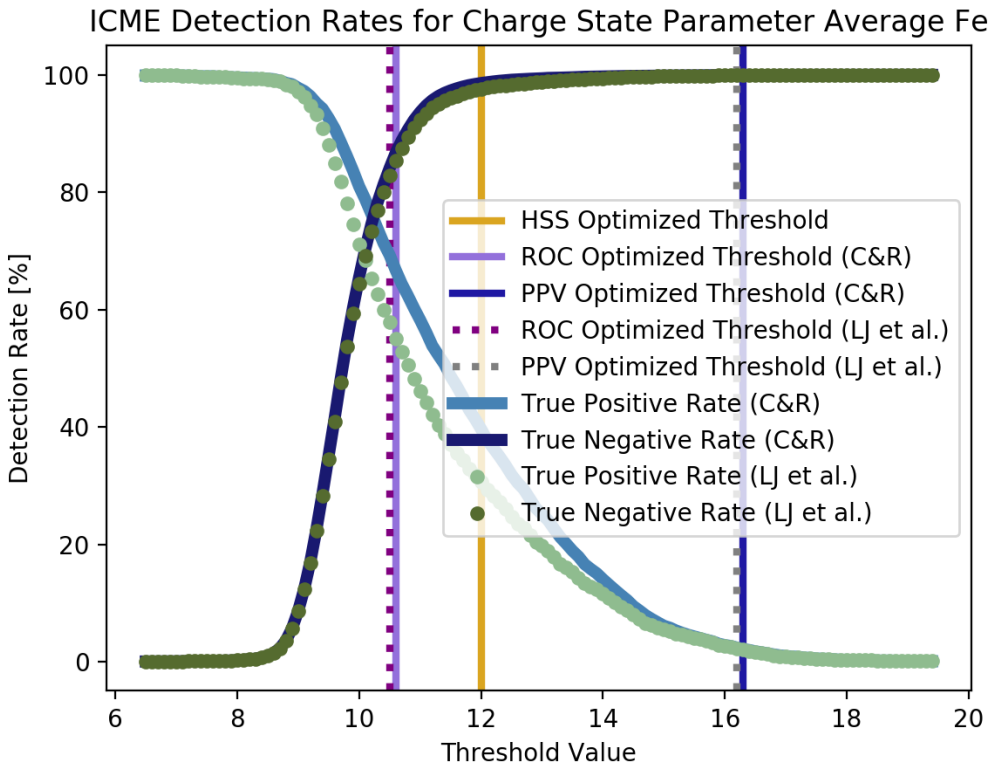

Figure A.5: This figure shows how the detection rate of $< Q_{\mathrm{Fe}} >$ varies with threshold choice. Vertical lines represent threshold choices that optimize for HSS and ROC. Solid lined results are based on the ICME boundaries from the C&R ICME list (*Richardson and Cane*, 2010). Dotted results are based on the ICME boundaries from the LJ et al. ICME list (*Jian et al.*, 2011). Navy results are based on the set of all non-event times binned by 2 hour intervals. Green results are based on the set of all ICME event times binned in 2 hour intervals.

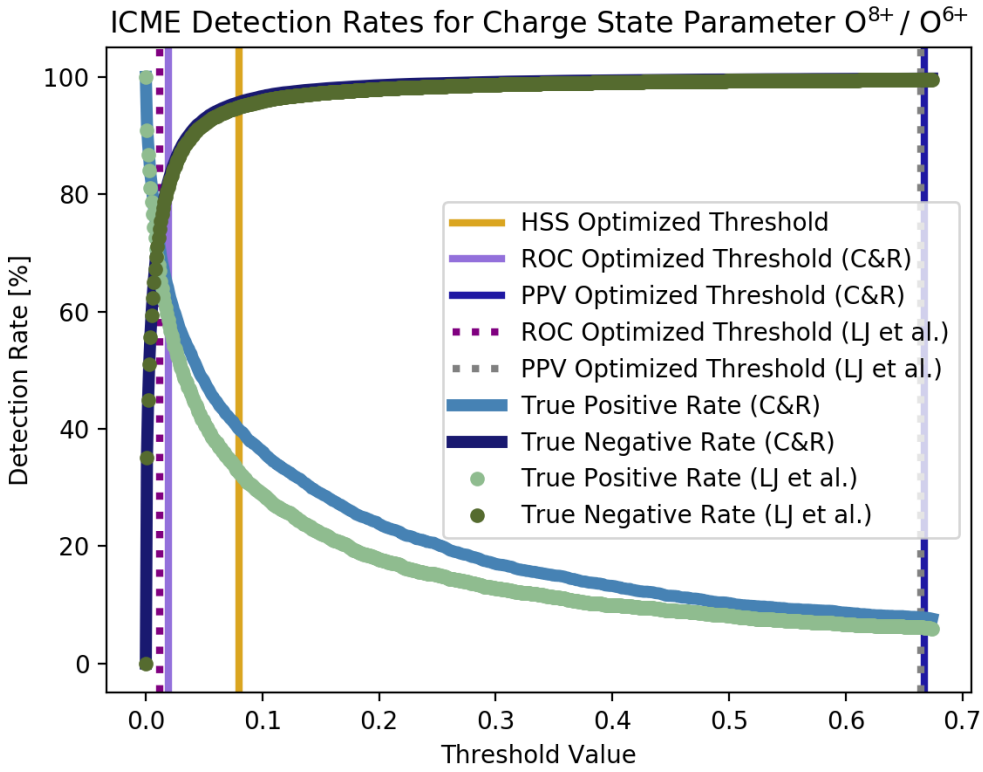

Figure A.6: This figure shows how the detection rate of O^{8+}/O^{6+} varies with threshold choice. Vertical lines represent threshold choices that optimize for HSS and ROC. Solid lined results are based on the ICME boundaries from the C&R ICME list (*Richardson and Cane*, 2010). Dotted results are based on the ICME boundaries from the LJ et al. ICME list (*Jian et al.*, 2011). Navy results are based on the set of all non-event times binned by 2 hour intervals. Green results are based on the set of all ICME event times binned in 2 hour intervals.

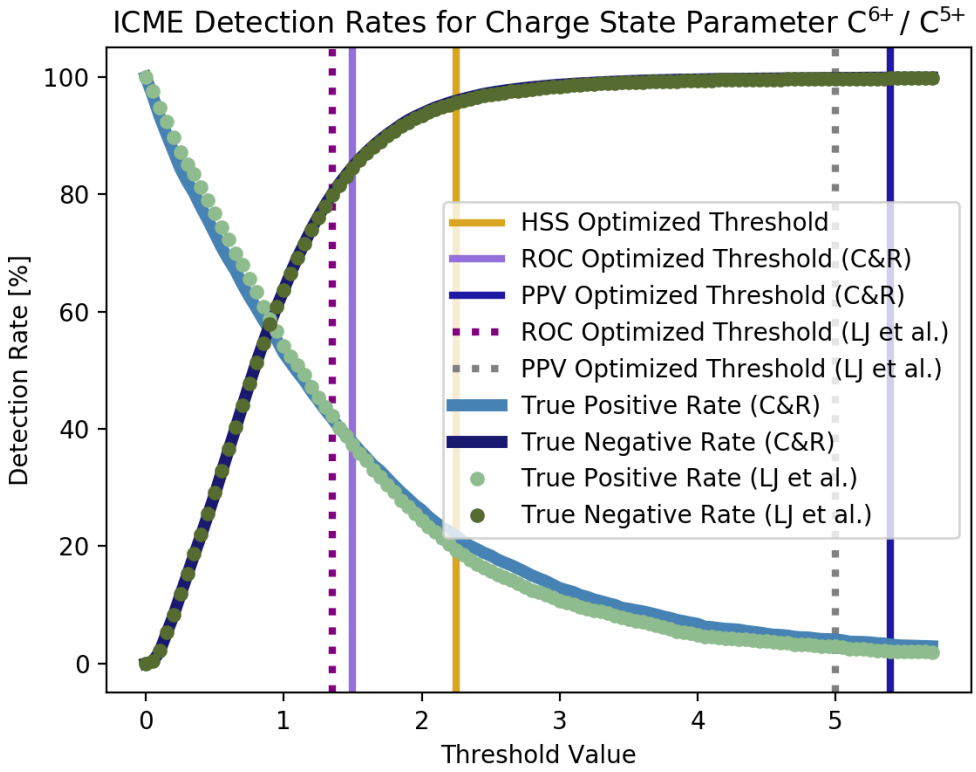

Figure A.7: This figure shows how the detection rate of C^{6+}/C^{5+} varies with threshold choice. Vertical lines represent threshold choices that optimize for HSS and ROC. Solid lined results are based on the ICME boundaries from the C&R ICME list (*Richardson and Cane*, 2010). Dotted results are based on the ICME boundaries from the LJ et al. ICME list (*Jian et al.*, 2011). Navy results are based on the set of all non-event times binned by 2 hour intervals. Green results are based on the set of all ICME event times binned in 2 hour intervals.

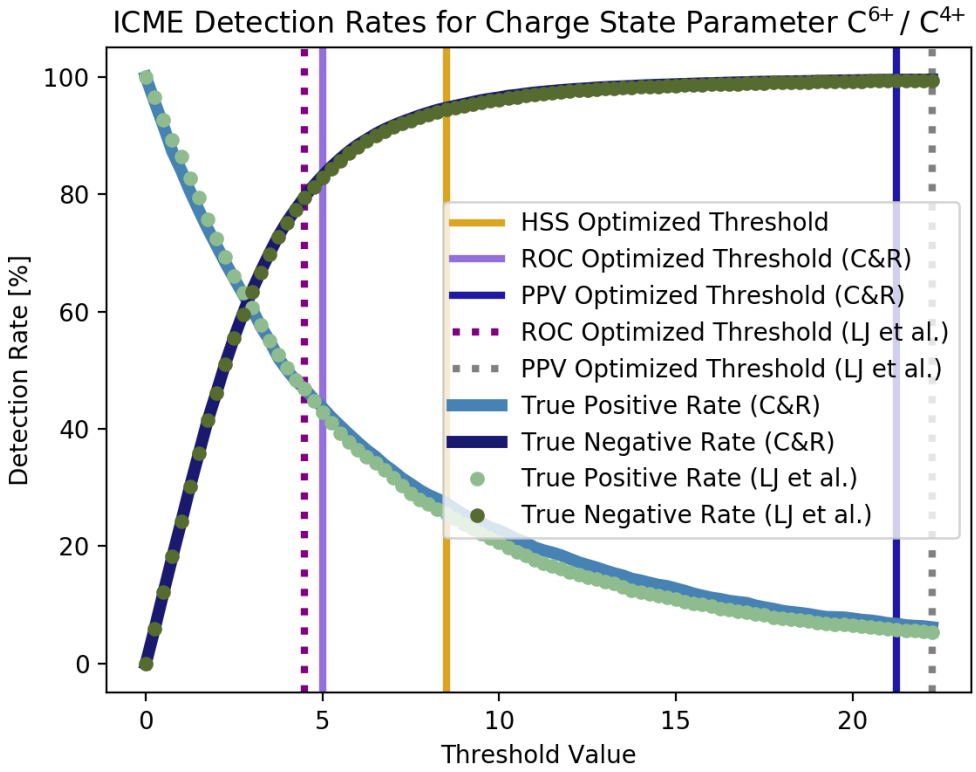

Figure A.8: This figure shows how the detection rate of C^{6+}/C^{4+} varies with threshold choice. Vertical lines represent threshold choices that optimize for HSS and ROC. Solid lined results are based on the ICME boundaries from the C&R ICME list (*Richardson and Cane*, 2010). Dotted results are based on the ICME boundaries from the LJ et al. ICME list (*Jian et al.*, 2011). Navy results are based on the set of all non-event times binned by 2 hour intervals. Green results are based on the set of all ICME event times binned in 2 hour intervals.

APPENDIX B

Supplemental Figures for Chapter III

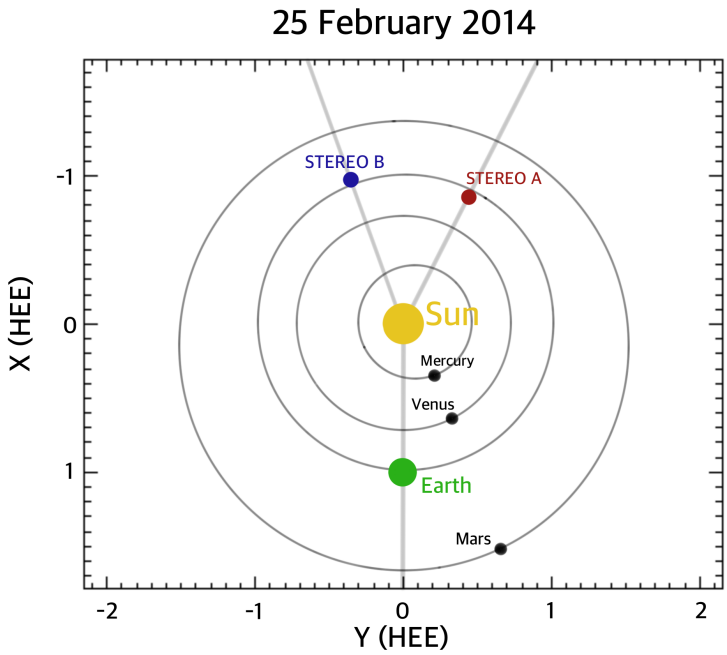

Figure B.1: Map of the relative STEREO A, STEREO B and Earth locations in the heliocentric earth ecliptic plane. Coordinates are given in Heliocentric Earth Ecliptic (HEE). The spacecraft and planetary locations are shown at the time of Event 2 on February 25th, 2014 when the STEREO A and STEREO B angular separation was 47°.

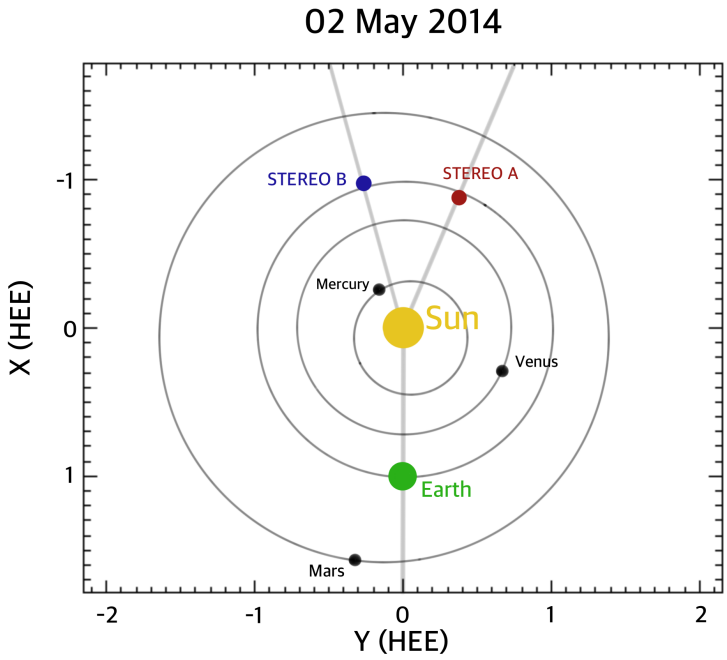

Figure B.2: Map of the relative STEREO A, STEREO B and Earth locations in the heliocentric earth ecliptic plane. Coordinates are given in HEE. The spacecraft and planetary locations are shown at the time of Event 3 on May 2nd, 2014 when the STEREO A and STEREO B angular separation was 38°.

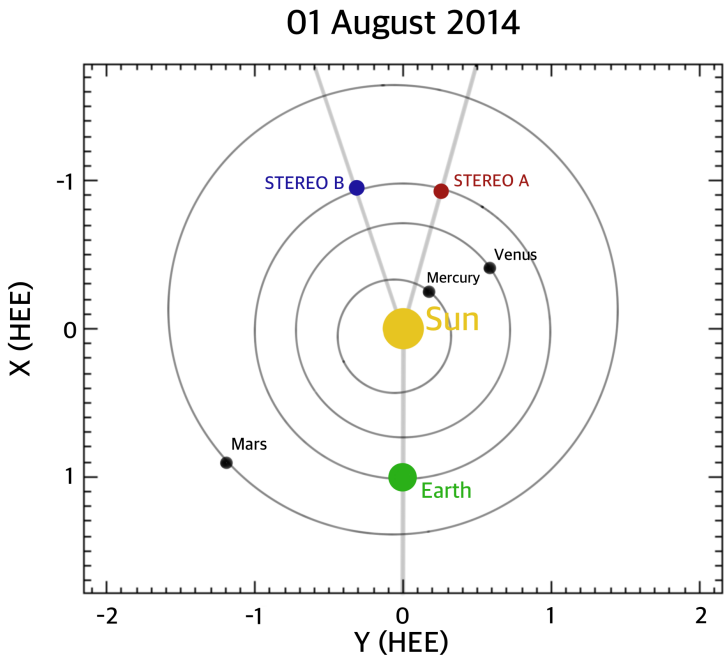

Figure B.3: Map of the relative STEREO A, STEREO B and Earth locations in the heliocentric earth ecliptic plane. Coordinates are given in HEE. The spacecraft and planetary locations are shown at the time of Events 5 and 6 on August 1st, 2014 when the STEREO A and STEREO B angular separation was 34°.

Event 1 ADAPT-WSA Modeled Magnetic Connectivity Results

Event 1 for STEREO A at 2013-10-11 07:34:00 (83, 21)

Forecast Window, Realization	Field Line to Flare Source Separation [deg.]	Field Line Footpoint Locations (long.,lat.)	Number of ADAPT-WSA Field Lines Comprising Results
05-Day Forecast, R001	46° to 47°	(35, -7) (35, -7) (32, -7) (30, -7) (35, -7) (33, -7) (33, -7)	7
05-Day Forecast, R003	46° to 47°	(35, -7) (33, -7) (32, -7) (30, -7) (33, -7) (31, -7)	6
05-Day Forecast, R004	46° to 47°	(35, -7) (32, -7) (30, -7) (28, -7) (33, -7) (33, -7)	6
05-Day Forecast, R007	46° to 47°	(33, -7) (30, -7) (28, -7) (33, -7)	4
05-Day Forecast, R009	46° to 47°	(33, -7) (30, -7) (28, -7) (33, -7)	4

Event 1 for STEREO B at 2013-10-11 07:47:00 (83, 21)

Forecast Window, Realization	Field Line to Flare Source Separation [deg.]	Field Line Footpoint Locations (long.,lat.)	Number of ADAPT-WSA Field Lines Comprising Results
05-Day Forecast, R002	10° to 17°	(118, -3) (117, -3) (115, -3) (113, -3) (111, -3) (109, -3) (107, -3) (105, -3) (105, -3)	9
05-Day Forecast, R005	7° to 16°	(93, -2) (91, -2) (104, -3) (102, -2) (100, -2) (98, -2) (96, -2) (94, -2) (92, -2) (90, -2) (117, -3) (115, -3) (113, -3) (111, -3) (109, -3) (107, -3) (105, -3) (103, -3) (117, -3) (115, -3) (113, -3) (111, -3) (109, -3) (107, -3) (105, -3) (103, -3) (101, -2) (99, -2) (97, -2) (95, -2) (93, -2) (91, -2) (89, -2)	33
05-Day Forecast, R006	7° to 62°	(115, -3) (107, -3) (122, -3) (120, -3) (118, -3) (116, -3) (114, -3) (112, -3) (110, -3) (108, -3) (106, -3) (104, -3) (102, -2) (100, -2) (98, -2) (96, -2) (94, -2) (92, -2) (121, -3) (119, -3) (117, -3) (115, -3) (113, -3) (111, -3) (109, -3) (107, -3) (105, -3) (103, -3) (105, -3)	29
05-Day Forecast, R009	9° to 10°	(105, -3) (103, -3) (101, -2)	3
05-Day Forecast, R011	7° to 16°	(107, -3) (94, -2) (92, -2) (119, -3) (117, -3) (115, -3) (113, -3) (111, -3) (109, -3) (107, -3) (105, -3)	11

Event 1 for ACE at 2013-10-11 11:10:00 (83, 21)

Forecast Window, Realization	Field Line to Flare Source Separation [deg.]	Field Line Footpoint Locations (long.,lat.)	Number of ADAPT-WSA Field Lines Comprising Results
04-Day Forecast, R000	182° to 182°	(243, 6)	1
04-Day Forecast, R002	181° to 182°	(236, 6) (245, 6) (240, 6) (238, 6)	4
04-Day Forecast, R003	182° to 183°	(236, 6) (245, 6) (245, 6) (244, 6)	4
04-Day Forecast, R005	181° to 183°	(243, 6) (243, 6) (240, 6) (238, 6) (247, 6)	5
04-Day Forecast, R003	182° to 183°	(236, 6) (245, 6) (245, 6) (244, 6)	4

Table B.1: Table of extracted magnetic footpoints modeled using ADAPT-WSA for SEP Event 1 on 11 October 2013. Each subtable presents the connectivity results for each of the observing spacecraft, STEREO A, STEREO B and ACE. Column 1: The selected forecast window and modeling realization. Column 2: The range of angular separations between the location of the associated solar flare and the modeled footpoints. Column 3: The set of extracted ADAPT-WSA modeled magnetic footpoints. Column 4: The number of footpoints comprising the extracted set for each forecast window and realization.

Event 3 ADAPT-WSA Modeled Magnetic Connectivity Results

Event 3 for STEREO A at 2014-05-02 05:33:00 (252, -8)

Forecast Window, Realization	Field Line to Flare Source Separation [deg.]	Field Line Footpoint Locations (long.,lat.)	Number of ADAPT-WSA Field Lines Comprising Results
04-Day Forecast, R000	17° to 18°	(226, 6) (226, 6) (224, 6) (225, 6) (226, 6) (224, 6)	6
04-Day Forecast, R002	17° to 18°	(226, 6) (226, 6) (224, 6) (225, 6) (226, 6) (224, 6)	6
04-Day Forecast, R003	17° to 17°	(226, 6) (224, 6) (225, 6) (226, 6)	4
04-Day Forecast, R007	17° to 18°	(224, 6) (224, 6) (225, 6) (226, 6) (224, 6) (223, 6)	6
04-Day Forecast, R010	17° to 18°	(226, 6) (224, 6) (225, 6) (226, 6) (224, 6) (223, 6)	6

Event 3 for STEREO B at 2014-05-02 05:32:00 (252, -8)

Forecast Window, Realization	Field Line to Flare Source Separation [deg.]	Field Line Footpoint Locations (long.,lat.)	Number of ADAPT-WSA Field Lines Comprising Results
03-Day Forecast, R001	5° to 6°	(273, 3) (270, 3) (268, 3) (266, 2) (273, 3)	5
03-Day Forecast, R004	5° to 6°	(273, 3) (273, 3) (268, 3) (266, 2) (273, 3)	5
03-Day Forecast, R005	5° to 6°	(273, 3) (270, 3) (268, 3) (266, 2) (273, 3)	5
03-Day Forecast, R006	5° to 6°	(275, 3) (275, 3) (272, 3) (270, 3) (268, 3) (266, 2) (275, 3)	7
03-Day Forecast, R007	5° to 6°	(273, 3) (270, 3) (268, 3) (266, 2) (275, 3) (273, 3) (273, 3)	7

Event 3 for ACE at N/A (252, -8)

Forecast Window, Realization	Field Line to Flare Source Separation [deg.]	Field Line Footpoint Locations (long.,lat.)	Number of ADAPT-WSA Field Lines Comprising Results
None	None	None	None
None	None	None	None
None	None	None	None
None	None	None	None
None	None	None	None

Table B.2: Table of extracted magnetic footpoints modeled using ADAPT-WSA for SEP Event 3 on 02 May 2014. Each subtable presents the connectivity results for each of the observing spacecraft, STEREO A, STEREO B and ACE. Column 1: The selected forecast window and modeling realization. Column 2: The range of angular separations between the location of the associated solar flare and the modeled footpoints. Column 3: The set of extracted ADAPT-WSA modeled magnetic footpoints. Column 4: The number of footpoints comprising the extracted set for each forecast window and realization.

Event 4 ADAPT-WSA Modeled Magnetic Connectivity Results

Event 4 for STEREO A at 2014-07-17 08:42:00 (272, 0)

Forecast Window, Realization	Field Line to Flare Source Separation [deg.]	Field Line Footpoint Locations (long.,lat.)	Number of ADAPT-WSA Field Lines Comprising Results
05-Day Forecast, R000	10° to 13°	(335, -2) (333, -2) (331, -2) (333, -2) (331, -2) (329, -2) (337, -2) (335, -2) (333, -2) (331, -2) (335, -2) (333, -2) (331, -2)	13
05-Day Forecast, R005	10° to 43°	(337, -2) (337, -2) (335, -2) (333, -2) (331, -2) (333, -2) (331, -2) (331, -2)	8
05-Day Forecast, R008	10° to 11°	(335, -2) (333, -2) (333, -2) (331, -2) (329, -2) (333, -2) (331, -2) (329, -2) (329, -2)	9
05-Day Forecast, R010	10° to 43°	(337, -2) (335, -2) (341, -2) (335, -2) (333, -2) (341, -2) (339, -2) (337, -2) (335, -2) (333, -2) (331, -2) (341, -2) (339, -2) (337, -2) (335, -2) (333, -2) (331, -2)	17
None	None	None	None

Event 4 for STEREO B at 2014-07-17 08:34:00 (272, 0)

Forecast Window, Realization	Field Line to Flare Source Separation [deg.]	Field Line Footpoint Locations (long.,lat.)	Number of ADAPT-WSA Field Lines Comprising Results
05-Day Forecast, R003	N/A		0
05-Day Forecast, R005	N/A		0
05-Day Forecast, R006	131° to 131°	(3, -5)	1
05-Day Forecast, R008	N/A		0
05-Day Forecast, R010	130° to 130°	(1, -5) (1, -5)	2

Event 4 for ACE at N/A (272, 0)

Forecast Window, Realization	Field Line to Flare Source Separation [deg.]	Field Line Footpoint Locations (long.,lat.)	Number of ADAPT-WSA Field Lines Comprising Results
None	None	None	None
None	None	None	None
None	None	None	None
None	None	None	None
None	None	None	None

Table B.3: Table of extracted magnetic footpoints modeled using ADAPT-WSA for SEP Event 4 on 17 July 2014. Each subtable presents the connectivity results for each of the observing spacecraft, STEREO A, STEREO B and ACE. Column 1: The selected forecast window and modeling realization. Column 2: The range of angular separations between the location of the associated solar flare and the modeled footpoints. Column 3: The set of extracted ADAPT-WSA modeled magnetic footpoints. Column 4: The number of footpoints comprising the extracted set for each forecast window and realization.

Event 5 ADAPT-WSA Modeled Magnetic Connectivity Results

Event 5 for STEREO A at 2014-08-01 16:34:00 (155, -22)

Forecast Window, Realization	Field Line to Flare Source Separation [deg.]	Field Line Footpoint Locations (long.,lat.)	Number of ADAPT-WSA Field Lines Comprising Results
05-Day Forecast, R002	36° to 37°	(108, -4) (107, -4) (105, -4) (108, -4) (106, -4) (108, -4) (106, -4)	7
05-Day Forecast, R003	36° to 36°	(107, -4) (108, -4) (108, -4)	3
05-Day Forecast, R007	36° to 36°	(110, -4) (107, -4) (108, -4) (110, -4) (108, -4) (107, -4)	6
05-Day Forecast, R010	36° to 37°	(107, -4) (105, -4) (108, -4) (106, -4) (108, -4) (105, -4)	6
05-Day Forecast, R011	36° to 37°	(109, -4) (108, -4) (106, -4) (106, -4)	4

Event 5 for STEREO B at 2014-08-01 16:54:00 (155, -22)

Forecast Window, Realization	Field Line to Flare Source Separation [deg.]	Field Line Footpoint Locations (long.,lat.)	Number of ADAPT-WSA Field Lines Comprising Results
04-Day Forecast, R000	35° to 36°	(159, -6) (157, -6)	2
04-Day Forecast, R003	37° to 37°	(159, -6) (157, -6)	2
04-Day Forecast, R005	35° to 36°	(162, -6) (160, -6)	2
04-Day Forecast, R006	34° to 35°	(159, -6) (157, -6) (155, -6) (159, -6) (157, -6)	5
04-Day Forecast, R011	35° to 36°	(160, -6) (155, -6)	2

Event 5 for ACE at 2014-08-01 18:00:00 (155, -22)

Forecast Window, Realization	Field Line to Flare Source Separation [deg.]	Field Line Footpoint Locations (long.,lat.)	Number of ADAPT-WSA Field Lines Comprising Results
04-Day Forecast, R001	113° to 119°	(321, 5) (306, 5) (315, 5) (313, 5) (311, 5) (309, 5) (307, 5) (305, 5) (303, 5) (301, 5) (311, 5) (309, 5) (307, 5) (305, 5) (303, 5)	15
04-Day Forecast, R003	113° to 119°	(321, 5) (306, 5) (315, 5) (313, 5) (311, 5) (309, 5) (307, 5) (305, 5) (303, 5) (301, 5) (311, 5) (309, 5) (307, 5) (305, 5) (303, 5)	15
04-Day Forecast, R005	113° to 119°	(321, 5) (315, 5) (313, 5) (311, 5) (309, 5) (307, 5) (305, 5) (303, 5) (301, 5) (311, 5) (309, 5) (307, 5) (305, 5) (303, 5)	14
04-Day Forecast, R006	113° to 119°	(306, 5) (317, 5) (315, 5) (313, 5) (311, 5) (309, 5) (307, 5) (305, 5) (303, 5) (301, 5) (311, 5) (309, 5) (307, 5) (305, 5) (303, 5)	15
04-Day Forecast, R008	113° to 119°	(321, 5) (306, 5) (317, 5) (315, 5) (313, 5) (311, 5) (309, 5) (307, 5) (305, 5) (303, 5) (301, 5) (311, 5) (309, 5) (307, 5) (305, 5) (303, 5)	16

Table B.4: Table of extracted magnetic footpoints modeled using ADAPT-WSA for SEP Event 5 on 01 August 2014. Each subtable presents the connectivity results for each of the observing spacecraft, STEREO A, STEREO B and ACE. Column 1: The selected forecast window and modeling realization. Column 2: The range of angular separations between the location of the associated solar flare and the modeled footpoints. Column 3: The set of extracted ADAPT-WSA modeled magnetic footpoints. Column 4: The number of footpoints comprising the extracted set for each forecast window and realization.

Event 6 ADAPT-WSA Modeled Magnetic Connectivity Results

Event 6 for STEREO A at 2014-08-01 23:45:00 (155, -22)

Forecast Window, Realization	Field Line to Flare Source Separation [deg.]	Field Line Footpoint Locations (long.,lat.)	Number of ADAPT-WSA Field Lines Comprising Results
05-Day Forecast, R002	37° to 37°	(103, -4) (104, -4) (104, -4) (103, -4)	4
05-Day Forecast, R003	36° to 37°	(105, -4) (106, -4) (106, -4) (105, -4) (103, -4) (106, -4)	6
05-Day Forecast, R007	37° to 37°	(105, -4) (106, -4) (106, -4) (105, -4)	4
05-Day Forecast, R010	37° to 37°	(104, -4) (104, -4) (103, -4)	3
05-Day Forecast, R011	36° to 37°	(107, -4) (104, -4) (102, -4) (104, -4) (107, -4)	5

Event 6 for STEREO B at 2014-08-01 23:54:00 (155, -22)

Forecast Window, Realization	Field Line to Flare Source Separation [deg.]	Field Line Footpoint Locations (long.,lat.)	Number of ADAPT-WSA Field Lines Comprising Results
04-Day Forecast, R000	9° to 38°	(157, -6) (155, -6) (149, -6) (147, -6)	4
04-Day Forecast, R003	10° to 40°	(162, -6) (147, -6) (145, -6)	3
04-Day Forecast, R005	9° to 40°	(159, -6) (157, -6) (155, -6) (153, -6) (160, -6) (147, -6)	6
04-Day Forecast, R006	10° to 10°	(145, -6) (143, -6) (141, -6)	3
04-Day Forecast, R011	8° to 41°	(158, -6) (166, -6) (164, -6) (162, -6) (160, -6) (158, -6) (156, -6) (154, -6) (152, -6) (150, -6) (148, -6) (146, -6) (159, -6) (157, -6) (155, -6) (153, -6) (151, -6)	17

Event 6 for ACE at 2014-08-01 00:00:00 (155, -22)

Forecast Window, Realization	Field Line to Flare Source Separation [deg.]	Field Line Footpoint Locations (long.,lat.)	Number of ADAPT-WSA Field Lines Comprising Results
04-Day Forecast, R001	119° to 151°	(319, 5) (334, 5) (332, 5) (330, 5) (328, 5) (326, 5) (324, 5) (322, 5) (320, 5) (322, 5) (320, 5) (347, 5) (345, 5) (343, 5) (341, 5) (339, 5) (337, 5) (335, 5) (333, 5) (331, 5) (329, 5) (327, 5) (325, 5) (324, 5)	24
04-Day Forecast, R003	119° to 122°	(319, 5) (344, 5) (342, 5) (340, 5) (322, 5) (320, 5) (343, 5) (341, 5) (339, 5) (337, 5) (335, 5) (333, 5) (331, 5) (329, 5) (327, 5) (325, 5)	16
04-Day Forecast, R005	118° to 122°	(319, 5) (322, 5) (320, 5) (322, 5) (320, 5) (345, 5) (343, 5) (341, 5) (339, 5) (337, 5) (335, 5) (333, 5) (331, 5) (329, 5) (327, 5) (325, 5) (324, 5)	17
04-Day Forecast, R006	118° to 122°	(319, 5) (322, 5) (320, 5) (322, 5) (343, 5) (341, 5) (339, 5) (337, 5) (335, 5) (333, 5) (331, 5) (329, 5) (327, 5) (325, 5)	14
04-Day Forecast, R008	118° to 122°	(319, 5) (344, 5) (342, 5) (340, 5) (338, 5) (336, 5) (334, 5) (332, 5) (330, 5) (328, 5) (326, 5) (324, 5) (322, 5) (320, 5) (322, 5) (320, 5) (343, 5) (341, 5) (339, 5) (337, 5) (335, 5) (333, 5) (331, 5) (329, 5) (327, 5) (325, 5) (324, 5) (322, 5)	28

Table B.5: Table of extracted magnetic footpoints modeled using ADAPT-WSA for SEP Event 6 on 01 August 2014. Each subtable presents the connectivity results for each of the observing spacecraft, STEREO A, STEREO B and ACE. Column 1: The selected forecast window and modeling realization. Column 2: The range of angular separations between the location of the associated solar flare and the modeled footpoints. Column 3: The set of extracted ADAPT-WSA modeled magnetic footpoints. Column 4: The number of footpoints comprising the extracted set for each forecast window and realization.

Comparison of ADAPT-WSA and Klassen et al. Modeled Magnetic Connectivity

Event 1: 11 Oct 2013

Spacecraft	ADAPT-WSA Mean (long.,lat.) Modeled at the Photosphere	ADAPT-WSA Range of (long.,lat.) Modeled at the Photosphere	Number of Modeled Footpoints Comprising Each Range	Klassen et al. (long.,lat.) Modeled at 2.5 R_s	ADAPT-WSA vs Klassen et al. Longitude Difference	ADAPT-WSA vs Klassen et al. Latitude Difference	ADAPT-WSA vs Klassen et al. Total Difference
SOHO/ACE	(264, -18)	(259, -22) to (265, -16)	18	(240, 6)	24°	24°	33°
STEREO A	(37, 13)	(37, 13) to (37, 13)	27	(40, -7)	3°	20°	21°
STEREO B: Cluster A STEREO B: Cluster B	(94, 21) (127, -22)	(90, 20) to (100, 23) (125, -23) to (128, -22)	81 4	(127, -2)	33° 0°	24° 20°	41° 20°

Event 2: 25 Feb 2014

Spacecraft	ADAPT-WSA Mean (long.,lat.) Modeled at the Photosphere	ADAPT-WSA Range of (long.,lat.) Modeled at the Photosphere	Number of Modeled Footpoints Comprising Each Range	Klassen et al. (long.,lat.) Modeled at 2.5 R_s	ADAPT-WSA vs Klassen et al. Longitude Difference	ADAPT-WSA vs Klassen et al. Latitude Difference	ADAPT-WSA vs Klassen et al. Total Difference
ACE: Cluster A ACE: Cluster B	(241, -16) (294, -14)	(237, -17) to (251, -10) (283, -22) to (296, -11)	44 12	(236, -7)	5° 58°	8° 7°	10° 58°
STEREO A: Cluster A STEREO A: Cluster B	(4, -12) (61, 17)	(2, -14) to (9, -12) (61, 17) to (61, 17)	54 1	(39, 6)	35° 22°	18° 11°	39° 24°
STEREO B	(65, 16)	(65, 16) to (66, 17)	34	(70, 7)	5°	9°	10°

Event 3: 02 May 2014

Spacecraft	ADAPT-WSA Mean (long.,lat.) Modeled at the Photosphere	ADAPT-WSA Range of (long.,lat.) Modeled at the Photosphere	Number of Modeled Footpoints Comprising Each Range	Klassen et al. (long.,lat.) Modeled at 2.5 R_s	ADAPT-WSA vs Klassen et al. Longitude Difference	ADAPT-WSA vs Klassen et al. Latitude Difference	ADAPT-WSA vs Klassen et al. Total Difference
SOHO/ACE	N/A	N/A	N/A	N/A	N/A	N/A	N/A
STEREO A	(235, -8)	(234, -8) to (235, -8)	28	(253, 6)	18°	14°	23°
STEREO B	(247, -11)	(246, -12) to (248, -10)	29	(300, 3)	53°	14°	54°

Event 4: 17 July 2014

Spacecraft	ADAPT-WSA Mean (long.,lat.) Modeled at the Photosphere	ADAPT-WSA Range of (long.,lat.) Modeled at the Photosphere	Number of Modeled Footpoints Comprising Each Range	Klassen et al. (long.,lat.) Modeled at 2.5 R_s	ADAPT-WSA vs Klassen et al. Longitude Difference	ADAPT-WSA vs Klassen et al. Latitude Difference	ADAPT-WSA vs Klassen et al. Total Difference
SOHO/ACE	N/A	N/A	N/A	(169, 4)	N/A	N/A	N/A
STEREO A: Cluster A STEREO A: Cluster B	(270, -11) (314, 11)	(268, -13) to (273, -10) (313, 10) to (314, 11)	44 3	(338, -3)	68° 24°	8° 13°	69° 28°
STEREO B	(42, -11)	(41, -12) to (42, -11)	3	(0, -6)	42°	5°	42°

Event 5: 01 Aug 2014

Spacecraft	ADAPT-WSA Mean (long.,lat.) Modeled at the Photosphere	ADAPT-WSA Range of (long.,lat.) Modeled at the Photosphere	Number of Modeled Footpoints Comprising Each Range	Klassen et al. (long.,lat.) Modeled at 2.5 R_s	ADAPT-WSA vs Klassen et al. Longitude Difference	ADAPT-WSA vs Klassen et al. Latitude Difference	ADAPT-WSA vs Klassen et al. Total Difference
SOHO/ACE	(271, -10)	(267, -11) to (274, -9)	75	(332, 6)	61°	16°	63°
STEREO A	(120, -32)	(120, -32) to (121, -31)	26	(133, -5)	13°	27°	30°
STEREO B	(188, -34)	(182, -45) to (191, -30)	13	(143, -7)	45°	27°	53°

Event 6: 01 Aug 2014

Spacecraft	ADAPT-WSA Mean (long.,lat.) Modeled at the Photosphere	ADAPT-WSA Range of (long.,lat.) Modeled at the Photosphere	Number of Modeled Footpoints Comprising Each Range	Klassen et al. (long.,lat.) Modeled at 2.5 R_s	ADAPT-WSA vs Klassen et al. Longitude Difference	ADAPT-WSA vs Klassen et al. Latitude Difference	ADAPT-WSA vs Klassen et al. Total Difference
SOHO/ACE	(275, -12) (8, 11)	(273, -13) to (277, -11) (8, 11) to (8, 11)	98 1	(318, 6)	43° 50°	18° 6°	47° 51°
STEREO A	(120, -31)	(119, -32) to (120, -31)	22	(133, -5)	13°	27°	30°
STEREO B: Cluster A STEREO B: Cluster B	(153, -13) (191, -33)	(152, -14) to (153, -12) (187, -37) to (195, -29)	23 10	(137, -7)	16° 54°	6° 26°	17° 60°

Table B.6: Table of ADAPT-WSA modeled photospheric footpoints for SEP Events 1 - 6 observed by STEREO A and B in 2013-2014 compared to the Klassen et al. magnetic connectivity using the Parker spiral approximation 2015; 2016; 2018. Column 1: Observing spacecraft. Column 2: Mean ADAPT-WSA footpoint location at the photosphere. Column 3: Range of ADAPT-WSA footpoint locations at the photosphere. Column 4: The number of modeled footpoints that comprised the range of ADAPT-WSA results for the set of extracted modeled footpoints for that spacecraft. Column 5: Klassen at al. modeled footpoints at the 2.5 R_S PFSS using the Parker spiral approximation 2015; 2016; 2018. Column 6: Longitude difference between the ADAPT-WSA mean 5 R_S footpoints and the corresponding Klassen et al. 2.5 R_S footpoints.

Comparison of SEP and Flare Arrivals and Locations

Event 1: Oct 11 2013

Spacecraft	Photospheric Flare Location (long.,lat.)	ADAPT-WSA Mean Modeled Connectivity at 5 R_s (long.,lat.)	ADAPT-WSA Flare-Connectivity Longitude, Total Difference	Klassen et al. Connectivity at 2.5 R_s (long.,lat.)	Klassen et al. Flare-Connectivity Longitude, Total Difference	Observed EUV Flare Arrival Time	Observed SEP Arrival Time	Flare-SEP Arrival Time Diff.
SOHO/ACE	(83, 21)	(242, 6)	159°, 160°	(240, 6.0)	157°, 158°	07:11 UT	11:10 UT	239 minutes
STEREOA	(83, 21)	(32, -7)	51°, 58°	(40, -7.3)	43°, 51°	07:11 UT	07:34 UT	23 minutes
STEREOB	(83, 21)	(106, -3)	23°, 34°	(127, -2.5)	44°, 50°	07:11 UT	07:47 UT	36 minutes

Event 2: Feb 25 2014

Spacecraft	Photospheric Flare Location (long.,lat.)	ADAPT-WSA Mean Modeled Connectivity at 5 R_s (long.,lat.)	ADAPT-WSA Flare-Connectivity Longitude, Total Difference	Klassen et al. Connectivity at 2.5 R_s (long.,lat.)	Klassen et al. Flare-Connectivity Longitude, Total Difference	Observed EUV Flare Arrival Time	Observed SEP Arrival Time	Flare-SEP Arrival Time Diff.
SOHO/ACE	(108, -13)	(246, -7)	138°, 138°	(236, -7.1)	128°, 128°	00:46 UT	02:04 UT	78 minutes
STEREOA	(108, -13)	(35, 6)	73°, 76°	(39, 5.9)	69°, 72°	00:46 UT	01:09 UT	23 minutes
STEREOB	(108, -13)	(60, 7)	48°, 52°	(70, 7.2)	38°, 43°	00:46 UT	01:22 UT	36 minutes

Event 3: May 2 2014

Spacecraft	Photospheric Flare Location (long.,lat.)	ADAPT-WSA Mean Modeled Connectivity at 5 R_s (long.,lat.)	ADAPT-WSA Flare-Connectivity Longitude, Total Difference	Klassen et al. Connectivity at 2.5 R_s (long.,lat.)	Klassen et al. Flare-Connectivity Longitude, Total Difference	Observed EUV Flare Arrival Time	Observed SEP Arrival Time	Flare-SEP Arrival Time Diff.
SOHO/ACE	(250, -8)	N/A	N/A	N/A	N/A	05:09 UT	N/A	N/A
STEREOA	(250, -8)	(225, 6)	25°, 29°	(253, 6.1)	3°, 14°	05:09 UT	05:33 UT	24 minutes
STEREOB	(250, -8)	(271, 3)	21°, 24°	(300, 2.7)	50°, 51°	05:09 UT	05:32 UT	23 minutes

Event 4: July 17 2014

Spacecraft	Photospheric Flare Location (long.,lat.)	ADAPT-WSA Mean Modeled Connectivity at 5 R_s (long.,lat.)	ADAPT-WSA Flare-Connectivity Longitude, Total Difference	Klassen et al. Connectivity at 2.5 R_s (long.,lat.)	Klassen et al. Flare-Connectivity Longitude, Total Difference	Observed EUV Flare Arrival Time	Observed SEP Arrival Time	Flare-SEP Arrival Time Diff.
SOHO/ACE	(270, -10)	N/A	N/A	(169, 4.5)	101°, 102°	08:08 UT	N/A	N/A
STEREOA	(270, -10)	(334, -2)	64°, 64°	(338, -2.8)	68°, 68°	08:08 UT	08:42 UT	34 minutes
STEREOB	(270, -10)	(2, -6)	92°, 92°	(0, -5.9)	90°, 90°	08:08 UT	08:34 UT	26 minutes

Event 5: Aug 01 2014

Spacecraft	Photospheric Flare Location (long.,lat.)	ADAPT-WSA Mean Modeled Connectivity at 5 R_s (long.,lat.)	ADAPT-WSA Flare-Connectivity Longitude, Total Difference	Klassen et al. Connectivity at 2.5 R_s (long.,lat.)	Klassen et al. Flare-Connectivity Longitude, Total Difference	Observed EUV Flare Arrival Time	Observed SEP Arrival Time	Flare-SEP Arrival Time Diff.
SOHO/ACE	(155, -22)	(308, 6)	153°, 156°	(332, 5.8)	177°, 179°	16:13 UT	N/A	N/A
STEREOA	(155, -22)	(107, -4)	48°, 51°	(133, -4.6)	22°, 28°	16:13 UT	16:34 UT	21 minutes
STEREOB	(155, -22)	(158, -7)	3°, 16°	(143, -6.8)	12°, 19°	16:13 UT	16:54 UT	41 minutes

Event 6: Aug 01 2014

Spacecraft	Photospheric Flare Location (long.,lat.)	ADAPT-WSA Mean Modeled Connectivity at 5 R_s (long.,lat.)	ADAPT-WSA Flare-Connectivity Longitude, Total Difference	Klassen et al. Connectivity at 2.5 R_s (long.,lat.)	Klassen et al. Flare-Connectivity Longitude, Total Difference	Observed EUV Flare Arrival Time	Observed SEP Arrival Time	Flare-SEP Arrival Time Diff.
SOHO/ACE	(155, -22)	(331, 5)	176°, 178°	(318, 5.8)	163°, 165°	23:24 UT	N/A	N/A
STEREOA	(155, -22)	(105, -4)	50°, 53°	(133, -4.6)	22°, 28°	23:24 UT	23:45 UT	21 minutes
STEREOB	(155, -22)	(154, -7)	1°, 15°	(137, -6.8)	18°, 24°	23:24 UT	23:54 UT	30 minutes

Table B.7: Table of ADAPT-WSA modeled 5 R_S PFSS footpoints for SEP Events 1 - 6 compared to the associated Solar flare locations and the Klassen et al. magnetic connectivity using the Parker spiral approximation 2015; 2016; 2018. Column 1: Observing spacecraft. Column 2: Photospheric longitude and latitude of the associated solar flare *Klassen et al.* (2015, 2016, 2018). Column 3: Mean ADAPT-WSA footpoint location at the 5 R_S PFSS. Column 4: Longitude difference and total angular difference between the flare location and the ADAPT-WSA modeled 5 R_S PFSS footpoint. Column 5: Klassen et al. 2.5 R_S footpoint locations *Klassen et al.* (2015, 2016, 2018). Column 6: Longitude difference and total angular difference between the flare location and the Klassen et al. modeled 2.5 R_S PFSS footpoint. Column 7: Arrival time of associated observed EUV solar flare. Column 8: Observed electron event arrival time at the observing spacecraft. Column 9: Difference in EUV solar flare and electron event arrival times.

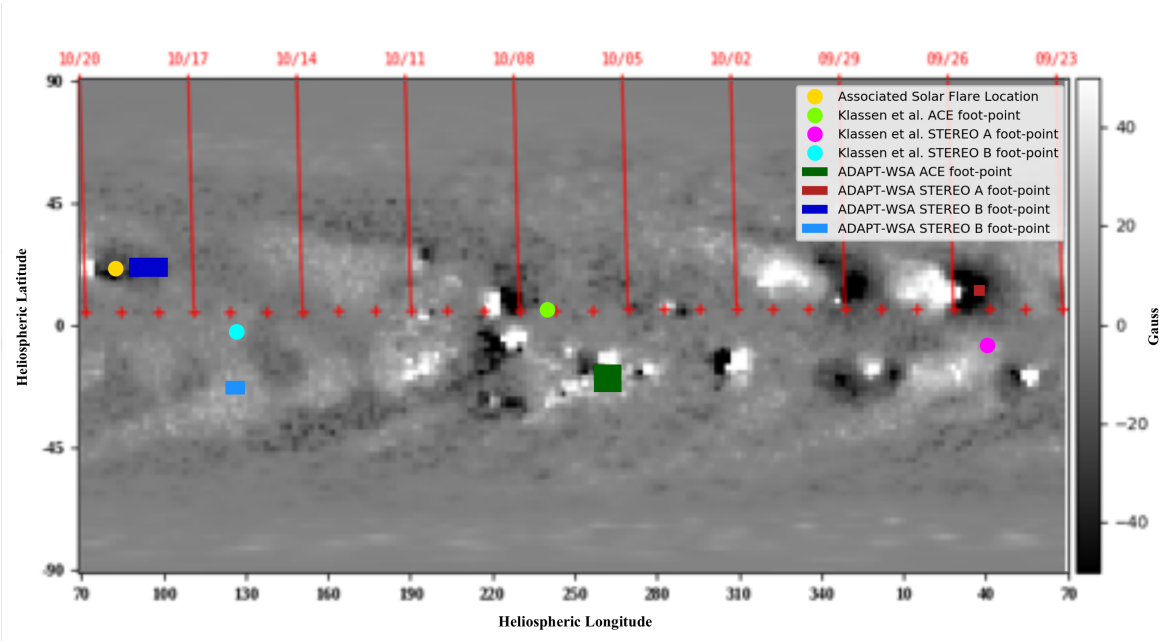

Figure B.4: Map of SEP Event 1 ADAPT-WSA modeled photospheric footpoints and Klassen et al. 2.5 R_S footpoints 2016. These modeled footpoints are overlaid on a photospheric synoptic magnetic field map from ground-based GONG magnetograms. Coordinates are in heliospheric latitude and Carrington longitude. The solar equator is at 0° latitude and the Earth ecliptic plane is marked by red plus symbols. Vertical red lines mark the central meridians, labeled with the corresponding observational dates, of the GONG magnetograms that form the composite synoptic map.

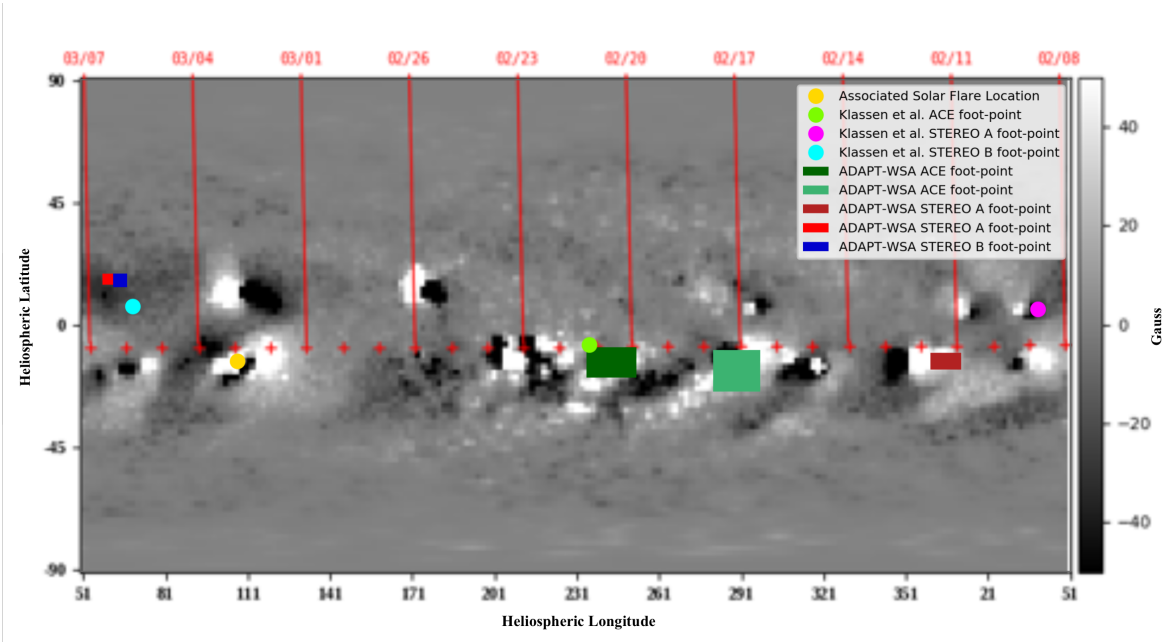

Figure B.5: Map of SEP Event 2 ADAPT-WSA modeled photospheric footpoints and Klassen et al. 2.5 R_S footpoints 2016. These modeled footpoints are overlaid on a photospheric synoptic magnetic field map from ground-based GONG magnetograms. Coordinates are in heliospheric latitude and Carrington longitude. The solar equator is at 0° latitude and the Earth ecliptic plane is marked by red plus symbols. Vertical red lines mark the central meridians, labeled with the corresponding observational dates, of the GONG magnetograms that form the composite synoptic map.

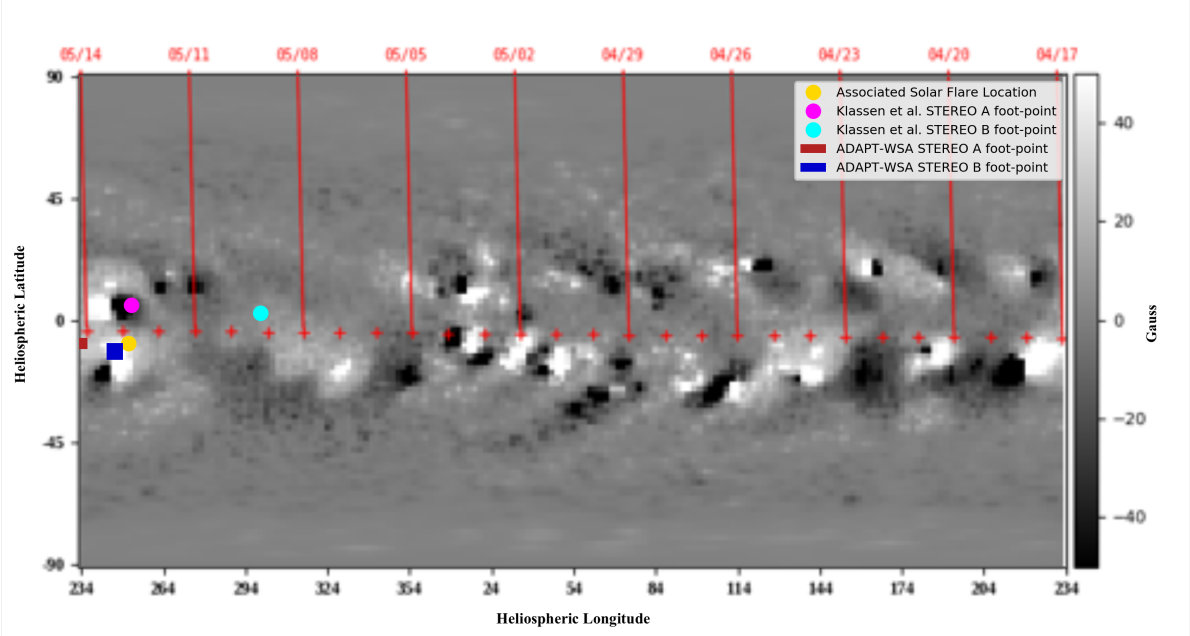

Figure B.6: Map of SEP Event 3 ADAPT-WSA modeled photospheric footpoints and Klassen et al. 2.5 R_S footpoints 2016. These modeled footpoints are overlaid on a photospheric synoptic magnetic field map from ground-based GONG magnetograms. Coordinates are in heliospheric latitude and Carrington longitude. The solar equator is at 0° latitude and the Earth ecliptic plane is marked by red plus symbols. Vertical red lines mark the central meridians, labeled with the corresponding observational dates, of the GONG magnetograms that form the composite synoptic map.

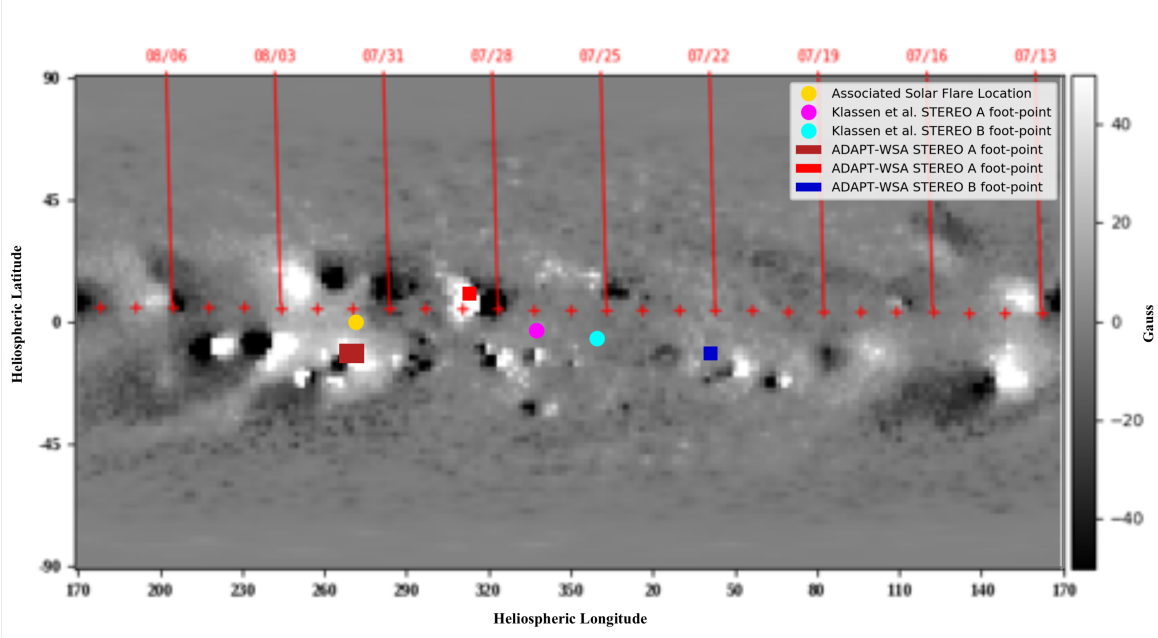

Figure B.7: Map of SEP Event 4 ADAPT-WSA modeled photospheric footpoints and Klassen et al. 2.5 R_S footpoints 2016. These modeled footpoints are overlaid on a photospheric synoptic magnetic field map from ground-based GONG magnetograms. Coordinates are in heliospheric latitude and Carrington longitude. The solar equator is at 0° latitude and the Earth ecliptic plane is marked by red plus symbols. Vertical red lines mark the central meridians, labeled with the corresponding observational dates, of the GONG magnetograms that form the composite synoptic map.

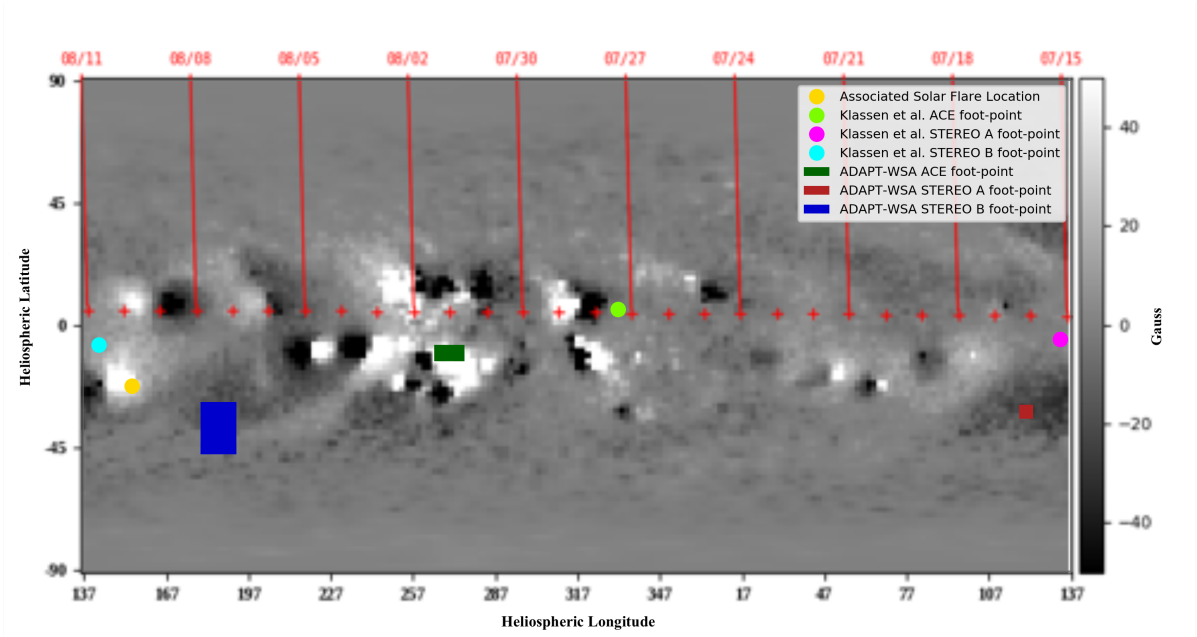

Figure B.8: Map of SEP Event 5 ADAPT-WSA modeled photospheric footpoints and Klassen et al. 2.5 R_S footpoints 2016. These modeled footpoints are overlaid on a photospheric synoptic magnetic field map from ground-based GONG magnetograms. Coordinates are in heliospheric latitude and Carrington longitude. The solar equator is at 0° latitude and the Earth ecliptic plane is marked by red plus symbols. Vertical red lines mark the central meridians, labeled with the corresponding observational dates, of the GONG magnetograms that form the composite synoptic map.

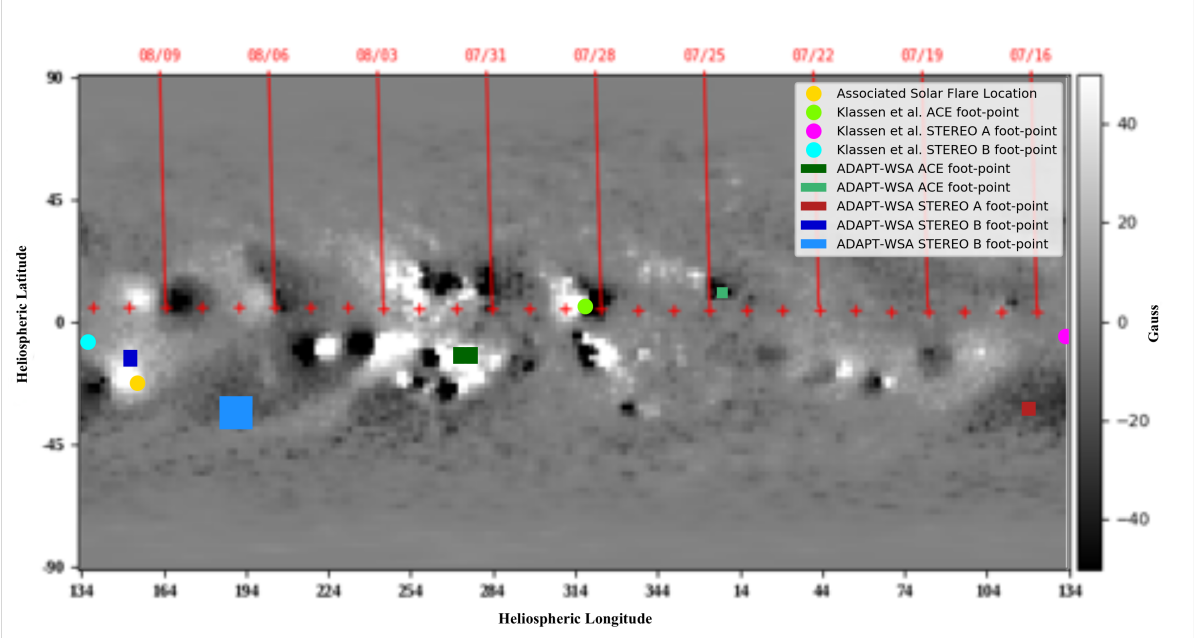

Figure B.9: Map of SEP Event 6 ADAPT-WSA modeled photospheric footpoints and Klassen et al. 2.5 R_S footpoints 2016. These modeled footpoints are overlaid on a photospheric synoptic magnetic field map from ground-based GONG magnetograms. Coordinates are in heliospheric latitude and Carrington longitude. The solar equator is at 0° latitude and the Earth ecliptic plane is marked by red plus symbols. Vertical red lines mark the central meridians, labeled with the corresponding observational dates, of the GONG magnetograms that form the composite synoptic map.

BIBLIOGRAPHY

BIBLIOGRAPHY

Alfvén, H. (1950), *Cosmic electrodynamics*, Clarendon Press.

Anderson, B., R. Skoug, J. Steinberg, and D. McComas (2012), Variability of the solar wind suprathermal electron strahl, *Journal of Geophysical Research: Space Physics*, *117*(A4).

Arge, C., and V. Pizzo (2000), Improvement in the prediction of solar wind conditions using near-real time solar magnetic field updates, *Journal of Geophysical Research: Space Physics*, *105*(A5), 10,465–10,479.

Arge, C., C. Henney, K. Shurkin, W. Toussaint, J. Koller, and J. Harvey (2011), Comparing adapt-wsa model predictions with euv and solar wind observations, in *Bulletin of the American Astronomical Society*, vol. 43.

Arge, C. N., C. J. Henney, J. Koller, C. R. Compeau, S. Young, D. MacKenzie, A. Fay, and J. W. Harvey (2010), Air Force Data Assimilative Photospheric Flux Transport (ADAPT) Model, in *Twelfth International Solar Wind Conference*, *American Institute of Physics Conference Series*, vol. 1216, edited by M. Maksimovic, K. Issautier, N. Meyer-Vernet, M. Moncuquet, and F. Pantellini, pp. 343–346.

Aschwanden, M. J., et al. (2017), Global energetics of solar flares. v. energy closure in flares and coronal mass ejections, *The Astrophysical Journal*, *836*(1), 17.

Bougeret, J.-L., et al. (2008), S/waves: The radio and plasma wave investigation on the stereo mission, *Space Science Reviews*, *136*(1-4), 487–528.

Bučík, R., D. E. Innes, G. M. Mason, M. E. Wiedenbeck, R. Gómez-Herrero, and N. V. Nitta (2018), 3he-rich solar energetic particles in helical jets on the sun, *The Astrophysical Journal*, *852*(2), 76.

Cane, H., and I. Richardson (2003), Interplanetary coronal mass ejections in the near-earth solar wind during 1996–2002, *Journal of Geophysical Research: Space Physics*, *108*(A4).

Case, A. W., et al. (2020), The solar probe cup on the parker solar probe, *The Astrophysical Journal Supplement Series*, *246*(2), 43.

Cash, M. D., H. J. Singer, G. H. Millward, C. C. Balch, G. Toth, and D. T. Welling (2017), Space Weather Forecasting at NOAA with Michigan's Geospace Model: Results from the First Year in Real-Time Operations, in *AGU Fall Meeting Abstracts*, vol. 2017, pp. SM11E–07.

Chollet, E., J. Giacalone, and R. Mewaldt (2010), Effects of interplanetary transport on derived energetic particle source strengths, *Journal of Geophysical Research: Space Physics*, *115*(A6).

Cohen, C. (2016), Current understanding of sep acceleration and transport, in *AIP Conference Proceedings*, vol. 1720, p. 060001, AIP Publishing LLC.

Cohen, C., G. Mason, and R. Mewaldt (2017), Characteristics of solar energetic ions as a function of longitude, *The Astrophysical Journal*, *843*(2), 132.

Crooker, N., J. Gosling, and S. Kahler (2002), Reducing heliospheric magnetic flux from coronal mass ejections without disconnection, *Journal of Geophysical Research: Space Physics*, *107*(A2), SSH–3.

Crosby, N., et al. (2015), Sepem: A tool for statistical modeling the solar energetic particle environment, *Space Weather*, *13*(7), 406–426.

De Koning, C., J. Gosling, R. Skoug, and J. Steinberg (2007), Energy dependence of electron pitch angle distribution widths in solar bursts, *Journal of Geophysical Research: Space Physics*, *112*(A4).

De Koning, C. A., J. Gosling, R. M. Skoug, and J. T. Steinberg (2006), Widths of suprathermal pitch angle distributions during solar electron bursts: Ace observations, *Journal of Geophysical Research: Space Physics*, *111*(A4).

Desai, M., and J. Giacalone (2016), Large gradual solar energetic particle events, *Living Reviews in Solar Physics*, *13*(1), 3.

Dresing, N., R. Gómez-Herrero, B. Heber, A. Klassen, O. Malandraki, W. Dröge, and Y. Kartavykh (2014), Statistical survey of widely spread out solar electron events observed with stereo and ace with special attention to anisotropies, *Astronomy & Astrophysics*, *567*, A27.

Einstein, A., and L. Infeld (1961), *The Evolution of Physics, Etc.[Edited by Leopold Infeld.]*., Simon & Schuster.

Feldman, W., J. Asbridge, S. Bame, M. Montgomery, and S. Gary (1975), Solar wind electrons, *Journal of Geophysical Research*, *80*(31), 4181–4196.

Feldman, W., R. Anderson, J. Asbridge, S. Bame, J. Gosling, and R. Zwickl (1982), Plasma electron signature of magnetic connection to the earth's bow shock: Isee 3, *Journal of Geophysical Research: Space Physics*, *87*(A2), 632–642.

Ferri, C., J. Hernández-Orallo, and P. A. Flach (2011), A coherent interpretation of auc as a measure of aggregated classification performance, in *Proceedings of the 28th International Conference on Machine Learning (ICML-11)*, pp. 657–664.

Fitzenreiter, R., K. Ogilvie, D. Chornay, and J. Keller (1998), Observations of electron velocity distribution functions in the solar wind by the wind spacecraft: High angular resolution strahl measurements, *Geophysical research letters*, *25*(3), 249–252.

Gary, S. P., and H. Li (2000), Whistler heat flux instability at high beta, *The Astrophysical Journal*, *529*(2), 1131.

Gilbert, J., S. T. Lepri, E. Landi, and T. H. Zurbuchen (2012), First measurements of the complete heavy-ion charge state distributions of c, o, and fe associated with interplanetary coronal mass ejections, *The Astrophysical Journal*, *751*(1), 20.

Gloeckler, G., et al. (1998), Investigation of the composition of solar and interstellar matter using solar wind and pickup ion measurements with swics and swims on the ace spacecraft, in *The advanced composition explorer mission*, pp. 497–539, Springer.

Gopalswamy, N., M. Shimojo, W. Lu, S. Yashiro, K. Shibasaki, and R. Howard (2003), Prominence eruptions and coronal mass ejection: a statistical study using microwave observations, *The Astrophysical Journal*, *586*(1), 562.

Gosling, J., and D. McComas (1987), Field line draping about fast coronal mass ejecta: A source of strong out-of-the-ecliptic interplanetary magnetic fields, *Geophysical research letters*, *14*(4), 355–358.

Gosling, J., and R. Skoug (2002), On the origin of radial magnetic fields in the heliosphere, *Journal of Geophysical Research: Space Physics*, *107*(A10), SSH–19.

Gosling, J., D. Baker, S. Bame, W. Feldman, R. Zwickl, and E. Smith (1987), Bidirectional solar wind electron heat flux events, *Journal of Geophysical Research: Space Physics*, *92*(A8), 8519–8535.

Gosling, J., R. Skoug, and W. Feldman (2001), Solar wind electron halo depletions at 90 pitch angle, *Geophysical research letters*, *28*(22), 4155–4158.

Gosling, J. T. (1990), Coronal mass ejections and magnetic flux ropes in interplanetary space, *Physics of magnetic flux ropes*, *58*, 343–364.

Gosling, J. T. (1993), The solar flare myth, *Journal of Geophysical Research: Space Physics*, *98*(A11), 18,937–18,949.

Gosling, J. T. (2014), The solar wind, in *Encyclopedia of the solar system*, pp. 261–279, Elsevier.

Gruesbeck, J. R., S. T. Lepri, T. H. Zurbuchen, and S. K. Antiochos (2011), Constraints on coronal mass ejection evolution from in situ observations of ionic charge states, *The Astrophysical Journal*, *730*(2), 103.

Gruesbeck, J. R., S. T. Lepri, and T. H. Zurbuchen (2012), Two-plasma model for low charge state interplanetary coronal mass ejection observations, *The Astrophysical Journal*, *760*(2), 141.

Haggerty, D. K., and E. C. Roelof (2009), Probing sep acceleration processes with near-relativistic electrons, in *AIP Conference Proceedings*, vol. 1183, pp. 3–10, American Institute of Physics.

Haixiang, G., L. Yijing, J. Shang, G. Mingyun, H. Yuanyue, and G. Bing (2017), Learning from class-imbalanced data: Review of methods and applications, *Expert Systems with Applications*, *73*, 220–239.

Halekas, J., et al. (2020), Electrons in the young solar wind: First results from the parker solar probe, *The Astrophysical Journal Supplement Series*, *246*(2), 22.

Howard, R. A., et al. (2008), Sun earth connection coronal and heliospheric investigation (secchi), *Space Science Reviews*, *136*(1-4), 67.

Hundhausen, A., H. Gilbert, and S. Bame (1968), Ionization state of the interplanetary plasma, *Journal of Geophysical Research*, *73*(17), 5485–5493.

Jian, L. K., C. T. Russell, J. G. Luhmann, and R. M. Skoug (2006), Properties of interplanetary coronal mass ejections at one au during 1995–2004, *Solar Physics*, *239*(1-2), 393–436.

Jian, L. K., C. T. Russell, and J. G. Luhmann (2011), Comparing solar minimum 23/24 with historical solar wind records at 1 au, *Solar Physics*, *274*(1-2), 321–344.

Kahler, S. (2007), Solar sources of heliospheric energetic electron events—shocks or flares?, *Space science reviews*, *129*(4), 359–390.

Kahler, S., and A. Vourlidas (2013), A comparison of the intensities and energies of gradual solar energetic particle events with the dynamical properties of associated coronal mass ejections, *The Astrophysical Journal*, *769*(2), 143.

Kahler, S., and A. Vourlidas (2014a), Do interacting coronal mass ejections play a role in solar energetic particle events?, *The Astrophysical Journal*, *784*(1), 47.

Kahler, S., H. Aurass, G. Mann, and A. Klassen (2007), Solar radio burst and solar wind associations with inferred near-relativistic electron injections, *The Astrophysical Journal*, *656*(1), 567.

Kahler, S., D. Haggerty, and I. Richardson (2011), Magnetic field-line lengths in interplanetary coronal mass ejections inferred from energetic electron events, *The Astrophysical Journal*, *736*(2), 106.

Kahler, S., C. Arge, and D. A. Smith (2016), Using the wsa model to test the parker spiral approximation for sep event magnetic connections, *Solar Physics*, *291*(6), 1829–1852.

Kahler, S. W., and A. G. Ling (2017), Characterizing solar energetic particle event profiles with two-parameter fits, *Solar Physics*, *292*(4), 59.

Kahler, S. W., and A. G. Ling (2018a), Forecasting solar energetic particle (sep) events with flare x-ray peak ratios, *Journal of Space Weather and Space Climate*, *8*, A47.

Kahler, S. W., and A. G. Ling (2018b), Relating solar energetic particle event fluences to peak intensities, *Solar Physics*, *293*(2), 30.

Kahler, S. W., and A. Vourlidas (2014b), Solar energetic particle events in different types of solar wind, *The Astrophysical Journal*, *791*(1), 4.

Kahler, S. W., S. M. White, and A. G. Ling (2017), Forecasting e¿ 50-mev proton events with the proton prediction system (pps), *Journal of Space Weather and Space Climate*, *7*, A27.

Klassen, A., R. Gómez-Herrero, and B. Heber (2011), Electron spikes, type iii radio bursts and euv jets on 22 february 2010, in *Energy Storage and Release through the Solar Activity Cycle*, pp. 107–113, Springer.

Klassen, A., R. Gómez-Herrero, B. Heber, Y. Kartavykh, W. Dröge, and K.-L. Klein (2012), Solar origin of in-situ near-relativistic electron spikes observed with sept/stereo, *Astronomy & Astrophysics*, *542*, A28.

Klassen, A., N. Dresing, R. Gómez-Herrero, and B. Heber (2015), First simultaneous observations of a near-relativistic electron spike event by both stereo spacecraft, *Astronomy & Astrophysics*, *580*, A115.

Klassen, A., N. Dresing, R. Gómez-Herrero, B. Heber, and R. Müller-Mellin (2016), Unexpected spatial intensity distributions and onset timing of solar electron events observed by closely spaced stereo spacecraft, *Astronomy & Astrophysics*, *593*, A31.

Klassen, A., N. Dresing, R. Gómez-Herrero, B. Heber, and A. Veronig (2018), Strong non-radial propagation of energetic electrons in solar corona, *Astronomy & Astrophysics*, *614*, A61.

Ko, Y.-K., L. A. Fisk, J. Geiss, G. Gloeckler, and M. Guhathakurta (1997), An empirical study of the electron temperature and heavy ion velocities in the south polar coronal hole, *Solar Physics*, *171*(2), 345–361.

Kozyra, J., W. Manchester IV, C. Escoubet, S. Lepri, M. Liemohn, W. Gonzalez, M. Thomsen, and B. Tsurutani (2013), Earth's collision with a solar filament on 21 january 2005: Overview, *Journal of Geophysical Research: Space Physics*, *118*(10), 5967–5978.

Lachiche, N., and P. A. Flach (2003), Improving accuracy and cost of two-class and multi-class probabilistic classifiers using roc curves, in *Proceedings of the 20th International Conference on Machine Learning (ICML-03)*, pp. 416–423.

Laitinen, T., and S. Dalla (2017), Energetic particle transport across the mean magnetic field: before diffusion, *The Astrophysical Journal*, *834*(2), 127.

Landi, E., R. Alexander, J. Gruesbeck, J. Gilbert, S. T. Lepri, W. Manchester, and T. H. Zurbuchen (2012), Carbon ionization stages as a diagnostic of the solar wind, *The Astrophysical Journal*, *744*(2), 100.

Lario, D., E. Roelof, and R. Decker (2014), Longitudinal dependence of sep peak intensities as evidence of cme-driven shock particle acceleration, in *Outstanding Problems in Heliophysics: from Coronal Heating to the Edge of the Heliosphere*, vol. 484, p. 98.

Lepri, S., and T. Zurbuchen (2004), Iron charge state distributions as an indicator of hot icmes: Possible sources and temporal and spatial variations during solar maximum, *Journal of Geophysical Research: Space Physics*, *109*(A1).

Lepri, S., and T. Zurbuchen (2010), Direct observational evidence of filament material within interplanetary coronal mass ejections, *The Astrophysical Journal Letters*, *723*(1), L22.

Lepri, S., T. Zurbuchen, L. Fisk, I. Richardson, H. Cane, and G. Gloeckler (2001), Iron charge distribution as an identifier of interplanetary coronal mass ejections, *Journal of Geophysical Research: Space Physics*, *106*(A12), 29,231–29,238.

Lin, R. (1970), The emission and propagation of 40kev solar flare electrons, *Solar Physics*, *12*(2), 266–303.

Lin, R. (1985), Energetic solar electrons in the interplanetary medium, *Solar physics*, *100*(1-2), 537–561.

Lynch, B., et al. (2011), Ionic composition structure of coronal mass ejections in axisymmetric magnetohydrodynamic models, *The Astrophysical Journal*, *740*(2), 112.

McComas, D., S. Bame, P. Barker, W. Feldman, J. Phillips, P. Riley, and J. Griffee (1998), Solar wind electron proton alpha monitor (swepam) for the advanced composition explorer, in *The Advanced Composition Explorer Mission*, pp. 563–612, Springer.

Mewaldt, R., et al. (2008), How efficient are coronal mass ejections at accelerating solar energetic particles?, in *AIP Conference Proceedings*, vol. 1039, pp. 111–117, American Institute of Physics.

Müller-Mellin, R., S. Böttcher, J. Falenski, E. Rode, L. Duvet, T. Sanderson, B. Butler, B. Johlander, and H. Smit (2008), The solar electron and proton telescope for the stereo mission, in *The STEREO Mission*, pp. 363–389, Springer.

Munro, R., J. Gosling, E. Hildner, R. MacQueen, A. Poland, and C. Ross (1979), The association of coronal mass ejection transients with other forms of solar activity, *Solar Physics*, *61*(1), 201–215.

National Science and Technology Council (2015), National space weather strategy.

Nitta, N. V., D. V. Reames, M. L. DeRosa, Y. Liu, S. Yashiro, and N. Gopalswamy (2006), Solar sources of impulsive solar energetic particle events and their magnetic field connection to the earth, *Astrophys. J*, *650*(1), 438–450.

Ogilvie, K., L. Burlaga, D. Chornay, and R. Fitzenreiter (1999), Sources of the solar wind electron strahl in 1995, *Journal of Geophysical Research: Space Physics*, *104*(A10), 22,389–22,393.

Ogilvie, K. W., R. Fitzenreiter, and M. Desch (2000), Electrons in the low-density solar wind, *Journal of Geophysical Research: Space Physics*, *105*(A12), 27,277–27,288.

Owens, M. J., and R. J. Forsyth (2013), The heliospheric magnetic field, *Living Reviews in Solar Physics*, *10*(1), 5.

Pagel, C., S. P. Gary, C. A. De Koning, R. M. Skoug, and J. T. Steinberg (2007), Scattering of suprathermal electrons in the solar wind: Ace observations, *Journal of Geophysical Research: Space Physics*, *112*(A4).

Parker, E. (1959), Extension of the Solar Corona into Interplanetary Space, *J. Geophys. Res.*, *64*, 1675–1681.

Pilipp, W., H. Miggenrieder, M. Montgomery, K.-H. Mühlhäuser, H. Rosenbauer, and R. Schwenn (1987a), Unusual electron distribution functions in the solar wind derived from the helios plasma experiment: Double-strahl distributions and distributions with an extremely anisotropic core, *Journal of Geophysical Research: Space Physics*, *92*(A2), 1093–1101.

Pilipp, W., H. Miggenrieder, K. Mühlhäuser, H. Rosenbauer, R. Schwenn, and F. Neubauer (1987b), Variations of electron distribution functions in the solar wind, *J. Geophys. Res*, *92*, 1103–1118.

Provost, F., and T. Fawcett (2001), Robust classification for imprecise environments, *Machine learning*, *42*(3), 203–231.

Ragot, B. (2006), Lengths of wandering magnetic field lines in the turbulent solar wind, *The Astrophysical Journal*, *653*(2), 1493.

Rakowski, C. E., J. M. Laming, and S. T. Lepri (2007), Ion charge states in halo coronal mass ejections: What can we learn about the explosion?, *The Astrophysical Journal*, *667*(1), 602.

Reames, D. V. (2013), The two sources of solar energetic particles, *Space Science Reviews*, *175*(1-4), 53–92.

Reames, D. V. (2018), The "fip effect" and the origins of solar energetic particles and of the solar wind, *Solar Physics*, *293*(3), 47.

Richardson, I. G. (2004), Energetic particles and corotating interaction regions in the solar wind, *Space Science Reviews*, *111*(3-4), 267–376.

Richardson, I. G., and H. V. Cane (2010), Near-earth interplanetary coronal mass ejections during solar cycle 23 (1996–2009): Catalog and summary of properties, *Solar Physics*, *264*(1), 189–237.

Rivera, Y. J., E. Landi, S. Lepri, and J. Gilbert (2018), Empirical modeling of a cme constrained to ion distributions detected by ace/swics, in *Solar Heliospheric and INterplanetary Environment (SHINE 2018)*.

Rosenbauer, H., et al. (1977), A survey on initial results of the helios plasma experiment, *Journal of Geophysics Zeitschrift Geophysik*, *42*, 561–580.

Schatten, K. H. (1972), Current sheet magnetic model for the solar corona, *NASA Spec. Publ.*, *SP-308*, 44.

Skoug, R., W. Feldman, J. Gosling, D. McComas, and C. Smith (2000), Solar wind electron characteristics inside and outside coronal mass ejections, *Journal of Geophysical Research: Space Physics*, *105*(A10), 23,069–23,084.

Skoug, R., J. Gosling, D. McComas, C. Smith, and Q. Hu (2006), Suprathermal electron 90 pitch angle depletions at reverse shocks in the solar wind, *Journal of Geophysical Research: Space Physics*, *111*(A1).

Smith, C. W., J. L'Heureux, N. F. Ness, M. H. Acuna, L. F. Burlaga, and J. Scheifele (1998), The ace magnetic fields experiment, in *The advanced composition explorer mission*, pp. 613–632, Springer.

Stakhiv, M. (2016), Tracing the solar wind to its origin: New insights from ace/swics data and so/his performance predictions, Ph.D. thesis.

Stansberry, J., J. Gosling, M. Thomsen, S. Bame, and E. Smith (1988), Interplanetary magnetic field orientations associated with bidirectional electron heat fluxes detected at isee 3, *Journal of Geophysical Research: Space Physics*, *93*(A3), 1975–1980.

Steinberg, J., J. Gosling, R. Skoug, and R. Wiens (2005), Suprathermal electrons in high-speed streams from coronal holes: Counterstreaming on open field lines at 1 au, *Journal of Geophysical Research: Space Physics*, *110*(A6).

Vocks, C., C. Salem, R. Lin, and G. Mann (2005), Electron halo and strahl formation in the solar wind by resonant interaction with whistler waves, *The Astrophysical Journal*, *627*(1), 540.

Vocks, C., E. Dzifčáková, and G. Mann (2016), Suprathermal electron distributions in the solar transition region, *Astronomy & Astrophysics*, *596*, A41.

Wang, L., S. Krucker, G. M. Mason, R. P. Lin, and G. Li (2016), The injection of ten electron/3he-rich sep events, *Astronomy & Astrophysics*, *585*, A119.

Webb, D., and A. Hundhausen (1987), Activity associated with the solar origin of coronal mass ejections, *Solar physics*, *108*(2), 383–401.

Webb, D., E. Cliver, N. Crooker, O. St. Cyr, and B. Thompson (2000), Relationship of halo coronal mass ejections, magnetic clouds, and magnetic storms, *Journal of Geophysical Research: Space Physics*, *105*(A4), 7491–7508.

Wiedenbeck, M., A. Klassen, P. Liewer, N. Nitta, C. Cohen, G. Mason, and R. Leske (2015), Constraints on mechanisms for longitudinal spreading of impulsive seps from multispacecraft observations of scatter-free even, *PoS*, p. 106.

Zhang, J., et al. (2007), Solar and interplanetary sources of major geomagnetic storms (dst- 100 nt) during 1996–2005, *Journal of Geophysical Research: Space Physics*, *112*(A10).

Zurbuchen, T. H., and I. G. Richardson (2006), In-situ solar wind and magnetic field signatures of interplanetary coronal mass ejections, in *Coronal mass ejections*, pp. 31–43, Springer.